Modeling of Interactions of Electromagnetic Fields With Human Bodies

by

Krzysztof Caputa
M.A.Sc., University of Victoria, 1992
M.Sc., Nicholas Copernicus University, Torun, 1975

A Thesis Submitted in Partial Fulfillment of the
Requirements for the Degree of

DOCTOR OF PHILOSOPHY
in the Department of Electrical and Computer Engineering

We accept this thesis as conforming to the required standard.

Dr. M.A. Stuchly, Co-Supervisor, (Department of Electrical and Computer Engineering)

Dr. M. Okoniewski, Co-Supervisor, (Department of Electrical and Computer Engineering)

Dr. J. Bornemann, Departmental Member, (Department of Electrical and Computer Engineering)

Dr. J. Provan, Outside Member, (Department of Mechanical Engineering)

Dr. R.H. Johnston, External Examiner, (Department. of Electrical and Computer Engineering, University of Calgary)

University of Victoria

Co-Supervisors: Dr. M.A. Stuchly and Dr. M. Okoniewski

Abstract

Interactions of electromagnetic fields with the human body have been a subject of scientific interest and public concern. In recent years, issues in power line field effects and those of wireless telephones have been in the forefront of research. Engineering research compliments biological investigations by quantifying the induced fields in biological bodies due to exposure to external fields. The research presented in this thesis aims at providing reliable tools, and addressing some of the unresolved issues related to interactions with the human body of power line fields and fields produced by handheld wireless telephones.

The research comprises two areas, namely development of versatile models of the human body and their visualisation, and verification and application of numerical codes to solve selected problems of interest. The models of the human body, which are based on the magnetic resonance scans of the body, are unique and differ considerably from other models currently available. With the aid of computer software developed, the models can be arranged to different postures, and medical devices can be accurately placed inside them.

A previously developed code for modeling interactions of power line fields with biological bodies has been verified by rigorous, quantitative inter-laboratory comparison for two human body models. This code has been employed to model electromagnetic interference (EMI) of the magnetic field with implanted cardiac pacemakers. In this case, the correct placement and representation of the pacemaker leads are critical, as simplified computations have been shown to result in significant errors.

In modeling interactions of wireless communication devices, the finite difference time domain technique (FDTD) has become a *de facto* standard. The previously developed code has been verified by comparison with the analytical solution for a conductive sphere. While previously researchers limited their verifications to principal axes of the sphere, a global (volumetric) fields evaluation allowed for identification of locations of errors due to staircasing, and the singularities responsible for them.

In evaluation of safety of cellular telephones and similar devices, the specific absorption rate (SAR) averaged over a 1 g (in North America) or 10 g (in Europe) cube is used. A new algorithm has been developed and tested, which allows for automatic and reliable identification of the maximum value with a user-selected inclusion of air (if required). This algorithm and the verified code have been used to model performance of a commercial telephone in the proximity of head, and to model EMI of this phone with a hearing aid placed in the ear canal. The modeling results, which relied on a proper representation of the antenna consisting of two helices and complex shape and structure of the telephone case, have been confirmed by measurements performed in another laboratory. Similarly, the EMI modeling has been in agreement with acoustic measurements (performed elsewhere). The latter comparison has allowed to confirm anticipated mechanism of the EMI.

Examiners:

Dr. M.A. Stuchly, Co-Supervisor, (Department of Electrical and Computer Engineering)

Dr. M. Okoniewski, Co-Supervisor, (Department of Electrical and Computer Engineering)

Dr. J. Bornemann, Departmental Member, (Department of Electrical and Computer Engineering)

Dr. J. Provan, Outside Member, (Department of Mechanical Engineering)

Dr. R.H. Johnston, External Examiner, (Department. of Electrical and Computer Engineering, University of Calgary)

Table of Contents

List of Figures

List of Tables

Acknowledgements

I am deeply indebted to both my co-supervisors for many things: Dr. Maria Stuchly for bringing me into the field of computational electrodynamics and directing me into numerical modeling, for modeling ideas and for guidance in completing this work; Dr. Michal Okoniewski for introducing me to FDTD and for letting me use his magnificent code, for always being able to resolve modeling problems and for discussions over doughnuts at Tim Hortons.

I owe gratitude to Dr. Trevor Dawson for letting me use his SPFD code and for countless suggestions for model improvements. I am also grateful to Dr. Stan Stuchly for the introduction to microwave measurements, antenna testing, and permittivity spectroscopy, but most of all for the advice to enroll in the Ph.D. program.

I would like to thank my colleagues, and once fellow students: Elise Fear, Mike Potter and Mizan Rahman for their feedback about body models and for the enlightening discussions over coffee breaks. I would like to thank Dr. Luis Netter for medical expertise with the models and for the Brazilian coffee.

Many thanks go to Ms. Donna Shannon for all the administrative help and to Ms. Vicky Smith for bailing me out countless times.

To Ewa, John Paul and Ursula

1 Introduction

1.1 Motivation

Electromagnetic (EM) fields are a natural component of Earth's environment. The geomagnetic field, which varies between 25 to 65 μT depending on the position on the globe, is known to have been present at similar levels all throughout the Earth's planetary history. All living organisms on Earth exist in presence of this field. Apart from the possibility that some migratory birds and whales may use the geomagnetic field for navigation, this field appears to be unimportant to living organisms. On the other hand, it is the very presence of the geomegnetic field that makes life on Earth possible, because it diverts the deadly stream of cosmic rays away from the planet's surface. The geoelectric field, due to the positively charged ionosphere and negatively charged ground surface, has also been persistently present in Earth's history. In good weather this field has a magnitude of about 200 V/m, but it does increase to 20,000 V/m or more during thunderstorms [1]. Both geomagnetic and geoelectric fields are static. Time varying (AC) EM fields and waves in the frequency range from a few Hz up to low infrared appear in nature only briefly as transients during the thunder strikes, or solar storms. These are very weak AC fields, except for the very close proximity of a lightning strike.

Increasingly people have been exposed to man-made AC fields, ever since the advent of electric power in the late 19th century. The spectrum of man-made EM fields extends from static magnetic and electric fields all the way to hard gamma rays. In this work we restrict our scope to the lower part of EM spectrum, below the infrared light. The man-made fields in this part of the spectrum tend to be orders of magnitude stronger than the naturally occurring fields. At the low end, the fields at power line frequencies of 50 or 60

Hz are particularly strong. There are no natural sources of fields comparable in magnitude to those close to power lines, industrial installations or home wiring and appliances. In the RF region, the absence of natural sources of electromagnetic waves helped tremendously in the initial development of radio communication and broadcasting. Subsequently, as more powerful RF sources were invented for higher frequencies the current state has been reached where the entire RF spectrum, up to high end millimeter waves, is allocated to various uses and services. Most of these uses have transmitting antennas located on tall masts and in places accessible only to service personnel, and thus do not expose people to high intensity fields in the proximity of antennas. However, recent proliferation of personal communication devices, such as cellular phones, has lead to a dramatic increase in the RF exposure encountered in everyday life.

Concerns about the health effects of man-made EM fields have been around as long as electric power. The shocks, tissue burns and electrocution suffered when touching high voltage wires were recognized as hazard early in the age of electricity - as soon as the sufficient power was generated. On the other hand, determining whether a long term exposure to low-level electric and magnetic fields poses a health hazard has proven to be much more challenging and is still a subject of research. The possibility that diseases such as leukemia and other cancers may be caused by the long term low level exposure to man-made EM fields continues to frighten the public and is the motivation for research.

The studies into the health effects of long-term exposure have been progressing on several fronts. Epidemiologists search for correlations between randomly occurring illnesses and the presence of elevated EM fields. Medical scientists and biologists, in addition to experimentation on animals and cell preparations, search for the plausible bio-chemical mechanisms of the interactions. Very important in this search is the EM field dosimetry. Dosimetry in this context is defined as evaluation of various parameters related to the electric field strength in tissue. This is where computer models of the human body and computational electromagnetics play a very important role. Using accurate, high resolution body models based on MRI scans of human subjects, and advanced electromagnetic codes it is possible to map accurately the induced fields in organs and tissues resulting from the external sources of AC fields, without having to insert field probes in the subjects and expose them to the actual field. Thus obtained data can be used to verify the biophysical hypotheses that may arise to explain epidemiological data. The knowledge of the induced fields distribution is also crucial for developing consistent, science-based standards for safety of human exposure to various field configurations.

A related subject is the Electromagnetic Interference (EMI) of external EM fields with the implantable medical devices, e.g., heart pacers, or devices worn in a body cavity, e.g., hearing aids. These devices are known to be susceptible to EMI. However, the experimental data obtained for them in free space or in simple physical body models are not usually fully representative (and on occasions completely erroneous) of their performance in the actual environment of a human body. Incorporating a model of the device into the human body model makes it possible to compute the EMI directly, and to remove the guesswork from the experimental data. With computer modeling it may also be possible to gain insight into the EMI mechanisms that are not accessible through experiments.

1.2 Research objectives and contributions

The objectives of research described in the thesis include:

1. Development of a variety of models of the human body for investigating the dosimetry at ELF and microwave frequencies. At the time of the thesis commencement, models of the human body compatible with computational codes were not available. In addition to a good overall representation of the shape and size of the body and its organs, there are specific requirements imposed on the models by the focus of a particular interaction modeling:
    - ☐ Modeling of currents induced in bone marrow by ELF fields demands continuity of this tissue in its location inside bones and the integrity of the less conductive bone tissue surrounding it.
    - ☐ Modeling occupational ELF exposure of line workers requires a variety of body postures appropriate for representative work scenarios.
    - ☐ Modeling of interference with cardiac pacemakers demands a faithful representation of the heart and the major veins and arteries.
    - ☐ Modeling of fields induced in a human head by a cellular telephone requires a high-resolution model of the head with an accurate representation of the external ear and ear canal. The latter is critical for evaluation of EMI with hearing aid.

2. Development of new algorithms to numerical methods at microwave frequencies for evaluation of field – human interaction. The safety guidelines for RF exposure are defined in terms of the weight-averaged Specific Absorption Rate (SAR), and this quantity needs to be computed from the EM fields inside the body. Prior to this research only non-systematic, ad-hoc methods have been used.

3. Verification of numerical methods used in modeling of the field – human interactions at ELF and microwave frequencies. Due to absence of experimental data on EM fields inside the body, there is a need to validate any numerically obtained data by repeating the modeling using a variety of EM solvers and a variety of human body models of varying complexity - from simple geometric solids to full anatomic models.

4. Modeling of selected interactions of practical importance.

The original contributions of the thesis are:

1. Development of unique models of the human body:
   - ☐ adding arms, legs and head to an existing torso model to obtain a high resolution model (3.6 mm) of a male adult in upright position
   - ☐ refinement of circulatory system of the model to assure electrical continuity of major blood vessels
   - ☐ refinement of bone and marrow tissues in arms and legs to assure continuity of both tissues
   - ☐ articulated models in various standing and sitting postures and different positions of arms, as required by the conditions of the modeled interactions
   - ☐ a child model with body size and proportions of a typical 5 year old
   - ☐ a model of cardiac pacemaker patient, with the metallic box of a pacer positioned in the chest according to clinical data
   - ☐ accurate external ear and ear canal in the high resolution (1.1 mm) head model
   - ☐ development of tools for 3D data visualization and data format conversions

2. New efficient algorithm for 1g/10g SAR

   - the accurate 12-component method of obtaining voxel-centered electric field from the voxel-edge electric field components of the FDTD
   - the FDTD method to compute the specific absorption rate (SAR) averaged over 1 or 10 g cube of tissue (Caputa et al. *IEEE Antennas & Propag. Magazine,* vol. 41 (4), pp. 102-107, August 1999)

3. Validation of electromagnetic codes for use with human body models
   - a comparison of ELF dosimetry results from two independently developed SPFD solvers and advanced body models (joint effort with NRPB lab in UK) (Caputa et al., *Phys. Med. Biol.,* 47 (8), pp. 1391-1398, April 2002*)*
   - a comparison of fields inside a dielectric sphere illuminated by a plane wave obtained with the FDTD for frequencies from 100 MHz to 2 GHz with analytical solution based on the Mie series.
4. Modeling of selected problems of practical importance:
   - heart pacer with unipolar leads implanted in the body model and subjected to Electromagnetic Interference (EMI) by the ELF magnetic fields at levels possible in work environment (Dawson, Caputa et al. *IEEE Trans. Biomed. Eng, vol. 47, pp. 2000*)
   - FDTD modeling of a dual helix antenna of a PCS phone using staircase approximation, with rigorous verification of the near fields against the measured data from the real phone (Caputa et al. *Proceedings, IEEE Aerospace Conf. 2001*)
   - FDTD modeling of the EMI with the hearing aid device from a PCS phone. (Caputa et al., *IEEE Trans. Microwave Theory Tech., vol. 48, pp. 2000*)

1.3 Outline

Chapter 2 presents the background information. Interaction mechanisms are reviewed between the EM fields and human body. After a brief presentation of interactions over the entire EM spectrum the mechanisms applicable at the high end of the RF/MW range are discussed, with a particular attention to near fields generated by personal communication devices. At RF frequencies for which body dimensions are comparable to or larger than the wavelength of the EM waves it is necessary to compute a full wave solution for waves propagating through body organs and tissues. To describe the interaction, it is more appropriate to consider the power deposited in organs and tissues rather than the electric or magnetic field distributions. Specific Absorption Rate (SAR) in body tissues is used as the dosimetric measure. At Extremely Low Frequencies (ELF), external electric and magnetic fields induce electric currents in body tissues. The electric and magnetic fields at ELF are uncoupled and their respective induced currents can be considered separately, while their combined effect is obtained through superposition. Computer modeling of a human body is introduced and dielectric properties of tissues are reviewed.

Chapter 3 describes models of the human body that have been developed to compute internal fields resulting from various EM sources outside the body. Methodology of the model development is presented, and model characteristics are tabulated. The three-dimensional data visualization is an important aspect of model development and use in evaluating the interactions. Advanced visualization techniques are used to obtain external views of the body model in various positions and postures. Body organs and tissue composition are presented in 2D cross-sections and 3D volumes.

Chapter 4 presents the computational methods used. Scalar Potential Finite Difference (SPFD) method is a variation of a Finite Difference (FD) method. This method is particularly suitable for computing quasi-static solutions of fields induced in body models by external fields - magnetic and electric. Finite Difference Time Domain (FDTD) code is a full wave solver based on discretization of the Maxwell equations in the differential form. Because of the computational demands of modeling with a high resolution, the SPFD and FDTD codes have been ported to run on the IBM SP2 parallel supercomputer.

Chapter 5 presents new algorithms that have been developed to compute the weight averaged SAR from the field solutions obtained for uniform and non-uniform FDTD meshes. The 3-component, 6-component and 12-component methods of interpolating the edge fields of FDTD into the voxel centers are compared. The 12-component algorithm to interpolate the edge-distributed power into voxel centers is improved for consistency with conductivity distribution. An accurate SAR algorithm is developed in two varieties: one for uniform FDTD meshes and the other for non-uniform and graded meshes.

Chapter 6 presents the verification of modeling codes: SPFD at ELF, and FDTD at RF and microwave frequencies. At ELF, the organ dosimetry is obtained for the external source of a 60 Hz magnetic field. Results for different body models and different resolutions are compared. This data are also compared to the data obtained by another research group, which used its own computer code for the same body models and field sources. The full wave solver based on the FDTD method is validated at RF frequencies by comparing the fields computed by FDTD inside and outside of a lossy dielectric sphere illuminated by a plane wave, with fields obtained analytically, using a Mie series.

Chapter 7 presents modeling of selected problems in ELF, RF and microwave frequency ranges. An analysis of the interaction of an ELF magnetic field with an electronic heart pacer properly positioned in the patient's chest addresses the issue of safety of workers with pacer implants in a high fieldwork environment. The EMI resulting from external magnetic fields at a power-line frequency of 60 Hz is computed at inputs of heart pacers. At RF and microwave frequencies the focus is on the interaction between a cellular phone and the model of a human head. An FDTD model of a cellular phone equipped with a dual helix antenna is constructed. Staircase representation of both helices in the FDTD mesh has been refined through comparison with the measured near-field maps obtained by another research group for the real phone. The validated FDTD model of the cellular phone is used together with the head model to compute the radiation patterns in presence of the head, SAR in the head and EMI effect on hearing aid device worn inside the ear.

Concluding remarks and suggestions for further research are presented in Chapter 8.

2 Background Information

In this chapter the mechanisms of the interaction of EM fields and waves with biological tissues are reviewed. The emphasis is placed on the power-line frequencies, which are a part of the ELF range, and in the RF part of the spectrum on the frequencies used in wireless communication. Predicting the fields inside the body from external sources using theoretical, experimental and computational methods is presented in a historical perspective. Discretized models of human body are discussed, followed by the review of dielectric properties of body tissues.

2.1 Biophysics of electromagnetic fields

As Richard P. Feynman observed [2] our almost entire experience of the physical world is electromagnetic in nature. We see the world through electromagnetic waves in the visible part of the EM spectrum. When we touch objects we feel the force between electrons in our skin and the electrons of the object we touch. The electromagnetic forces between atoms and molecules give solids, liquids and gases their macroscopic properties. But what are the specific effects that the external electromagnetic fields may have on biological systems?

Life sciences tell us that chemical processes involving complex organic molecules form the basis of the biological phenomena. All chemical bonds originate from electromagnetic forces between atoms and molecules. The energy released or absorbed in chemical reactions is due to changes in internal the EM fields of atoms and molecules. At the same time, because of quantum laws that govern the absorption and emission of EM energy, the ability of applied fields to cause chemical reactions is predetermined by the frequency of the fields. Planck's law provides that a quantum of energy E released or absorbed by an atom in the single act of interaction with EM field is related to the field frequency *f*:

$$E = h \cdot f \tag{2.1}$$

where $h = 6.63 \times 10^{-34} J \cdot s$ is the Planck's constant. Considering a typical electrochemical potential of chemical bonds at the order of 0.5 to 5 V and the conversion factor of $1.0eV = 1.6 \times 10^{-19} J$, it takes frequencies of the EM field of the order of 10^{+14} to 10^{+15} Hz, or higher, to break such bonds. In wavelength this corresponds to 300 – 3000 nm, which covers the range of EM radiation from infrared to ultraviolet including the visible light range of 400 to 800 nm. In view of Planck's law it is clear that the ability of the EM fields to interfere with biochemical processes of living organisms is dependent on the frequency of the fields.

The frequency and wavelength spectrum of EM fields is presented in Figure 2-1. The top row of the diagram shows various sources of man-made EM fields positioned against the spectrum. In the bottom part of diagram various physical effects are related to frequencies of the spectrum. At the right end of diagram are the X-rays and Gamma rays, which represent the shortest wavelengths and the highest frequency part of EM spectrum. X-rays are generated by bouncing the electron beam off heavy nuclei while radioactive isotopes emit gamma rays. The X-rays have the ability to penetrate through matter and their photons carry enough energy to each cause an avalanche of secondary electrons, which in turn are capable of breaking chemical bonds and cause damage to genetic material in living cells.

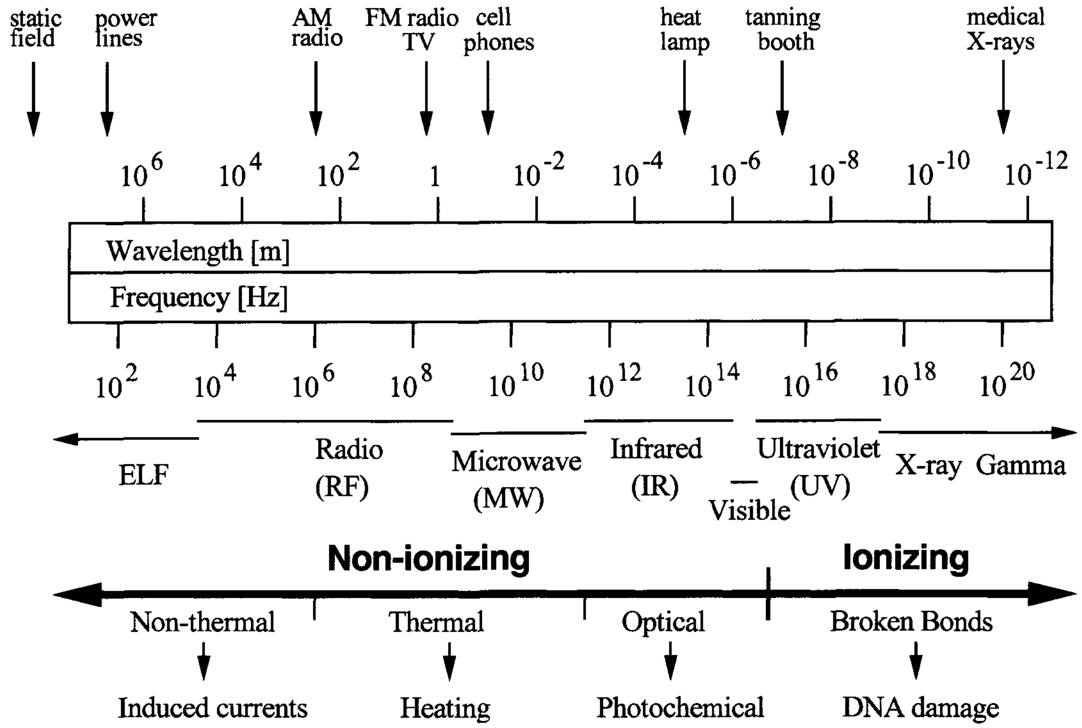

Figure 2-1 Electromagnetic spectrum

Due to this ability, the high energy X-rays found application in radiation therapy. By focusing the rays on the affected internal organs, cancer tumors can be killed without the need for surgery. Softer X-rays have wide applications in medical diagnostics, in the traditional 2-dimensional X-ray pictures and in the more recent 3-dimensional CT scans. Because of the damage that X-rays can cause to healthy tissues, the exposure needs to be monitored and minimized both in the treatment and in diagnostics. The amount of ionizing radiant energy absorbed by matter per unit mass, or the density of ionizing energy is called the dose:

$$D = \frac{dE}{dm} \tag{2.2}$$

The SI unit of dose is the *gray (Gy)*. One gray is defined as 1J of ionizing energy absorbed per kilogram of material irradiated. The unit in conventional use in North

America, the *rad* is 100 times smaller.

Less energetic quanta of ultraviolet light also have the ability to damage DNA but do not penetrate deep into body. Man-made UV radiation is commonly generated by mercury arc lamps and used in beauty spas for tanning. Even though UV radiation is a powerful chemical agent, the UV component of sunlight is a part of the natural environment and does not represent health hazard comparable to X-rays, partially because the human body evolved to defend vital tissues from the UV with the skin pigmentation. While it is a well-established fact that excessive exposure to UV, both natural and man-made, can be a cause of skin cancer, some UV exposure is beneficial to health because it helps the body synthesize vitamin D.

The next component of the EM spectrum, the visible light is the range of EM frequencies for which we are equipped by nature to perceive directly. With our eyes we see EM waves ranging in frequency between 37 and 75 THz. Visible light does cause photochemical reactions and as a photosynthesis agent this part of the sunlight spectrum is the source of energy for the entire cycle of life on Earth. Man-made sources of light have been in use for ages and there are no known health risks of normal exposure to light, either natural or artificial.

Below the visible light is the infrared range. Quantum energy associated with this range is sufficient to cause some chemical effects; however, the skin is opaque to IR and only skin heating occurs when IR is absorbed. The natural environment is flooded with a wide spectrum of IR: shorter wavelengths from the sunlight and the longer wavelengths emanating from heat sources and warm objects. The infrared range is considered a part of the optical engineering domain and optical methods are predominantly used to generate and to detect the frequencies from that range.

Following the infrared range are the microwave frequencies, which can now be produced and detected by circuits with electrical current. A somewhat arbitrary division between the infrared range and microwaves may be set at 300 GHz, which corresponds to a free space wavelength of 1 mm. Quantum energy in the upper part of this range is only sufficient to elicit rotation of molecules and the energy associated with this relaxation phenomenon is dissipated as heat. At frequencies below 10 GHz, RF causes ion motion manifesting itself as current flow, which through ohmic losses also introduces heat.

The frequencies from 0 to 300 GHz have found many uses in engineering, and have been allocated to various practical purposes and services that are too numerous to enumerate. The division of this part of the spectrum into the upper part called microwave (MW) range and lower part called radio frequency (RF) range is arbitrary and mostly historical. The lower limit of what frequencies constitute "radio" is also not precisely defined, but 3 kHz is a commonly accepted starting point for the radio spectrum. For instance the IEEE standard for RF exposure [3] defines the RF range as extending from 3 kHz to 300 GHz. The EM frequencies below RF are commonly classified as Extremely Low Frequencies (ELF). At these frequencies the distance from source is a very small fraction of the wavelength. Consequently the electric and magnetic fields are decoupled from each other and are only dependent on their respective sources.

Two sub-ranges of the RF and ELF range, gained a particular attention over the course of last decade in the context of public health, namely: power line frequencies of 50/60 Hz, and the 800 MHz and 2 GHz bands in which the cellular phones and other personal communication devices operate. The interactions between EM fields and the human body and the implanted medical devices in these two frequency sub-ranges are the main object of this dissertation.

2.2 Interactions at RF frequencies

2.2.1 Dosimetry

For frequencies of 10 MHz to 300 GHz, the quantum energy is too small to directly alter the chemistry of biological molecules. Although it has been suggested that narrow ranges of frequencies (sometimes referred to as "windows"), might exits in the upper microwave region, within which the RF would excite particular vibrational states of molecules leading to some biological responses, such as accelerated cell growth rate, the experimental evidence has been inconclusive [4]. Excluding that possibility, the only well established effect of the RF on biological systems is the change of a local temperature due to the absorption of EM energy by the tissue.

Maintaining the temperature of the body is a vital part of animal physiology. Humans and other mammals are equipped with thermoregulatory systems, which effectively deal with the environmental temperature changes with the highest priority given to keeping constant temperature of the central nervous system. An important new factor of man-made RF fields is that they deposit thermal energy directly into internal tissues and organs, while the thermoregulatory system responds to temperature receptors, which are located mostly in the skin. By producing different than natural heat gradients, the stress due to RF absorption can potentially overwhelm the thermoregulatory system with dire consequences for health.

Based on the extensive research, both experimental and theoretical, various national and international standards and guidelines have been established for safe levels of RF exposure at different frequencies. Representative recent RF exposure safety standards are reviewed in Appendix E. The dosimetric measure that is accepted and used in these standards is the Specific Absorption Rate (SAR), defined as the time derivative of the incremental energy ΔW absorbed by or dissipated in the incremental mass Δm contained in the volume element ΔV of a given density ρ:

$$SAR = \frac{d}{dt}\left(\frac{\Delta W}{\Delta m}\right) = \frac{d}{dt}\left(\frac{\Delta W}{\rho \cdot \Delta V}\right) \tag{2.3}$$

In comparison with the ionizing radiation dose of Eq. 2.2, the SAR as dosimetric measure reflects the fact that heat deposition into the body is not as inherently harmful as the effects of ionizing radiation. It can only be harmful, if the rate of deposition exceeds the rate of heat dissipation by both natural conduction and the active thermoregulatory response of the body.

Determining the SAR in a human body at the given RF field is a challenging task. Two approaches have been used. In the experimental approach, models of human body and body parts have been made consisting of thin plastic shells imitating the shapes of the body and body parts, filled with liquid dielectric imitating electromagnetic properties of body tissues. This type of a model, the so called phantom, has openings in the plastic shell allowing for an insertion of field probes to measure the internal fields arising from exposure to external sources. The probes are used to measure the fields directly, usually the electric field components along the 3 orthogonal axes. The SAR can be computed from the measured fields and known conductivity and density of the simulated tissue at the given RF frequency. Alternatively, a temperature probe can be used to detect the local temperature increase due to absorbed EM energy, and thus evaluate the SAR directly. Complex high quality phantoms of human body with a number of internal organs of appropriate dielectric properties were developed by Stuchly et al. [5] in mid 1980s and were used to evaluate SAR. Similar, but limited to the head, phantoms are extensively used today for testing portable telephones [13], [14].

The second approach is to theoretically predict field intensity and associated SAR inside a body exposed to RF radiation. In a work dating back to 1956, the simplest case was considered by Schwan and Li [6], where a half-space with the average dielectric properties of the human body was subjected to the perpendicular incidence of a plane wave. In a slightly more complicated scheme multiple layers were also considered in the half-space dielectric to imitate skin, fat, muscle and bone. In these considerations an early insight was obtained at the penetration of body by radar frequencies of 915 MHz and 2.450 GHz.

Homogeneous and layered spherical and ellipsoidal models of the human body were considered in the 1970s using the analytic Mie expressions for scattered fields [7], [8], [9]. Using a homogeneous prolate spheroid model of the body a “resonance” effect was revealed for the impinging wave of E-polarization along the longest dimension of the spheroid. The average SAR for the whole body showed a maximum at the resonance, which occurred at the spheroid maximum dimension 0.4λ, where λ = free space wavelength. An average male body of 1.75 m height and a mass of 70 kg was represented by prolate spheroid with the axis ratio of 6.34. The resonance for this height was observed at 70 MHz. Based on this analysis, for frequencies below the resonance the SAR decreased as a square of frequency, and became very small at frequencies below 1 MHz. This simplistic modeling of a body was also applied to relating SAR in laboratory rats to humans, which was essential for planning of exposure experiments and interpretation of the results.

Further progress in predicting the internal fields and SAR was made, when more complex body models were introduced. In these models the body and its internal organs were divided into a number of simple solids and iterative computer field solvers using Method of Moments (MoM) technique were applied. In 1977 Gandhi et al [10] used a body model made of 180 cubical cells of unequal size. A more refined version of the same technique using a 340-cell model was applied by DeFord et al in 1983 [11].

Great advancements in computational methods for electromagnetics and a vast increase of available computational power occurred in the 1980s and 1990s. As a result it became possible to predict the fields in models consisting of millions of cubical cells. The computational method that gained prominence in predicting fields in such complex human body models is the FDTD (which is presented in Chapter 4).

Parallel to the progress in computational electromagnetics has also been the improvement in anatomically-based body models. The models used in the late 80s had a resolution of 12 mm and were based on the cross-sectional atlas of the human body published in 1911. In the 1990s the models were subsequently refined to 5, 3.6, 2 and 1 mm. This progress was made possible by the availability of detailed CT and MRI scans of the human body. Particularly significant was the Visible Human Project of NIH [12], which created and put in the public domain a database of 1 mm cross-sections of a male cadaver recorded as digitized color photographs and CT images with 1 mm resolution and MRI images with 5 mm resolution. Development of human body models, that are compatible with electromagnetic computational codes, is presented in Chapter 3.

2.2.2 Personal communication devices

The proliferation of cellular phones and other personal communication devices, which occurred in the last decade brought with it new issues and concerns. Technical characteristics of several representative devices and services are summarized in Table 2-1. One unifying characteristic of these devices is that they transmit RF in very close proximity of the user's head. Although the transmitted power of these devices is relatively low, the possibility exists that the highly concentrated field near the antenna may locally cause SAR values higher than previously established as safe.

Table 2-1 Systems and services that utilize handheld transmitters

System	Service type	Where used	Tx frequency [MHz]	Average power [mW]	Peak power [mW]
AMPS	analog cellular	North America	824-849	600	800
NADC	digital cellular	North America	824-849	200	600
GSM	digital cellular	Europe	880-915	250	2000
PDC	digital cellular	Japan	940-956 1477-1501	200	600
PCS	digital	North America	1850-1910	125	200
DCS	digital	Europe	1710-1785	31	248
CTO	analog cordless	Worldwide	45-49	10	10
CT2	digital cordless	Worldwide	864-868	10	10

Antenna performance of a handheld device is also adversely affected by the absorption of RF power in the human tissues, and from the design perspective it is desirable to minimize this effect. A related issue is the Electromagnetic Interference (EMI) of cellular phones with medical devices, such as hearing aids worn inside the ear canal, or cochlear implants located in the inner ear. The study of this phenomenon requires proper modeling of near fields of the handheld transmitter and the environment in which the device is working, which includes the human head.

Both experimental and computational methods have been applied to investigate the interaction between cellular phones and the human body. Experimental methods have an advantage of using the actual physical telephone as the source of the RF field but are disadvantaged by inaccurate head phantoms, which only reproduce the external shape of the head while neglecting inhomogeneities of the head inside.

Using the FDTD method with high-resolution head models, which reproduce anatomy and tissue composition of the user's head, allows for accurate mapping of SAR over the volume of the head. To accurately reproduce the near fields of a transmitter, which enter the head, it is equally important to also model the intricate details of the antenna system. Most common among the commercially available handheld devices are normal mode helical antennas, which cannot be easily modeled on a rectangular FDTD grid.

Several approaches have been used in the past to model small helices in FDTD. In one approach a very fine FDTD grid is used to discretize the metal helix. Accurate representation of helical wire curvature requires at least 3 grid cells per wire diameter, which implies the grid size of 0.2 mm or smaller. Using such fine resolution in the FDTD computational space that also contains the head model is very costly in both memory and CPU time, even if the graded mesh is utilized for local grid refinement around the helix. In a different approach Lazzi et al [69], used sub-cell modeling of a helix. This method relied on imposing analytically derived fields E and H in the volume occupied by the helix. This method has a serious limitation, as it represents an idealized theoretical helix.

In Chapter 7 a combination of experimental and computer modeling is applied to accurately predict the near fields is described for modeling a GSM cellular phone with a dual helical antenna.

2.3 Interactions at power line frequencies

For frequencies below 1 MHz the thermal effects of EM fields in the human body are insignificant. Although many mechanisms have been proposed for the interaction of power-frequency fields with the human body, the only one that withstands the scientific scrutiny is the induction of electric fields and currents in tissues. The main phenomenon of biological significance associated with induced fields and currents is the ion transport in physiological liquids and across cell membranes. Considerable displacement of ions during a single AC cycle is only possible at the low end of RF and at the ELF. Directly related to this effect is the nerve stimulation by the induced electrical currents, which only occurs when a certain threshold current density is exceeded across tissues containing nerve fibers. Nerve stimulation also occurs only below 100 kHz.

The same mechanism of induced currents that is responsible for nerve stimulation can also cause EMI with implanted medical devices such as heart pacers or defibrillators. Modeling of current induction in body models and the EMI of induced fields with heart pacemakers are presented in Chapter 5.

2.3.1 Typical field strengths

Fields near the ground directly under high-voltage transmission line can approach 10 μT and 10 kV/m. At the edge of the transmission line corridor fields typically are 0.3 to 3.0 μT and 0.1 to 1.0 kV/m.

Residential fields vary from over 150 μT and 0.2 kV/m a few centimeters from certain appliances to less than 0.02 μT and 0.002 kV/m in the center of many rooms.

In occupational exposure AC fields as high as 8 – 70 mT have been reported but more typically electrical power station workers encounter fields of 0.5 mT at the highest while the time averaged exposure registered by personal dosimeters does not exceed the value of 8.4 μT [26].

2.3.2 Dosimetry

Theoretical, experimental and computational methods described in section 2.2 are also applicable with modifications to determine electric currents induced in the body by external electric and magnetic ELF fields. Thus, quasi-static Mie solutions have been used to determine the currents induced in spherical models of a body [31]. Liquid filled body phantoms and mechanically scanned electric field probes have been used to map the currents induced in the body [78], and discretized computer body models combined with appropriate field solvers have been used to determine the currents induced in a body by externally applied electric and magnetic fields [18]. Computational methods that are most commonly used in conjunction with discretized body models are the impedance method, (IM), scalar potential finite-difference method (SPFD), finite difference time-domain method (FDTD) and quasi-static FDTD. Since strong ELF fields are only encountered at very small distances from the source in comparison with the wavelength, the electric and magnetic fields can be considered uncoupled and their effects can be evaluated separately, while the combined effect can be obtained by simple superposition.

The dosimetric measure that is used to quantify the ELF exposure is the average current density or the electric field over the organ or body part volume. Using this measure it is possible to compare the exposure resulting from various electric and magnetic field configurations with those resulting from contact currents. Comparison of body part and organ averages of induced fields in humans and laboratory animals, such as mice or rats is crucial for the design of exposure experiments and interpretation of their results.

2.4 Electrical properties of tissues

Computational models of the human body provide the mapping of organs and tissue types on three-dimensional space. In addition to that, in order to compute the distribution of fields in the model, it is also necessary to know the electromagnetic properties of all the tissues represented in the model.

Biological tissues can be described as non-magnetic, lossy dielectrics. Thus they are characterized by the relative permeability of 1.0 and a complex relative permittivity:

$$\varepsilon^* = \varepsilon' - j\varepsilon'' = \varepsilon' - j\frac{\sigma}{\omega\varepsilon_o} \tag{2.4}$$

where, in the simplest case, the imaginary part ε'' is due to static conductivity σ and varies with frequency ω as expressed in the right part of Eq. 2.4. A more general case of the dependence of permittivity on frequency is given by the Debye equation:

$$\varepsilon^* = \varepsilon_\infty + \frac{\varepsilon_s - \varepsilon_\infty}{1 + j\omega\tau} - j\frac{\sigma_s}{\omega\varepsilon_o} \tag{2.5}$$

where τ is the relaxation time, ε_S is the static permittivity, ε_∞ is the asymptotic permittivity at high frequencies, σ_S is the static conductivity and ε_0 is permittivity of free space. In polar liquids, such as water or alcohol the relaxation phenomenon is due to mechanical inertia of electrically polarized molecules being reoriented in the applied electrical field. These dielectrics are well described by a single relaxation of Eq. 2.5. Biological tissues, which can be seen as mixtures and dilute suspensions of particular organic matter in water are better described by a multiple relaxation Debye equation:

$$\varepsilon^* = \varepsilon_\infty - j\frac{\sigma_s}{\omega\varepsilon_o} + \sum_i \frac{\Delta\varepsilon_i}{1 + j\omega\tau_i} \tag{2.6}$$

An empirical refinement of Debye dispersion is known as Cole-Cole dispersion. To better fit the observed data the $j\omega\,\tau_i$ terms of a multiple relaxation equation are raised to the power $(1-\alpha_i)$ where α_i coefficients are small positive fractions:

$$\varepsilon^* = \varepsilon_\infty - j\frac{\sigma_s}{\omega\varepsilon_o} + \sum_i \frac{\Delta\varepsilon_i}{1+(j\omega\tau_i)^{(1-\alpha_i)}} \tag{2.7}$$

Permittivity of body tissues observed over the broad spectrum of RF, is characterized by 4 distinct dispersions [27], which, in order of increasing frequency, have been termed Alpha, Beta, Gamma and Delta. Alpha dispersion occurs at frequencies under and around 1 kHz and is due to counterion polarization of cell membranes combined with the polarization of the sarcotubular systems inside the cells. Beta relaxation occurs at RF frequencies, and is caused by the charging of interfaces between the insulating cell membranes, the cell interiors, and extracellular suspension. This relaxation results in a large decrease in permittivity and an increase in conductivity due to increased conduction through cell membranes. Gamma and Delta relaxations are due to the dipolar relaxation of water in the tissues, and respectively occur around 2 and 20 GHz.

The dielectric properties, used in both computational and experimental dosimetry, critically influence the results. Thus, their knowledge for various tissues represented in models is critical for reliable data.

Many researchers conducted measurements of electrical properties of human and animal tissues at various frequencies and the published results, particularly in the early works dating back to 50s and 60s were often conflicting. Gabriel *et al* [28], [29] undertook the monumental task of creating a consistent database of dispersion characteristics of tissues based on their own measurements and previous publications of other researchers [35], [36], [37]. Gabriel used the 4-pole Cole-Cole dispersion of Eq. 2.7 to fit the curves to the frequency points of measured permittivity. Dispersion parameters obtained for a few representative tissues are presented in Table 2-2. Using Gabriel's notation the parameters for Alpha, Beta, Gamma and Delta relaxations are indexed '4', '3', '2' and '1' respectively. As can be seen from the table the four relaxations have been identified for all the tissues except the blood, which does not have the Alpha and Beta relaxations.

Table 2-2 Cole-Cole dispersion parameters of selected tissues

	Blood	Brain	Bone	Cartilage	Fat	Muscle	Heart	Stomach
ε_∞	4.0	4.0	2.5	4.0	2.5	4.0	4.0	4.0
σ_s	0.7	0.02	0.02	0.15	0.035	0.2	0.05	0.5
$\Delta\varepsilon_1$	56.0	45.0	10.0	38.0	9.0	50.0	50.0	60.0
τ_1 [ps]	8.377	7.95	13.26	13.26	7.958	7.234	7.958	7.958
α_1	0.1	0.1	0.2	0.15	0.2	0.1	0.1	0.1
$\Delta\varepsilon_2$	5200	400	180	2500	35	7000	1200	2000
τ_2 [ns]	132.62	15.91	79.57	144.68	15.91	353.68	159.15	79.57
α_2	0.1	0.02	0.2	0.15	0.1	0.1	0.05	0.1
$\Delta\varepsilon_3$	0	2.0E+05	5.0E+03	1.0E+05	3.3E+04	1.2E+06	4.5E+05	1.0E+05
τ_3 [μs]	159.15	106.10	159.15	318.31	159.15	318.31	72.34	159.15
α_3	0.2	0.22	0.2	0.1	0.05	0.1	0.22	0.2
$\Delta\varepsilon_4$	0	4.5E+07	1.0E+05	4.0E+07	1.0E+07	2.5E+07	2.5E+07	4.0E+07
τ_4 [ms]	15.91	5.305	15.91	15.91	15.91	2.274	4.547	15.91
α_4	0	0	0	0	0.01	0	0	0

Using the dispersion parameters from Table 2-2 the real and imaginary parts of permittivity of Eq. 2.4 have been plotted in Figure 2-2. Relaxations Alpha, Beta, and Gamma and Delta are clearly evident as separate "humps" in the ε' plots (solid line) for all the tissues except the blood.

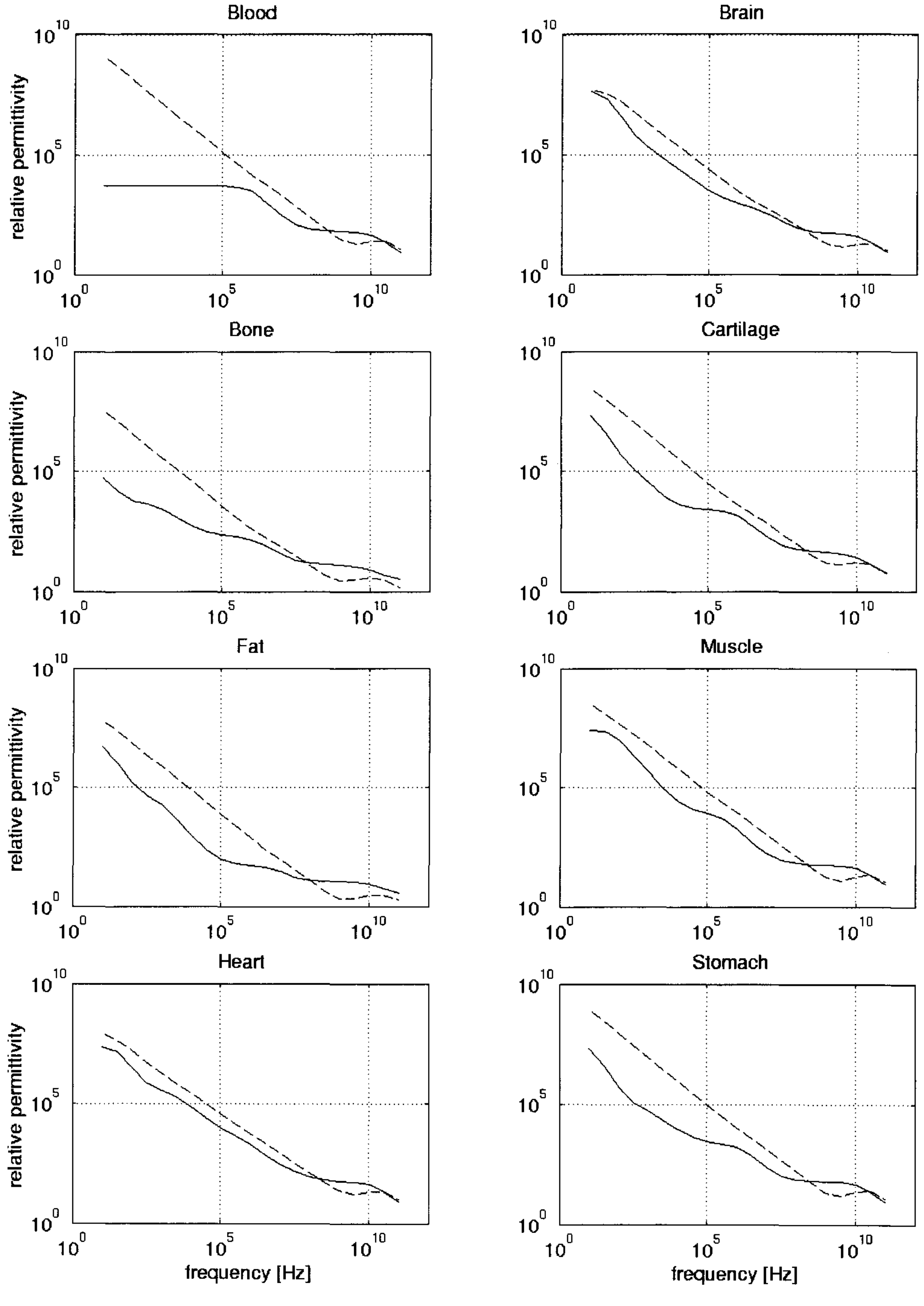

Figure 2-2 Relative permittivity of selected tissues as function of frequency. Real part ε' plotted solid, imaginary part ε'' plotted with dashed line.

An important observation from the perspective of modeling fields at 60 Hz is that at the ELF part of the spectrum in Figure 2-2 the real permittivity of tissues ε' is at least an order of magnitude smaller than the imaginary ε''. Thus the displacement currents at that frequency range may be considered negligible when compared with conduction currents.

At cellular phone frequencies of 900 MHz and 1.8 GHz it is seen that all tissues exhibit Gamma/Delta dispersion, which needs to be accounted for if a broadband FDTD computation is to accommodate both frequency bands in a single run.

2.5 Summary

This chapter presented the brief review of mechanisms of interactions between EM fields and the human body referenced to the EM frequency spectrum. Mechanisms of interaction at cellular phone frequencies and power frequencies, which are the focus of this work, have been presented in greater detail. Theoretical, experimental and computational methods used in determining fields induced in the body by external sources have been described together with the body models utilized by various methods. Electromagnetic properties of tissues are described by complex permittivity. Static conductivity combined with the four-pole Cole-Cole relaxation is sufficient to characterize tissues over the ELF/RF/MW frequency range. Cole-Cole parameters and dispersion plots of permittivity have been shown for a few representative tissues.

Suitable computational methods for dosimetry at ELF and RF were available at the onset of this research. However, their reliability in modeling complex heterogeneous bodies was not fully tested. Typical testing methods using analytic solutions for canonical problems, do not completely evaluate possible errors associated with the specific problems of interest. Furthermore, in the case of modeling at microwave frequencies, certain problems, e. g. computation of 1 or 10 g average SAR, modeling of helices among other, were important but not satisfactorily solved. Electromagnetic interference (EMI) with implanted or body-attached medical devices was also not modeled, despite its importance both at ELF and RF. Similarly, researchers were only starting to develop human body models compatible with electromagnetic modeling. Thus, this dissertation addresses some of the problems that are essential to better understanding of field-tissue interactions. The results also contribute to the scientific database used in health protection standards.

3 Models of Human Body

The function of computer body model is to provide the information for the field solver about the spatial distribution of the electrical properties of tissues. In the real body the properties change continuously from point to point. For a computational method these properties must be discretized. In one-dimensional digital processing an analogue signal, is represented as a train of equally spaced discrete values or *samples*. In digital image processing a picture is represented by a 2-dimensional array of equally spaced light intensity values, which are picture elements or *pixels*. An extension of this scheme into 3 dimensions can represent a spatial distribution of a physical quantity such as the conductivity or permittivity as a 3-dimensional array. Such discretized quantity is assumed constant in a cuboid *volume element* or *voxel*. Since it is not practical to have a precise knowledge of electromagnetic properties of body in each voxel, it is assumed that all the voxels representing one organ or one type of tissue have the same property. With this assumption, a body can be represented by a 3-dimensional array of integer tags identifying the tissues and organs, which in turn, through the use of lookup tables provide the information of continuous physical properties such as the conductivity, relaxation parameters of Eq. 2.7 or mass density.

3.1 Development of voxel-based body models

Early body models were based on pictures in a cross-sectional anatomy atlas [16] dating back to the early 20th century. Consistency of the cross-sections taken at 1-inch (25.4 mm) intervals was not very good, since they had been compiled from many different frozen cadavers. This is evident in Figure 3-1 showing an external view of the Utah model [17], which has been derived from the atlas.

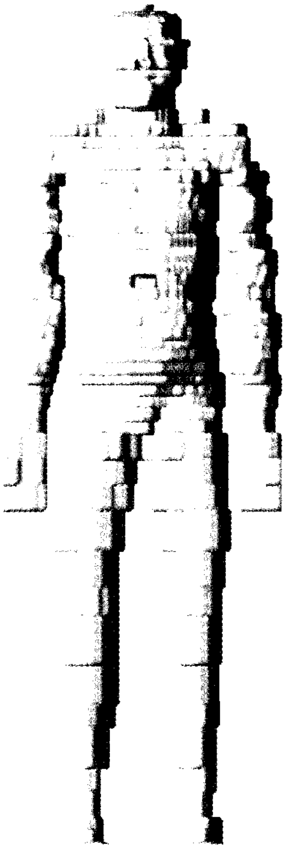

Figure 3-1 Body model based on cross-sectional atlas

Although the Utah model was initially successfully used at UVic [18], the availability of tomographic scans made it urgent to develop a more accurate model. Specifically for this task software was written for semi-automatic image segmentation, which would take a CT (or MRI) image and subdivide it into regions of similar picture density (Appendix B). A person using the program must manually classify and label the regions as belonging to given organs or tissue types. Assembling the whole body from such labeled slices is very tedious, as the process of segmentation and labeling needs to be repeated for every cross-section.

With similar software a part of our model (torso and head only) was developed by radiologists at Yale [19], based on MRI scans of a living person, a male of an average build. Concurrently with the development of Yale torso and head, the Visible Human Project (VHP) data was released [12].

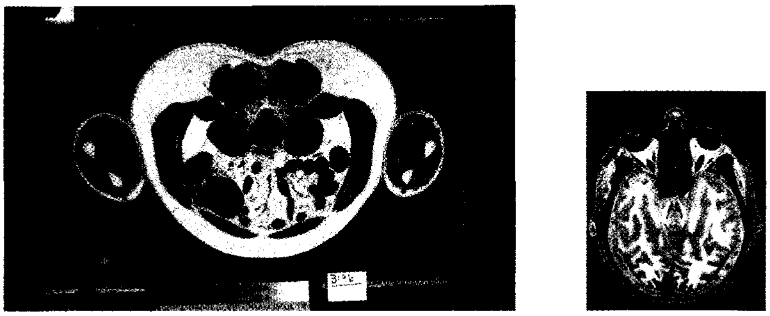

Figure 3-2 Representative slices of the Visible Human

The VHP data that are in the public domain consist of a complete set of CT scans, MRI scans and digitized color photographs of a large and heavy build male cadaver. The CT and MRI images have been taken with the separation of 5 mm and resolution of 1 mm, while the color images have been obtained at 1 mm intervals by physically slicing up the frozen cadaver and color-scanning the cross-sections with the resolution of 0.3 mm (Figure 3-2).

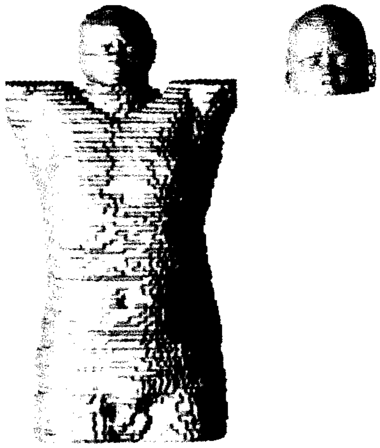

Figure 3-3 Yale model of a torso and head

The VHP model is not representative of an average male. Furthermore, converting the VHP images into a segmented body model presents a tedious task and has not been considered as a viable option. Therefore, a completion of the Yale model, as pictured in Figure 3-3, has been undertaken using the limbs derived from the VHP data.

With the use of our program for image segmentation (see Appendix B), and as a result of several weeks of a trained anatomist working with the program, a voxel model of the VHP limbs was assembled as visualized in Figure 3-4.

Figure 3-4 Model of body limbs derived from VHP data

The Yale model of torso had a resolution 3.6 mm and the upper part of the head had a resolution of 1.1 mm, while the VHP limbs had a voxel size of 5 mm. All the parts were assembled together by re-scaling and re-sampling the parts with a uniform resolution of 3.6 mm. Differences in anatomy were accommodated by re-scaling and matching the bone structure, and by expanding or contracting the malleable outer parts, consisting of fat, muscle and skin, in order to obtain undisturbed transitions between parts and a smooth outer shape of the body.

3.2 Assembly and modifications of the models

All operations on body models and model parts have been performed on a UNIX workstation using C programs written specifically for each operation. These generally are command line programs that read the model data from one or several files into 3-d arrays in memory and perform simple operations on elements of these arrays. The result is a new 3-d array of tissue tags, which is saved in a file, when the program terminates. This output file is subsequently loaded into a visualization program to assess if a desired result has been achieved. Based on a result of visual inspection, the program is modified and run again. This cycle may have to be repeated several times, with each iteration bringing the model closer to the intended form. The basic operations performed on voxel arrays are as follows:

- translation and alignment of array layers,
- Boolean operations on selected elements of 3-d arrays to include or exclude voxels based on the tissue type, location and neighboring tissues,
- smoothing out layer contours and body surface,
- insertion and removal of geometrically defined volumes of arbitrary tissue (lines, rectangles, circles, cylinders, spheres, parallelepipeds),
- application of geometrically defined masks such as parallelepipeds, spheres, ellipsoids to erase model parts or to delimit parts for translation, rotation or substitution,
- model re-sampling in a different than original resolution, and

- limbs translation and rotation to obtain different postures.

The visualization of the resulting model and a facility to inspect the volume for the locations of tissues and body structures was crucial in the iterative process of model development. Initially Matlab programs were used to visualize model cross-sections but Matlab proved to be slow in loading the models from files, and scrolling through the layer images. A dedicated program for quick model loading and fast scrolling through cross-sections was written in C using Xlib and Motif libraries to handle the display of a UNIX workstation, as described in Appendix C.

3.3 Voxel filter

A fundamental difficulty is encountered in re-sampling models in a different resolution, and in model rotations by angles other than multiples of 90 degrees. This difficulty results from a question: what tissue should be assigned to a point that falls between the voxels of not identical tissues? In the analogous situation of a 2-d image or a 3-d field of a continuous quantity such as pressure or power density, the linear interpolation between neighboring samples is usually the answer. In a more elaborate scheme for re-sampling a continuous quantity, Finite Impulse Response (FIR) filters are used [38]. These filters take a number of neighboring samples and apply different weights to them to obtain the new sample value. Unfortunately these approaches cannot be applied to voxel models, as linear interpolation between tissue types does not make biological sense.

A more appropriate approach must be based on a non-linear scheme such as used in the median filter [39]. The principle of operation is to take several neighboring samples and uses the median value of the samples as the output value.

A similar type of a non-linear filter, also based on a statistical measure, has been developed in this work to determine the tissue type in a point that falls between the samples in the original model. Instead of a median value (which requires that samples have a value which for some samples is larger and for other samples is smaller), the tissue type most common in the neighborhood is selected as the output. For this filtering a 3x3x3 voxel cube of 27 voxels is considered around the sampling point. The tissue that has the highest representation in the 27 cells is taken as the tissue in the sampling point. The characteristics of the filter can be modified by applying different weights to the center voxel, to the 6 voxels at its sides, the 8 voxels in the corners, and the remaining 12 voxels attached to the center by the edges. The tissue that has the largest weight collected within the 27 cells is considered the output of this filter.

This type of a filter has been used for a variety of tasks in developing the UVic models. These included: re-sampling the 1.1 mm head model to the 3.6 mm resolution of the body, re-sampling the 5 mm resolution of limbs to 3.6 mm, eliminating individual, spurious voxels inside the body, re-sampling limbs in rotated positions for various body postures, refinement of internal organs. All these operations were performed using a variety of experimentally determined weighting schemes for the 27-voxel masks. For instance: to eliminate discontinuities in the major blood vessels, which mostly run vertically, the blood tissue was selectively filtered with the 27-voxel mask in which the two voxels above and below the center were weighted heavier than other voxels. Presence of blood tissue in the voxel above and below the center would make blood the output tissue irrespective of what was the tissue type in the center.

3.4 The UVic model characteristics

The basic UVic model has a voxel size 3.6 mm and is described by an array of integers of

145 x 83 x 487. The model has a weight of 76 kg and height 1.76 m, which is reasonably close to the ICRP Reference Man [43]. Overall, 86 distinct organs and tissues are present as tabulated in Table A-1 in Appendix A.

A view of the UVic model surface and selected internal structures is presented in Figure 3-5.

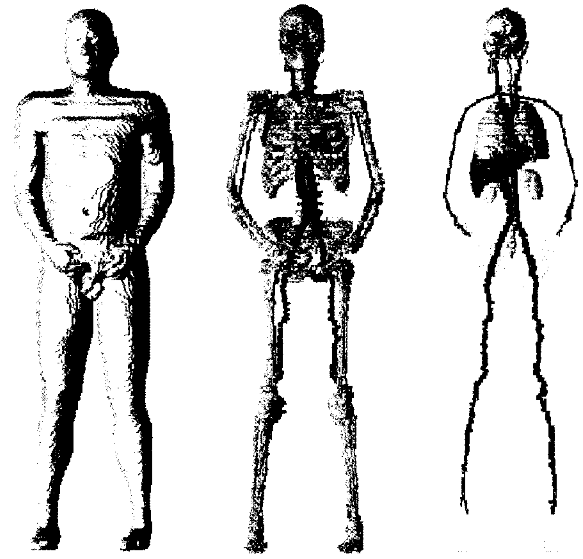

Figure 3-5 Views of UVic man model and selected organs and tissues

Many of the organs and tissues in Table A-1 are characterized by the same electrical properties. For instance, various parts of the brain can be classified as either gray or white matter. The appropriate lookup tables assigning properties to tags are put together specifically to the modeling task at hand. As an example Figure 3-6 presents a vertical cross-section through the model. Left part of the figure has color assigned according to tissue types, while the right part shows a conductivity map for the cross-section. Conductivity values in this instance are assigned to voxels according to a 60 Hz conductivity table.

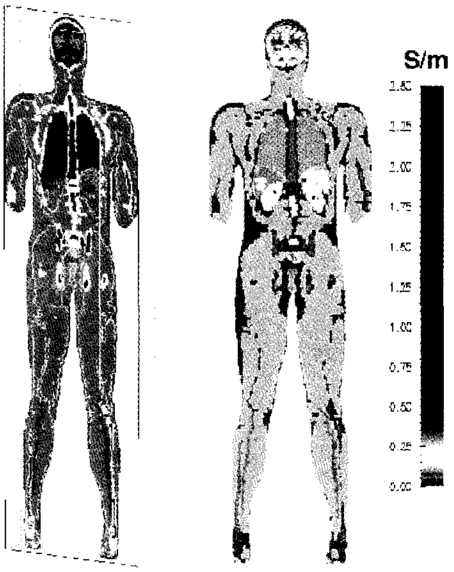

Figure 3-6 Conductivity in vertical cross-section of UVic man

3.5 Derived models

A variety of models have been derived from the basic UVic model as required by different exposure situations. Figure 3-7 shows the model in a variety of postures to represent occupational exposure of a power line worker servicing a 4-wire bundle of 500 kV transmission line.

The UVic model has also been modified to represent a child. Aside from different overall body size, a child's body is characterized by a different proportion between the head, and the rest of the body. Using the data from ICRP Reference book [43] a 5-year old child has been constructed with appropriate body proportions, as visualized in the company of the adult UVic man in Figure 3-8.

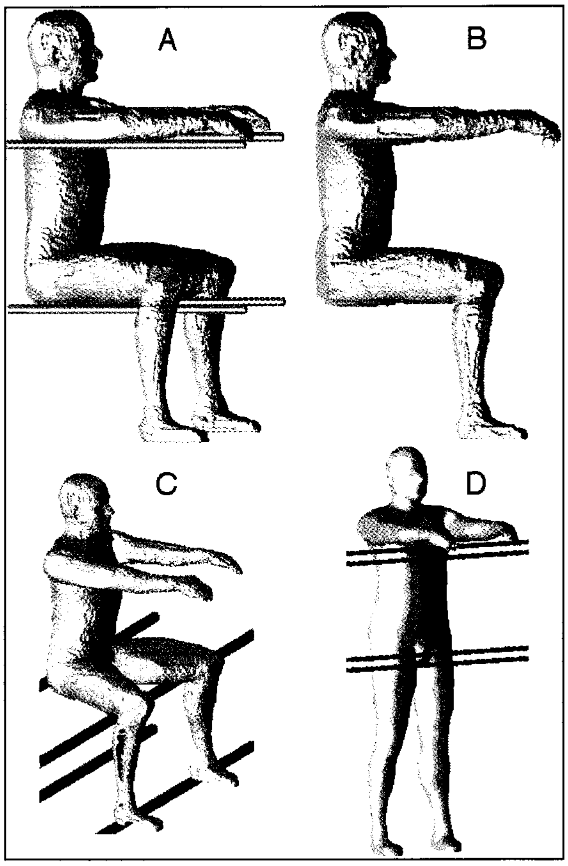

Figure 3-7 Modeling occupational exposure of a technician servicing a 500 kV transmission line

The derived models in various postures may have additional uses beyond the specific tasks for which they were originally developed. Recently, an interest has been expressed by another research group to use our models of Figure 3-7 to simulate a soldier carrying a backpack radio transmitter.

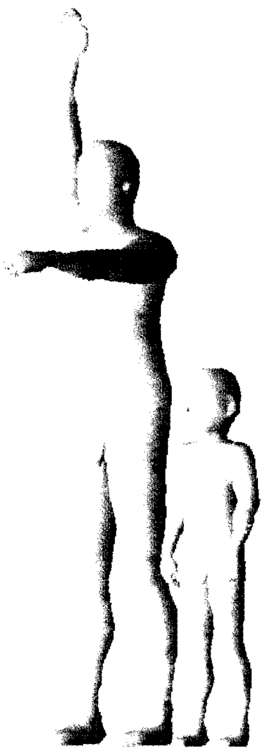

Figure 3-8 Child model visualized next to adult in one of the postures

3.6 Data formats and visualization

Computer modeling of fields using body models and the data post-processing to interpret the results always involve reading and writing data into files of a variety of formats. Two standard formats have been adopted to simplify this, namely the IBM 'general' format [40] and NCSA HDF format (www.hdf.ucsa.uiuc.edu).

For compactness of storage, the voxel body models are stored as binary data blocks, each one byte representing one voxel. The structure of these files is described in small script-like files following the syntax of 'general' files of IBM Data Explorer.

Volumetric field data, which are produced as results of numerical modeling, are stored in the HDF format. Both UVic numerical codes, SPFD and FDTD have been linked with

NCSA HDF library, to store the floating-point data as HDF matrices.

Visualization and 3-d rendering of data are important aspects of model development and post-processing of computed electric field data. All the 3-d figures in this chapter have been generated using the IBM Data Explorer (DX) visualization package. By invoking a sequence of calls to DX library a variety of visualization modes are accessed. The data can be presented as color on 3 dimensional surfaces showing model's external shape or internal structure, vector fields can be visualized by arrow glyphs or color stream-lines.

3.7 Summary

Voxel models of human body developed in this thesis have been presented. The development of the UVic man model has been accomplished using the source data of Yale torso and VHP cross-sectional data. The result is a complete 3.6 mm model of male adult in upright position. Methods and software techniques used for assembling and modifying voxel models have been developed as outlined. The subsequent model modifications and the derived models have been obtained using the developed software. Data formats and advanced volumetric data visualization techniques used throughout the research presented in this thesis have been introduced.

4 Computational Methods

There is close relationship between the mathematical description used in the body model and the computational method for solving the fields inside and around the model. Thus the models described by subdividing the volume into a number of solid elements of varying shape and size may be suitable for a Finite Element Method (FEM) solver, while models with mathematical descriptions of the surface may qualify for computing with Method of Moments (MoM) solver. For models described by subdividing the volume into a large number of cuboids the Finite Difference (FD) methods are a natural choice. The two numerical techniques that have been used in this work, namely a quasi-static Scalar-Potential Finite-Difference (SPFD) method and a full wave Finite-Difference Time-Domain (FDTD) method are described in this chapter.

4.1 Scalar-Potential Finlte-Difference Method

The SPFD method [20], [21], is a quasi-static frequency-domain technique for the computation of currents induced in a conductive body by an external AC magnetic field. Quasi-static conditions imply that at the frequency considered, the largest dimension of the conductive body under analysis is much smaller than the wavelength, and that the conductivity is low so that the secondary magnetic field due to induced eddy currents can be neglected.

The derivation of a basic SPFD begins with considering a varying magnetic field which causes a curl of the electric field (Faraday's equation)

$$\nabla\times\vec{E}=-\frac{\partial\vec{B}}{\partial t} \tag{4.1}$$

which in a material characterized by conductivity σ causes a circulating current flow $\vec{J}$ according to Ohm's law

$$\vec{J} = \sigma\vec{E} \tag{4.2}$$

$$\nabla\left(\sigma\vec{E}\right) = 0 \tag{4.3}$$

If the magnetic field is harmonic, with the radial frequency ω, Eq. 4.1 can be written as

$$\nabla\times\vec{E} = -j\omega\vec{B} \tag{4.4}$$

Expressing the magnetic field in Eq. 4.4 as a curl of a vector potential $\vec{A}$ gives

$$\nabla\times\vec{E} = -j\omega\nabla\times\vec{A} \tag{4.5}$$

Thus

$$\nabla\times\left(\vec{E} + j\omega\vec{A}\right) = 0 \tag{4.6}$$

which implies

$$\vec{E} = -\nabla\varphi - j\omega\vec{A} \tag{4.7}$$

where φ is a scalar potential. Substituting Eq. 4.7 into 4.3 gives

$$\nabla\left(\sigma\nabla\varphi + j\omega\sigma\vec{A}\right) = 0 \tag{4.8}$$

The above is the equation for an unknown scalar potential φ due to a known vector potential $\vec{A}$ in the conductive medium described by a conductivity σ.

To obtain the SPFD, the equation 4.8 is discretized over a mesh of cuboid cells (voxels) of the conductive body. Corners of the cells are the nodes in which the discrete potential φ is defined. Components x, y and z of the conductivity σ are defined along the edges of cells connecting the nodes, as averages of conductivities of the four cells touching the edge. Components of the vector potential $\vec{A}$ are also defined along the edges. Using a finite differencing scheme to replace the derivatives in Eq. 4.8 the discrete potential in a node is expressed as a function of potentials in the 6 neighboring nodes [41]

$$\varphi = \left(\sum_{n=1}^{6} \frac{\sigma_n}{\Delta_n^2} \left(\varphi_n - (-1)^n \Delta_n i\omega A_n \right) \right) \left(\sum_{n=1}^{6} \frac{\sigma_n}{\Delta_n^2} \right)^{-1} \tag{4.9}$$

where Δ_n denotes the edge length, Δ_x, Δ_y, or Δ_z, (which can be different if parallelepiped cells are used) and A_n is a component of the vector potential along the given edge in the x-, y- or z-direction. The quantities under summation are indexed to span the 6 neighboring nodes, 2 along x-, 2 along y- and 2 along z-axis according to the computational molecule [22] shown in Figure 4-1.

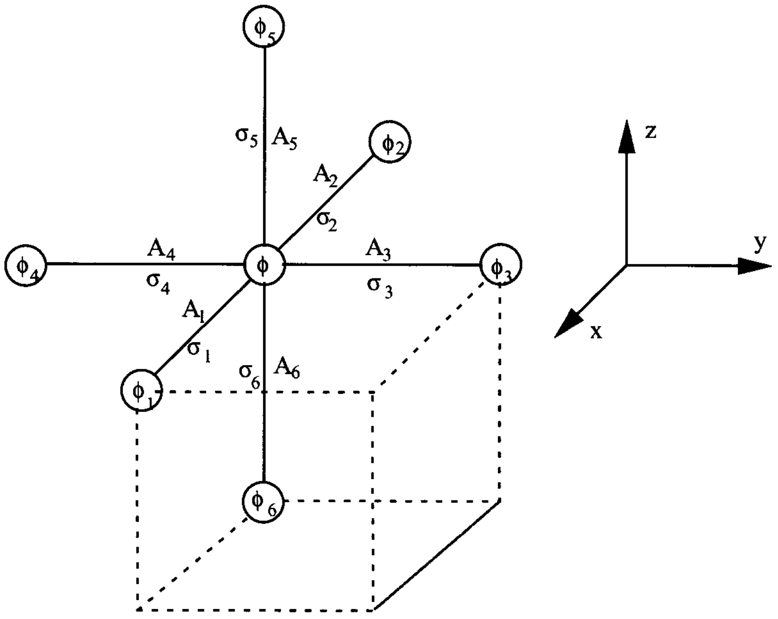

Figure 4-1 Computational molecule for the SPFD method. Mesh nodes indicated by circles, a single voxel of the conductive body shown in a dotted line.

The complete set of equations (4.2) for N nodes forms a sparse matrix of a N X N size with each row and column having at most 7 non-zero elements (fewer elements for the conductor surface nodes). This set is solved iteratively for the potential using either successive over-relaxation or conjugate gradient methods.

The UVic SPFD solver in addition to the basic operation outlined above has been enhanced to allow current injection into the surface nodes and embedding thin insulated wires for connecting pairs of nodes through the span of the mesh. The solver is written in Fortran90 and makes extensive use of scientific computational libraries such as LAPACK for efficient storage of sparse matrices, matrix conditioning and solving using the conjugate gradient method [22].

4.2 Finite-Difference Time-Domain Method

The FDTD method is based on discretizing of Maxwell's curl equations for the electric field vector, **E** and the magnetic field vector, **H**. In the staggered grid implementation invented by Kane S. Yee in 1966 [15], a grid is set up in the computational space consisting of elementary cells as depicted in Figure 4-2. By using a central differencing scheme the field components **E** and **H** in the entire space are computed in time steps in a *leapfrog* fashion:

E(t)–>**H**(t+1/2Δt) –>**E**(t+Δt))–>**H**(t+3/2Δt)–>. . .

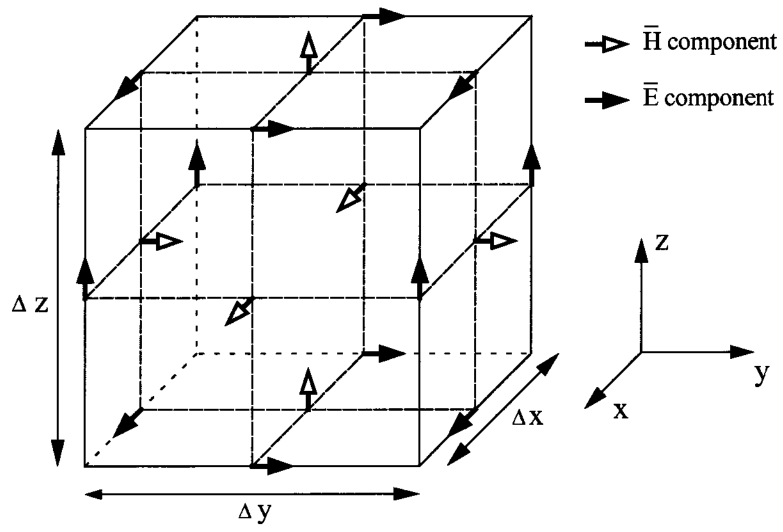

Figure 4-2 Magnetic and electric field components in Yee cell

Numerous extensions and improvements have been added to the original FDTD formulation making it arguably the most versatile electromagnetic field solver in use today. A comprehensive survey of the current state of the FDTD can be found in [23].

Many of the latest features and enhancements are included in the UVic FDTD. Written entirely in Fortran90 this program is highly portable and runs on a variety of UNIX platforms from desktop workstations to parallel supercomputers. Relevant to this work, the UVic solver supports the following enhancements:

- Perfectly Matched Layer (PML), and Generalized Perfectly Matched Layer (GPML) boundary conditions
- graded and sub-gridded meshes
- lossy and dispersive dielectrics
- frequency domain observations of fields based on the Fourier Transform
- near-to-far-field transformation of radiated energy
- inclusion in computational space of voxel discretized dielectrics

- dielectric averaging for re-sampling voxel models on graded meshes
- conformal treatment of metals and dielectrics
- surface impedance materials
- accurate modeling of thin wires and slots (smaller in diameter than grid size)

4.3 SPFD and FDTD code on parallel supercomputer

The new supercomputer facility of UVic, the IBM SP2 MINERVA consists of 8 nodes connected by a fast network, and each node has 16 processors working in parallel in the Symmetric Multi-Processing (SMP) architecture and is equipped with the shared memory of 8 GB. The availability of this machine made it possible to solve problems that are larger and more computationally intense than previously attainable.

Due to high portability of Fortran90 code both SPFD and FDTD codes compiled on MINERVA with only minor code modifications. An additional work was required to take advantage of multiprocessor architecture. In the instance of SPFD the parallelization was accomplished by linking the pre-compiled parallel versions of LAPACK library, which comprises the conjugate gradient matrix solver.

More effort was needed to parallelize the FDTD code. Although the UVic FDTD code was originally written for parallel execution on SGI machines, significant code modifications were necessary to successfully spread the execution of the FDTD field update over several processors of the IBM machine. Only SMP parallelization was implemented which is done semi-automatically by placing OpenMP directives around the critical loops of the program and giving appropriate options to the compiler to act on these directives.

Efficiency or scaling of parallel execution is described by a fractional number giving the ratio of the processing speed on multiple CPUs to the processing speed of a single CPU multiplied by the number of CPUs. Ideally this ratio should be 100%. Actually observed ratio is always less (except when entire programs may fit into cache for larger number of CPUs which may result in the so called super-linear speed-up) and it is a function of the computer architecture (how fast is the switch connecting CPUs with various areas of memory) and the code itself. In experiments with MINERVA it has been found that scaling is quite good for up to 8 processors, but very little additional gain of speed is achieved beyond that. In some instances the code executed 20% faster on 16 processors than on 8, in other instances there was even less gain. Most likely this is a shortcoming of the architecture or the operating system scheduler. On the other hand, good scaling was observed when using 3 CPUs (80%) or 6 CPUs (75%) while very little speed gain was observed when going from 3 to 4 CPU or from 6 to 7. This is due to the chosen method of parallelization, which was to run the x-, y- and z-field component update in parallel. If the number of CPUs is not divisible by three this part of the code runs inefficiently.

To handle very large data sets (very detailed models) both the SPFD and FDTD have been compiled using IBM's 64-bit libraries. This allows for the total memory usage by a single program to go beyond 2 GB limit. Running the FDTD code with 3.6 mm body model and the SPFD code with 2 mm model, both required using the 64-bit addressing to allocate memory for the required computational space.

The SP2 versions of SPFD and FDTD codes obtained for this project have proven useful for other researchers pursuing large scale computations of EM fields, e.g. Dawson [84], Fear [83], Hirata [79] and Rahman [82].

4.4 Summary

Two previously developed numerical codes have been used in this thesis. However, for solution of the problems of interest, significant modifications of the codes have been necessary. Particularly important has been making the codes work on a large parallel supercomputer.

Numerical codes SPFD and FDTD have been ported to UVic parallel supercomputer MINERVA for solving very large problems involving full body models in 2 mm and 3.6 mm resolutions. Up to 70% scaling have been achieved when running the codes parallel on 8 CPUs.

The supercomputer versions of codes that have been obtained are also applicable to solving other large problems in the areas of antenna research, EMI, remote sensing etc.

5 SAR Computation

Specific Absorption Rate (SAR) as defined by Eq. 2.3 is a volume-averaged quantity, which is dependent on the shape and size of the volume ΔV used. In the early regulations for RF exposure the whole volume of the body has been used for averaging. The highly localized nature of power distribution from handheld transmitters made it necessary to use smaller averaging volumes. In the recently introduced regulations in the US [71] and guidelines in Europe [72], a cube of tissue weighing 1 g or 10 g is used as the averaging volume. For compliance with these regulations, the averaged SAR must not exceed a specified value. The guidelines do not specify how the averaging should be done, neither do they give any specifics regarding air inclusions in the cube volume. While the SAR has been evaluated for mobile devices, such as cellular telephones, (e.g. [64], [65], [66]), little specific information has been given on how the 1 g or 10 g values have been obtained. In one instance [66], variously shaped volumes, instead of cubes, are considered close to the peak SAR and interpolation is used to arrive at 1 g average. In this instance 20 % of the volume considered can be occupied by air.

5.1 FDTD computation of absorbed power

In the standard FDTD implementation, dielectric boundaries are aligned with the E grid and thus the Yee cell in Figure 4-2 is uniformly filled with a dielectric of a complex permittivity ε^*.

$$\varepsilon^* = \varepsilon' - j\varepsilon'' \tag{5.1}$$

As discussed in Section 2.4, biological tissues are characterized by the permeability equal to that of free space and thus the power absorbed in the tissue is due to the imaginary part of complex permittivity ε^*. Both real and imaginary parts of complex permittivity depend on a frequency as described by the 4-pole Cole-Cole dispersion of Eq. 2.7. For a single frequency ω the permittivity of Eq. 4.1 can be expressed as equivalent conductivity σ

$$\varepsilon^* = \varepsilon' - j\frac{\sigma}{\omega\varepsilon_o} \tag{5.2}$$

In the FDTD grid the conductivities are defined along the Yee cell edges to coincide in space with the E-field components. When the dielectric boundaries are aligned with the E-grid, the E-field components of a Yee cell are tangential to dielectric interfaces and as such are continuous across the interfaces. Therefore, at a given edge the conductivity can be taken as an arithmetic mean of the four conductivities of Yee cells meeting on this edge. It should be noted that this may not apply to a general case of dielectric interfaces cutting through the Yee cells at arbitrary angles because of the presence of E components normal to the interfaces. That case is still an object of active research [24], [25], and is not considered here.

Power density absorbed in the conductivity σ along the x-edge of a Yee cell from the sinusoidal field of the amplitude E_x is given by

$$P_x = \frac{|E_x|^2 \sigma}{2} \tag{5.3}$$

Field amplitudes Ex, Ey, Ez at a frequency ω are obtained in FDTD at run-time with the recursive Fourier transform. At the end of the run the magnitudes are squared and multiplied by the conductivities resulting in 3 power density fields P_x, P_y and P_z. The total power density is a sum of P_x, P_y and P_z however, there is a complication due to the fact that these components are not co-located. There are three possibilities of combining these partial power fields into a single scalar field of absorbed power density, namely, the three-, six- and twelve-field-component approach. The three-field approach (Figure 5-1a) is the least accurate method as components from different spatial locations are added. In the six-field components approach (Figure 5-1b) interpolation is used to place all field components in the cell node. The twelve-field-component approach (Figure 5-1c) interpolates all field components in the center of the voxel. The latter provides direct mapping of the power field into the body model. Thus using the twelve-component interpolation, power totals absorbed in organs and tissues can be easily computed.

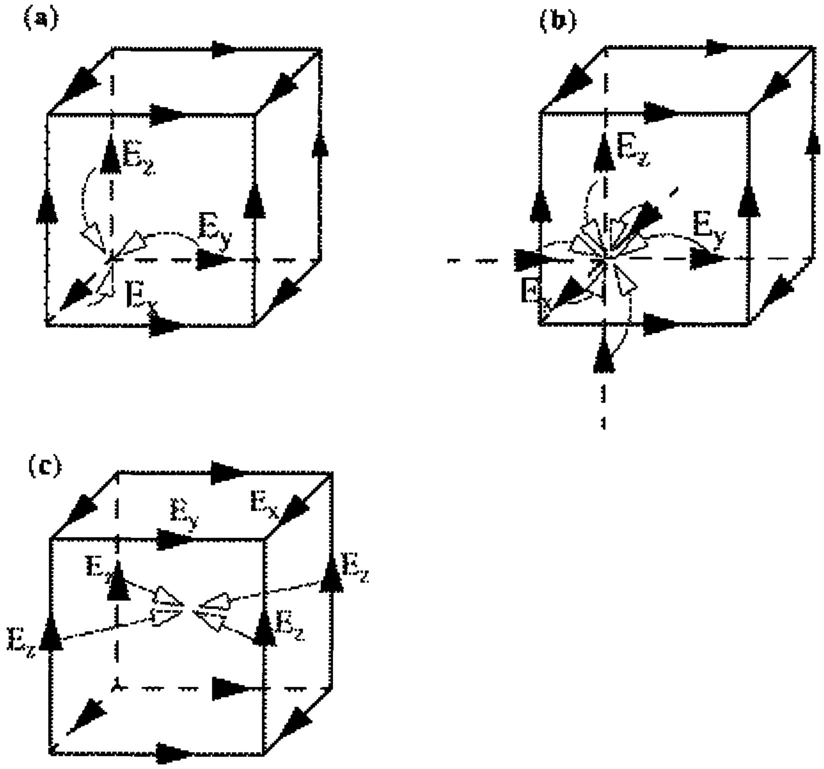

Figure 5-1 Combining Ex, Ey and Ez contributions to the total power absorbed in Yee cell: (a) three-field, (b) six-field, (c) twelve-field approach

5.2 Improved twelve-field algorithm

In the standard twelve-field approach the x, y, or z component of E field in the Yee cell center is taken as an arithmetic mean of the edge defined values as obtained by FDTD. Considering the *i,j,k* subscripts denoting the position of a cell, and *Ex* the x-component of the edge defined field, the cell center x-component *Exc* is given by

$$Exc_{ijk} = \frac{Ex_{ijk} + Ex_{ij+1k} + Ex_{ijk+1} + Ex_{ij+1k+1}}{4} \tag{5.4}$$

The same operation is repeated for the four edges along y-axis to obtain *Eyc* and along z-axis for *Ezc*.

Similar linear interpolation has been used to bring the power obtained in the locations along cell edges to the center of the cell. Although satisfying the energy conservation for the whole volume, this method deposits some power into empty voxels immediately adjacent to voxels with lossy dielectric, which obviously is not correct. To derive a proper expression for power interpolation consider Figure 5-2.

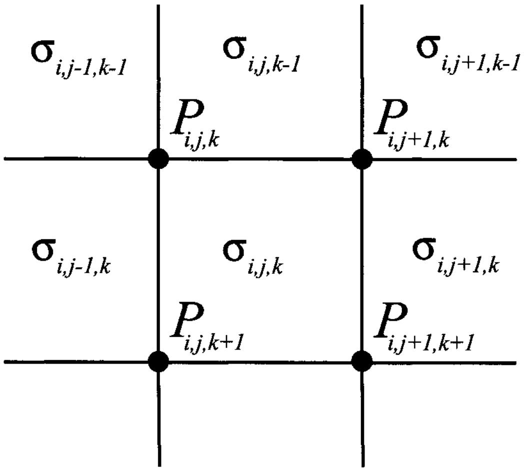

Figure 5-2 The x-plane cross-section through dielectric voxels in FDTD grid, power densities *P* are defined along x-edges, conductivities σ constant in voxels

In Figure 5-2 the x-edges of Yee cells are shown as the nodes of a 2D grid. In the standard treatment of dielectrics in FDTD the dielectric voxels are aligned with the E-grid. Power density $P_{i,j,k}$ as given by Eq. 5.3, is a result of the generally unequal contributions of the four cells meeting on the edge and can be written as

$$P_{ijk} = \frac{E^2_{ijk}}{2} \frac{\sigma_{ijk} + \sigma_{ij-1k} + \sigma_{ijk-1} + \sigma_{ij-1k-1}}{4} \tag{5.5}$$

Thus, each of the four voxels contributes to the power at the voxel edge proportionally to its conductivity. This must be taken into account to properly compute the power density in the volume of voxel σ_{ijk} from its edge power densities. Considering the middle voxel of Figure 5-2, a fraction P_1 of edge power P_{ijk} that 'belongs' to that voxel is:

$$P_1 = P_{ijk} \frac{\sigma_{ijk}}{\sigma_{ijk} + \sigma_{ij-1k} + \sigma_{ijk-1} + \sigma_{ij-1k-1}} \tag{5.6}$$

Similarly the fractions P_2 - P_4 of the remaining three edges are obtained from the conductivities of the voxels touching each edge, and combined for the total power density in the voxel volume due to x-component of the E-field. The same operation is repeated for the y and z-components for a correct 12-component voxel power interpolation. Simple arithmetic proves that this method also conserves the power in the whole volume but redistributes it only in the cells with lossy dielectric and not in free space.

5.3 Weight averaged SAR

Considering tissue density ρ, and power density P, the SAR for a single voxel of tissue at a grid position (i,j,k) is given by

$$SAR_{ijk} = \frac{P_{ijk}}{\rho_{ijk}} \tag{5.7}$$

A cube of tissue weighing 1 or 10 g as required for SAR average needs to be assembled from a number of voxels, which will depend on the volume of individual voxels and the density of tissues represented by the voxels. To meet the compliance with the standard the entire volume of the body needs to be searched with the cubical averaging volume to determine the location and value of maximum SAR. The following algorithms have been developed for this purpose.

5.4 SAR algorithm for uniform grid

For a simpler case of a uniform mesh ($\Delta x = \Delta y = \Delta z$), the algorithm for the mass average SAR in a sampling point (X in Figure 5-3) proceeds as follows:

(i) A sequence of cubes of increasing size (single voxel, 3 x 3 x 3, 5 x 5 x 5, etc.) is built by adding a layer of voxels to the previous cube until its mass is equal or larger than the required mass. In each expansion step it is verified that at least one voxel with tissue is present on every face of the new layer and that inside the cube the percentage of empty voxels does not exceed a preset value selected by the user and typically 5% - 20%. If this condition is not satisfied, the SAR is considered indeterminate. The last cube in the sequence with a mass less than required is considered the *core* of the sought cubic volume.

(ii) A cubic equation is solved to compute the fraction $f = dx/\Delta x$ (Figure 5-3) of the additional layer that needs to be added to the core in order to obtain the required averaging mass. This equation is

$$cf^3 + ef^2 + sf - k = 0 \tag{5.8}$$

where c is the total mass of 8 corners, e is the total mass of 12 edges, s is the total mass of 6 sides, $f = dx/\Delta x$, and k is the required fraction of the outer layer mass.

(iii) The power of core elements and weighted power contributions of the sides, edges and corners are added using appropriate powers of f as weights. SAR is computed by dividing thus obtained total power by the required averaging mass.

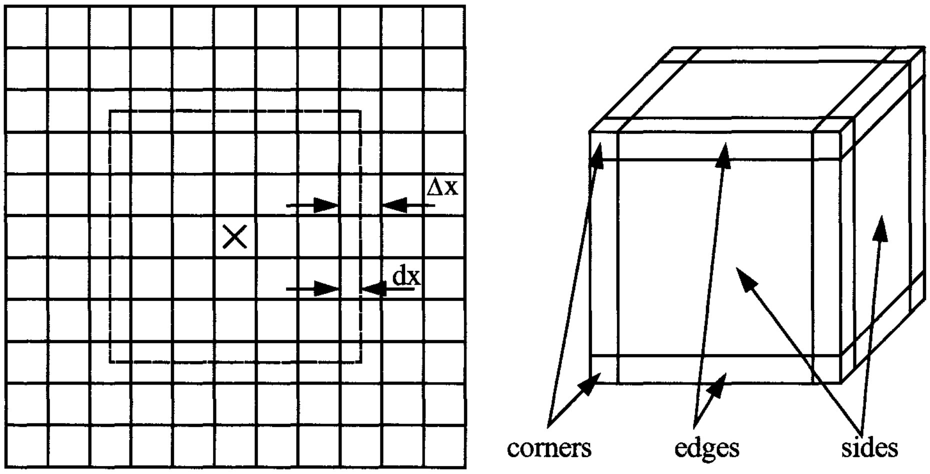

Figure 5-3 Cubical volume for mass averaged SAR

5.5 SAR algorithm for non-uniform grid

In many of the problems solved with FDTD codes, the meshes other than uniform in three directions are used. The main varieties of meshes are: uniform non-homogenous meshes, graded meshes, sub-gridded meshes, and combinations of these. The algorithm appropriate for complex meshes is based on the idea of progressively assembling a cube shaped volume of voxels surrounding the sampling point until a big enough volume is created to have the required mass. The algorithm for non-uniform mesh is illustrated in Figure 5-4, which shows an example of a slightly exaggerated non-uniform mesh. More typically in graded meshes the adjacent cell size ratio in any direction should not be higher than 1:1.3.

With respect to Figure 5-4 assembling a cubic volume of required mass progresses as follows:

(i) The initial core is defined as all the voxels within the cubic volume based on the longest side of the voxel that contains point X in which SAR is evaluated (dashed outline in Figure 5-4 a).

(ii) The masses of the core and of the single layer of tissue (outer layer) surrounding the core (Figure 5-4 b) are added. If the computed mass is less than required, the core is expanded by adding another single layer of voxels to a selected wall of the core. The wall whose external boundary is nearest to the SAR sampling point X is selected for this expansion.

(iii) Step (ii) is repeated until the mass computed is greater than required averaging mass.

The growth of the core after 2 and 6 iterations of (ii) is shown in Figure 5-4 b and c.

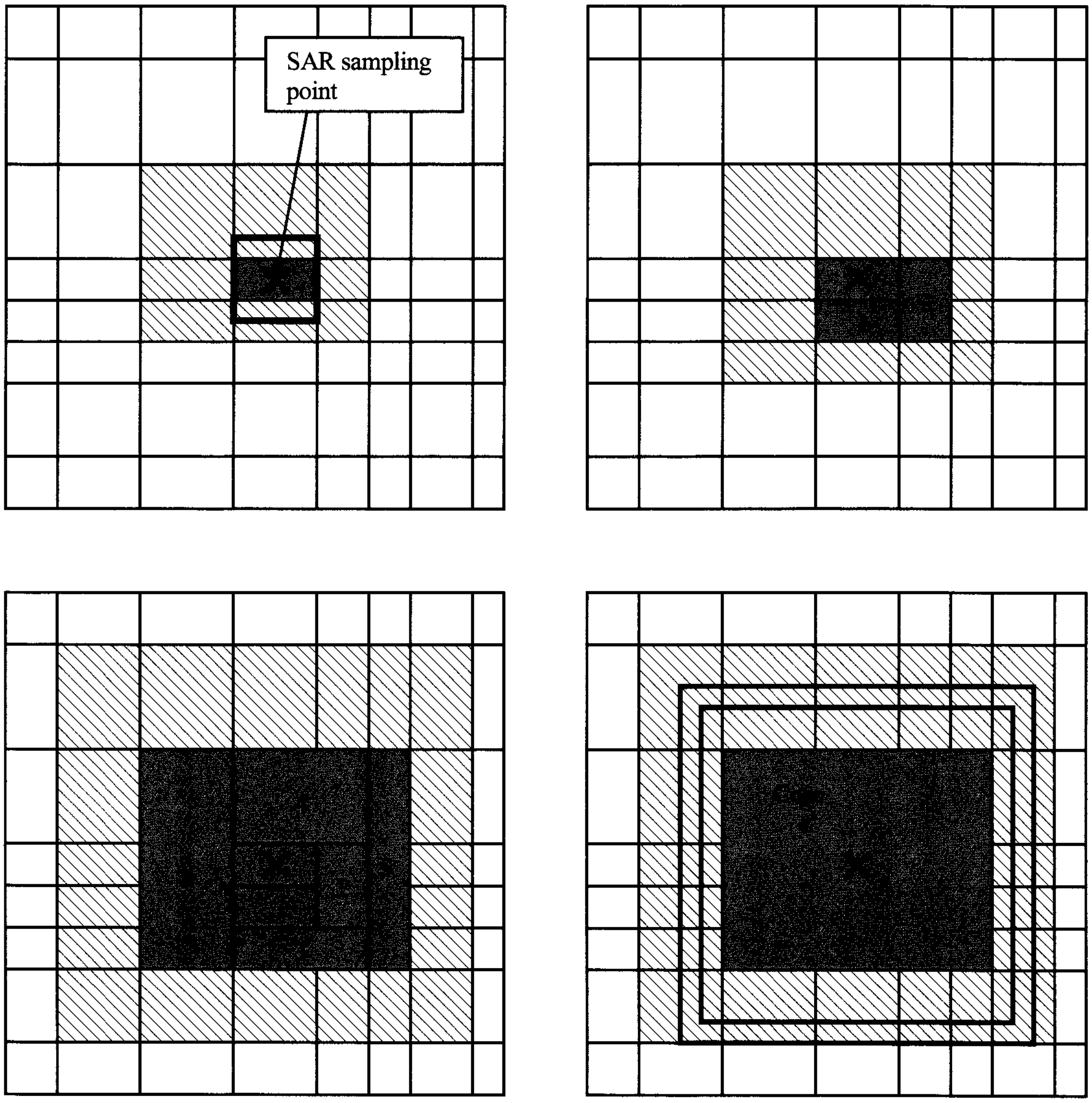

Figure 5-4 Cube volume building in a non-uniform mesh

(iv) The largest cube centered at point X and entirely within the volume defined in (ii) is created, as shown by the dashed line in Figure 5-4d. This volume encompasses the entire core and is contained within one layer of cells outside the core (cross-hatched area in

Figure 5-4 d.)

(v) If the mass of the core and the fraction of the layer contained in the dashed cube is still less than required, the core is further expanded as in steps (ii) - (v).

(vi) The exact size of the required cube is computed by simple iteration within the boundaries defined by the largest and smallest cubes whose surfaces are contained within the outer layer and which are centered on the sampling point. Having determined the cube volume of the required mass the contributions of power density from the outer layer are added to the SAR average in the same proportions as fractional voxels of the outer layer contributed to the required mass.

5.6 Computing SAR by linear Interpolation

For comparison with the new algorithms a simpler method of linear interpolation of SAR results is also implemented. This method relies on computing the 1 g or 10 g average SAR based on the power deposited in two cubical volumes made of full voxels, one of which has lower and one higher mass than required. SAR averaged over the required mass is obtained by linear interpolation between the two cubical volumes

$$SAR_g = \frac{P_1 + (P_2 - P_1)\dfrac{m_g - m_1}{m_2 - m_1}}{m_g} \tag{5.9}$$

where: SAR_g is the SAR averaged over the required mass, (usually 1 g or 10 g) m_g is the required mass, P_l is the power deposited in the cube of the mass m_l which is lower than

m_g and P_2 is the power deposited in the cube of mass m_2 which is higher than m_g.

The linear interpolation in its simple form outlined above is not directly applicable to non-uniform and graded meshes.

5.7 Numerical verification

A. Power Distribution: Number of Field Components in Averaging

An evaluation of the effect of the number of electric field components on the computed power deposited in a voxel has been performed for a canonical problem of a two-layer sphere irradiated by a resonant dipole. The sphere dimensions were: outer radius 11.2 cm and inner radius 10.7 cm. The electrical properties of the outer layer simulated those of the bone with $\varepsilon' = 12.5$, $\sigma = 0.13$ S/m and $\rho = 1.85$ g/ml. The inner sphere properties were those of the brain with $\varepsilon' = 44$, $\sigma = 0.9$ S/m and $\rho = 1$ g/ml. The dipole was resonant at 835 MHz and in all cases data were normalized to constant output power of the antenna (power radiated plus total power absorbed in the sphere). Table 1 presents the comparison for three dipole locations and uniform and graded meshes. The data are presented in terms of the 1 g average SAR. Thus, while the 3 component averaging is not accurate for mass-averaged SAR evaluation, either 6 or 12 component averaging can be used with minimal effect on the accuracy of the computed value.

Table 5-1 Maximum SAR averaged over 1 g of mass of cubical shape computed using three different methods of combining electric field components.

Dipole Location	Mesh	SAR, 1 g (W/kg)			Difference (%)	
		3 component	6 component	12 component	3 & 12 component	6 & 12 component
10 mm	graded 2x2x5 mm	8.93	8.47	8.46	5.4	0.1
	uniform 5 mm	8.06	7.13	7.07	14	0.7
20 mm	graded 2x2x5 mm	4.43	4.17	4.17	6	0
	uniform 5 mm	4.32	3.92	3.91	10	0.2
50 mm	graded 2x2x5 mm	0.92	0.87	0.86	5.7	0.3
	uniform 5 mm	0.90	0.85	0.85	6	0

B. SAR Algorithms

Average SARs for 1 and 10 g were computed with the new algorithm for uniform and graded meshes for a human head in the proximity of a cellular telephone. An anatomically realistic model of the human head and a typical telephone in the usual (tilted) position were modeled at 840 MHz with the FDTD method [63]. A uniform grid of 2 mm and a graded mesh varying from 1 mm to 2 mm with expansion coefficient 1.25 were used. Values within 0.03 % were obtained by the two new algorithms compared to the linear interpolation for the uniform mesh only. However, the SAR distribution was very smooth. Within the 125 voxels that comprised the 1 g cube, at the point of maximum SAR the standard deviation of voxel SARs was only 7%. In this case, the new algorithm is only superior for graded meshes, as linear interpolation becomes difficult.

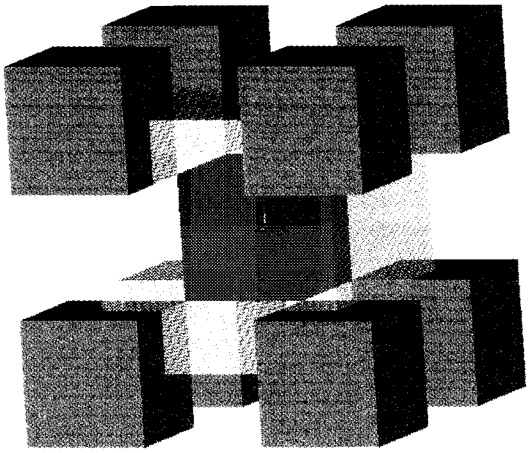

Figure 5-5 A test case of 9 voxels of CSF interspersed with 18 voxels of fat (invisible). Shaded is the one gram volume cut out of the 27 voxel cube depicted

To illustrate a case where the new algorithm performs, while linear interpolation fails, another artificial, but realistic situation of tissue configuration, shown in Figure 5-5, is evaluated. The tissue consists of 27 voxels in a 3 x 3 x 3 cube, with a voxel size of 5 mm. The voxels are CSF ($\sigma = 2.4$ S/m), and the blank voxels are fat ($\sigma = 0.04$ S/m). For this configuration, the new algorithm adds a 2.5 mm thick layer around the center voxel. In the linear interpolation 7/26 of the outer layer is added to the 0.125 g core to obtain the 1 g mass. The error due to linear interpolation in this procedure is over 50%.

5.8 Summary

Algorithms have been developed and tested for accurate automatic computation of mass-averaged SARs (typically 1 g or 10 g average) from the FDTD data for heterogeneous tissue models. The algorithms apply to uniform and non-uniform meshes. The accuracy of the algorithms is practically the same as that of linear interpolation for fine meshes (2 mm) and smooth spatial distribution of the local SARs. Their performance is clearly superior for large SAR gradients and a coarse mesh. Also, it has been established that for accurate computation of the cube-averaged SAR, and for computing organ averages, the 12 electric field components must be used to obtain a voxel-total electric field.

6 Verification of Modeling Codes

6.1 ELF Field Modeling - Comparison study of currents induced in body models by 50/60 Hz magnetic field

To assess the reliability of data obtained by using anatomy based body models and numerical methods, a joint study has been conducted with the National Radiological Protection Board (NRPB) in UK to compare the dosimetry of power frequency magnetic fields. Two body models were used by both groups: the 3.6 mm model developed at UVic (Chapter 3) and 2 mm model developed by NRPB. Each group applied its own, independently developed field solver based on the SPFD method (Chapter 4).

6.1.1 **Rationale**

Numerical modeling involving realistic tissue conductivity representations of the human body has been extensively used in recent years. Such modeling allows for establishing the relationship between the external (exposure) field and the induced internal electric fields and current densities. The induced current density is often used as a benchmark for exposure levels in safety guidelines, e.g., ICNIRP (1998) uses 2 mAm^{-2} and 10 mAm^{-2}, as limits for the general population and occupational exposure, respectively. For exposures to non-uniform magnetic fields, numerical modeling provides the only practical solution for realistic evaluation of compliance.

A few research groups have published data from modeling of human exposure to 50 or 60 Hz uniform magnetic fields [41[, [44], [47]. Some occupational exposures have also been modeled [48], [49].

The anatomy of human body models used by different groups, their resolution (voxel size), and the conductivities of tissues were not identical. Each of these factors is well known to influence the induced fields. Quantitative differences for resolution and conductivity have been evaluated [47], [52]. A comparison of data from three laboratories indicates differences in induced field strengths that range from a few percent (3 – 5%) to factor of two for some voxel maxima [53]. These differences can be explained by the differences in the models anatomy, resolution and tissue conductivity, as well as the inevitable errors associated with the maximum values [51]. Nevertheless, the reliability of numerical modeling has been questioned by scientists not directly involved in computational electromagnetics, despite extensive verification of the methods and codes used by all groups. The research presented here has been undertaken to address the underlying perception of possible problems with numerical modeling.

Three models of the human body have been used in this investigation. Data for two models have been independently computed in two laboratories, and comparisons are given of average, maximum and 99 percentile values for over 30 organs and tissues. Additional data are obtained on the effects of model anatomy and resolution, by using several variations of models with the same field solver and tissue conductivity values.

6.1.2 Body Models

Essential characteristics of the models are summarized in Table 6-1, and an illustration is given in Figure 6-1. "NORMAN", the model developed by NRPB [42] has an anatomy that is the closest to the International Commission for Radiological Protection (ICRP) Reference Man [43]. The "UVic" model, as described in Chapter 3, is reasonably representative of an average man.

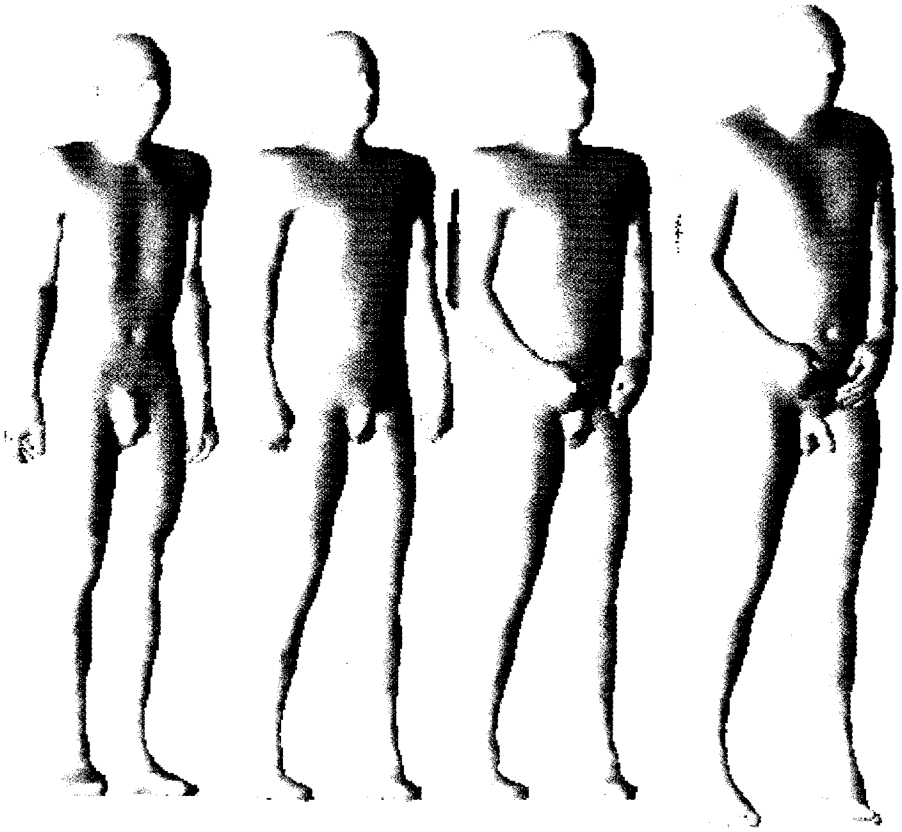

Figure 6-1 Models used in comparison, from left to right: NORMAN, UVic with arms down, UVic with arms in front, AF model.

There are two versions of the UVic model; one has the arms on the sides, and the other in front (Figure 6-1). The "AF" model taken from (http://www.brooks.af.mil) represents a larger man. To obtain a sufficient number of models for comparison, NORMAN has been re-sampled from its original resolution of approximately 2 mm to 4 mm. The UVic model has been subdivided into smaller voxels of 1.8 mm. However, while these data are useful for comparisons, this model does not genuinely represent the anatomy with the fine resolutions for apparent reasons. The AF model has also been re-sampled to 2-mm resolution, and edited to correct a few minor errors in its anatomy (e.g., missing skin in a few boundary voxels).

Table 6-1 Characteristics of human body models.

Model	NORMAN	UVic	AF
Height	1.76 m.	1.77 m	1.80 m
Mass	73 kg	76 kg	104 kg
Original Voxel	2^* mm	3.6 mm	1 mm
Voxel in computations	2^* & 4 mm	1.8 & 3.6 mm	2 mm

* The actual voxel sizes are 2.077 mm in the horizontal dimensions and 2.021 mm in vertical.

In all computations a uniform magnetic field is oriented front-to-back and conductivity values from [29] are allocated to tissues for the three models. The original divisions into body parts are somewhat different for the three models, particularly for parts of the same tissue and small organs such as glands. Computations at the NRPB were performed at 50 Hz and the data re-scaled to 60 Hz; thus all data presented are for 1 μT at 60 Hz.

6.1.3 Computational Methods

The numerical modeling in both laboratories uses the quasi-static approximation and the scalar-potential finite difference-method (SPFD). However, the actual computer codes have been developed entirely independently, and thus are quite different. For instance, the NRPB code uses successive over relaxation rather than a conjugate gradient matrix solver used at UVic. Results obtained with the SPFD are practically identical to those obtained with the impedance method, but at a lower computational cost [41]. Post-processing to obtain the average, 99 percentile and maximum values of organ/tissue measures has been done at UVic on the raw field data submitted by CRPB. In all cases, three orthogonal components of the electric field in voxel centers are vectorially summed.

The detailed results of data obtained at UVic and NRPB are shown in Apendix D.

6.2 Verification of FDTD at ceiluiar phone frequencies

For the FDTD code verification, use of an analytic solution for a conductive sphere is universally accepted as a suitable method, e.g. [46]. The analytical solution based on Mie series [45] of plane wave scattering by a lossy dielectric sphere provides such a solution. Typically, only electric fields along the principal axis are considered [81]. However, experience with verification using a sphere [51], indicates that values of fields along other axes and in other locations need to be compared.

6.2.1 Mie series computation

A Mie series is computed using a Fortran code developed at the University of Utah [46]. Since only E-fields along the principal axes are computed in this code, it had to be modified to produce the data for the whole volume. The modified version computes the E-field on an arbitrary 3-d grid of points.

A sphere of lossy dielectric placed at the origin of coordinate system has a diameter of 30 cm and is illuminated by a plane wave of 900 MHz and E-field amplitude 1V/m propagating along the y-axis and polarized along the z-axis. The dielectric is characterized by ε_r = 39.4 and σ = 0.694 (arithmetic mean of white and gray brain tissues at 900 MHz). Symmetry of the problem allows for computing the Mie solution for one quarter of the cube encompassing the sphere – only positive values of x- and z-coordinates need to be considered, while in the direction of propagation along y the whole span of the sphere is used. A grid of points aligned with the FDTD mesh is used for the computation. As determined by testing, at 900 MHz 15 terms of Mie series are necessary to bring the solution within the limits of numerical resolution (in single precision output data). Field components Ex, Ey, and Ez are combined as an RMS value, which is stored in a data file when the program terminates.

6.2.2 FDTD computation

The 300-mm sphere with $\varepsilon_r = 39.4$ and $\sigma = 0.694$ is centered in a cubical FDTD volume measuring 332 mm per side and discretized either on a 2 mm grid or on a 1 mm grid. A total-scattered FDTD formulation is used [23], with a z-polarized plane wave propagating along the y-axis. A frequency shifted Gauss impulse with a center frequency 900 MHz and bandwidth 900 MHz is used as a time excitation. The FDTD grid is terminated with a six-layer Perfectly Matched Layer (PML) boundary [23] on all sides. Fourier observations of Ex, Ey, and Ez at 900 MHz are recorded within the whole FDTD volume. Two complete FDTD simulations are performed for each resolution, one without and one with the dielectric sphere. The field recorded without the sphere is used to normalize the 900 MHz plane wave to the amplitude of 1 V/m.

In the post-processing, the recorded Ex, Ey, and Ez are interpolated to voxel centers using Eq. 6.1, squared and summed under square root to obtain the RMS value.

6.2.3 Comparison of FDTD with analytical solution

Figure 6-2 presents the comparison of fields inside the sphere along its principle axes obtained using Mie series expansion (continuous line) and the FDTD (dotted line). The red plot is for the y-axis along which the wave propagates. The decay of magnitude is a result of the wave attenuation as it propagates in the lossy medium. The black plot is along the z-axis, which is perpendicular to the direction of propagation and parallel to the E-vector of the incident wave, and the blue plot refers to the x-axis. As confirmed by the symmetry of the plots, the black and blue plots are in the plane perpendicular to the direction of propagation.

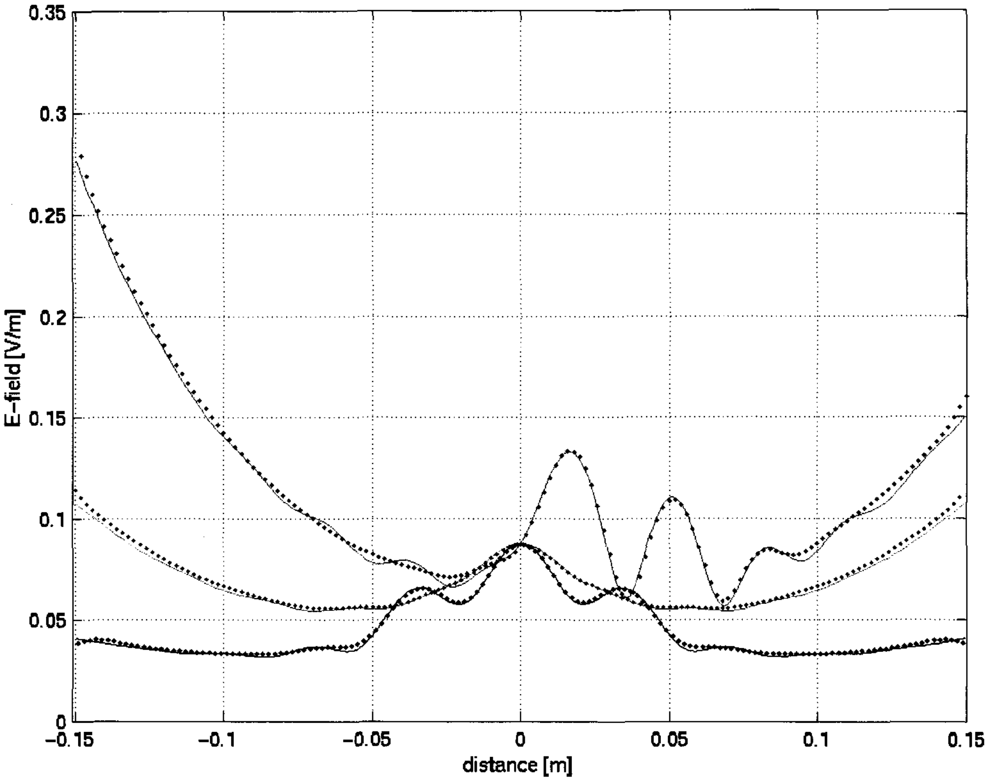

Figure 6-2 Comparison of E-field magnitude along the principal axes inside dielectric sphere, illuminated by 900 MHz plane wave propagating in positive direction of y-axis. Analytical solution plotted as continuous line and the FDTD solution dotted. Field distributions along x-axis are shown in blue, y-axis red, and z-axis black.

As evident from the plots, the differences between FDTD and Mie solution on principal axes of the sphere are small. This is confirmed by statistical analysis. The standard deviation of FDTD data (assuming exactness of the analytical solution) for x-, y-, and z-axis is 2.6%, 2.7% and 2.7% respectively.

Considering the data for the entire volume, the standard deviation is greater, namely

5.7%, while the mean absolute error for the whole volume is 2.0%. This is not unexpected, since it has been shown that staircased surfaces in FDTD (such as the sphere considered here) are subject to field singularity errors [51]. A few high error values lead to relatively larger increase in the standard deviation than the increase in the mean error.

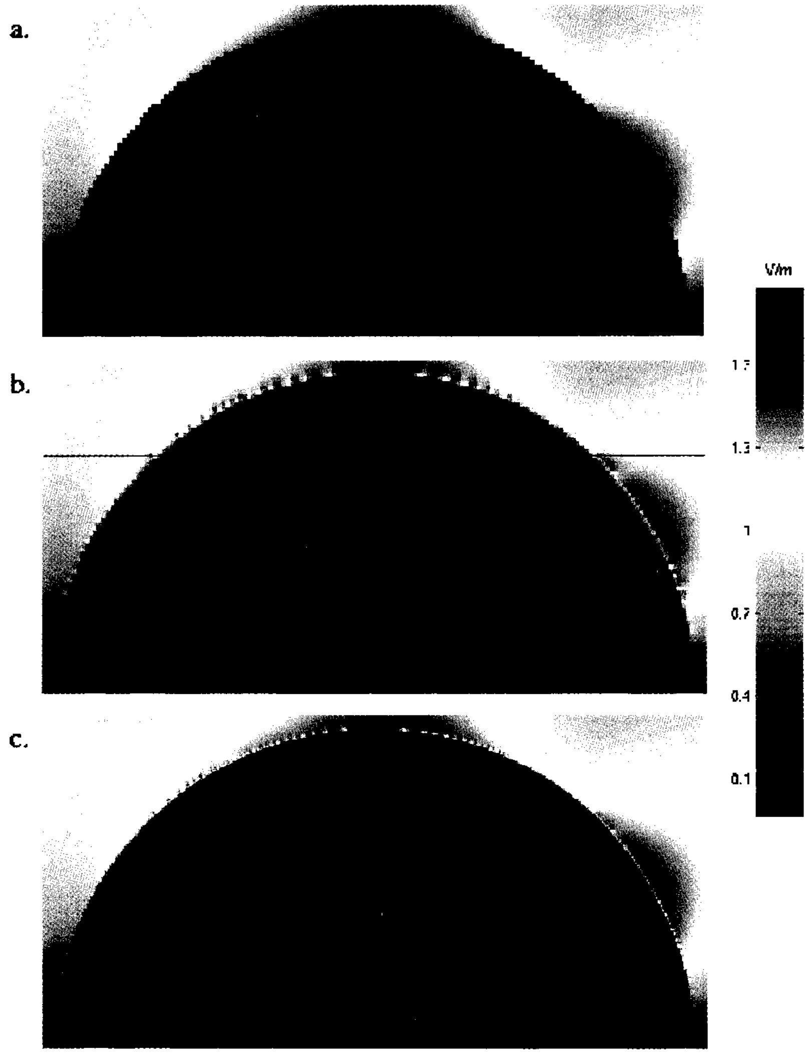

Figure 6-3 E-field in x-y-plane (H-plane) through the sphere: a. Mie solution on a grid 2mm, b. FDTD grid 2mm c. FDTD grid 1mm
The horizontal line in panel b. indicates the position of line plot in Figure 6.4

Differences between the FDTD and Mie solutions that occur outside the principal axes are illustrated in cross-sections of the sphere in Figure 6-3. Panels a, b, and c show the results from the Mie, 2mm FDTD, and 1mm FDTD codes respectively. The x-y plane (H-plane in terms of the illuminating wave) cross-sections are shown through the sphere center.

Overall the agreement between the panels a, b, and c of Figure 6-3 is excellent, but a number of differences can be seen along the boundary of the sphere. One type of difference between the Mie and FDTD fields is the transition between the inside and outside of the sphere. In the FDTD there is a layer of cells along the boundary that have values that lie between the field values inside and outside of the sphere (light-green color). This transition layer in Figure 6-3c. (1 mm grid) is obviously thinner than in Figure 6-3b. (2 mm grid).

The second type of a difference between the Mie and FDTD solution is the presence of elevated field values that occur in the FDTD solution and are located outside some of the ridges of discretized sphere. To pinpoint one such 'hot spot' the horizontal line in Figure 6-3b is drawn through the highest field value in the cross-section, which is located just outside the sphere on the left hand side of the panel. The elevated value is also present in the corresponding location in the 1 mm FDTD solution in Figure 6-3c. Figure 6-4 provides additional illustration, as it shows the field profile along the line indicated in Figure 6-3b. The red plot shows the Mie solution, the blue plot is for a 2 mm FDTD grid and the black plot for a 1 mm FDTD grid. It is evident, that the presence of elevated field is not eliminated by using a finer grid, both the location and the magnitude of the overshoot remain virtually unchanged in a 1 mm grid compared with a 2 mm grid. Apart from the errors on the surface and outside the surface the plot also confirms good agreement between the analytical solution and FDTD inside the sphere.

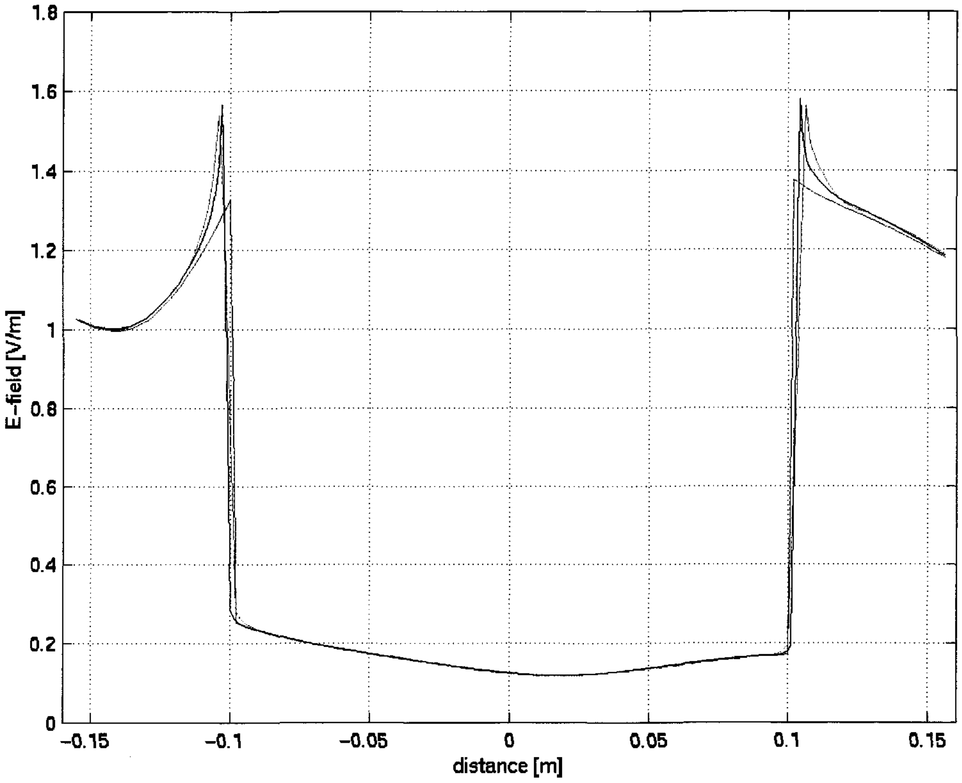

Figure 6-4 E-field along the line indicated in Figure 6-3b. Red plot is for Mie, 2mm FDTD is plotted in blue and 1mm FDTD in black. Due to staircase error, both 2mm and 1mm FDTD 'overshoot' by about 15% the values for a smooth sphere of Mie.

.

Statistical values, such as maximum, mean and standard deviation, computed for the whole volume and for the inside and outside of sphere are summarized in Table 6-2. The values in the column labeled 'whole' are for the whole volume and include the surface voxels of the sphere, which are excluded from the column 'in' with values for the inside and the column 'out' with values for the outside of the sphere. The agreement between the Mie and FDTD solutions is very good inside the sphere, and the standard deviation for the ‘in’ volume (2.2%) is smaller that the standard deviation along the principal axes (2.7%).

The statistical errors were not compiled separately for the surface layer of voxels excluded from the ‘in’ and ‘out’ volumes in the table because of a fundamental incompatibility between the Mie and FDTD solutions for that region. The discontinuity of the E-field at the surface, which is perfectly represented in the Mie solution as a step, is represented in the FDTD solution by a ramp function which spreads the field jump over the thickness of one or two surface cells. As a result the transitional values of FDTD solution differ drastically from the Mie values on either side of the jump.

The effect of isolated ‘hot spots’ in FDTD, as can be seen in Figure 6-4, is spread over several voxels into the ‘out’ volume and affects the statistics for that volume.

FDTD errors that are due to singularities associated with staircased surfaces can be alleviated by using sub-cell modeling and special field update schemes to represent dielectric surface not aligned with the grid [24]. However, this does not apply to voxel based body models, which inherently are characterized by staircased surfaces. Still, as evident from Figure 6-3, the elevated field values occur in empty space outside the dielectric and only to a lesser extent influence the power absorbed in the adjacent cells of the dielectric. Furthermore, the body surface fields are rarely of interest when the interactions of EM waves with the human body are considered. Since the fields for the smooth and staircased models converge inside the voxelized body, the singularity errors can be neglected, when the FDTD is used to determine the fields inside the body. The weight-averaged SAR algorithm (Chapter 5), when applied to a field with isolated voxels affected by the field singularity, further reduces its influence by spreading the elevated power in one voxel over the averaging volume which typically comprises many voxels.

Table 6-2 Statistics for Mie and FDTD fields: 'whole' indicates entire volume, 'in' inside of the sphere excluding the surface, 'out' outside the sphere excluding the surface

	Maximum V/m			Mean V/m			Standard deviation %		
	whole	in	out	whole	in	out	whole	in	out
Mie	1.73	0.27	1.72	0.512	0.048	0.46	--	--	--
FDTD 2mm	1.96	0.29	1.96	0.510	0.049	0.45	5.7	2.2	6.9
FDTD 1mm	2.02	0.30	1.99	0.511	0.049	0.45	8.6	1.4	7.9

6.3 Conclusions

Detailed evaluations and comparisons have been performed for human models in a uniform magnetic field of 60 Hz. Comparisons of data obtained independently by two laboratories confirm the reliability of methods and models used. All dosimetric values computed for each particular model agree within 2 % or less. Since *in situ* measurements cannot be performed in humans, and achievable accuracy of measurements in models and animals is not likely to be better than 10 – 15 %, the comparisons presented should provide confidence limits on computational dosimetry. The latter is an important, often critical tool for assessment of occupational and environmental exposures in complex environments.

The evaluation of model size, shape and resolution has confirmed previous observations, and further illuminate the reasons for large differences in voxel maximum electric fields for various human body models. The results reported also further emphasize that comparisons of data need to take into account all of the anatomical differences in the models.

The FDTD code has been evaluated by modeling the induced field inside a discretized sphere made of a typical body tissue. A field distribution inside the sphere obtained using an analytical formula based on the Mie series has been compared with the distributions obtained from FDTD computations in two resolutions: 2mm and 1mm. Excellent agreement (within 2%) has been obtained inside the sphere for both resolutions, as indicated by field statistics for the principal axes and the whole volume. Two types of errors have been identified on the surface of the sphere: one is a gradual transition of the fields from the inside to outside of the sphere, second is the presence of isolated 'hot spots' immediately outside the surface. Both these errors have been found insignificant in modeling the fields inside the body models, provided that sufficiently fine meshes are employed in the simulations.

7 Modeling of Selected Problems

7.1 Pacemaker interference by ELF magnetic fields

Implanted heart pacers and defibrillators have been shown to be sensitive to Electromagnetic Interference (EMI) by high electric fields at power line frequencies (50 or 60 Hz) [54], [55]. Recently performed numerical modeling of EMI in 60-Hz electric fields indicates that pacemakers with unipolar electrodes can be susceptible to EMI by fields of the magnitude of 6 kV/m [56]. Much stronger (of the order 4 to 5 times) fields are necessary to cause EMI with bipolar pacemakers. In the case of 50 or 60 Hz magnetic fields the close spacing of electrodes of bipolar devices practically eliminates the possibility of interference. However, for unipolar electrodes, the inductive loop of the pacer wire completed with the conductive path through tissues makes the EMI by magnetic fields a distinct possibility. In [57] the magnetic field levels of 21 mT (rms.) at 50 Hz and 17.5 mT at 60 Hz were estimated to induce a 1 mV peak-to-peak EMI signal. The estimation was based on a semicircular loop profile enclosing an area of 0.057 m^2. The manufacturers of pacemakers anticipate the EMI more conservatively at magnetic flux densities of 0.2 - 1 mT [58]. Fields this high and higher are possible in occupational exposures [59], [60].

In this study the SPFD method and the 3.6 mm model of the human body have been applied to compute the induced potential at the unipolar pacemaker input. Three orthogonal 60-Hz magnetic field orientations have been considered for two typical locations of the pacemaker generator, with both atrial and ventricular electrode placements. The results of these accurate computations have been compared with estimates obtained from a direct application of Faraday's law to the equivalent conductive loops formed by the pacer wire plus the shortest path connecting the electrodes.

7.1.1 Models and methods

The 3.6 mm UVic model with hands on the side is used for this set of computations. The 60 Hz conductivities assigned to tissues are identical to those used in comparison study of Section 5.1. In the model a metallic box representing a pacemaker pulse generator is embedded in the fat tissue in the left or right side of the chest, following typical clinical placements. Leads are routed through veins from the pacemaker generator to the atrium or ventricle of the heart. For comparison extravenous routing is also modeled. A total of 8 configurations are considered. They are designated as follows: generator placement – "left" or "right"; electrode – "A" for atrial and "V" for ventricular; wire path – "i.v." for intravenous and "e.v." for extraneous. The total lead resistance comprises the lead (typically 10-100 Ω) and amplifier input resistance. Two representative input resistances were used, namely 20 and 100 kΩ.

The computational method is SPFD, as described in Chapter 4, extended with an algorithm to represent an insulated thin wire implanted in the body.

7.1.2 Configurations and simplified computations

Figure 7-1(a) shows a frontal view of a typical placement of the pacemaker generator on the left side of the body and the ventricular lead path within the body. The heart and associated major blood vessels are also indicated. A pacer wire is shown threaded through the veins into the heart ventricle and ending on the contact point with the heart muscle. Figure 7-1(b) depicts an alternate location of the pacer generator on the right side of chest and appropriate wire threading into the ventricular pacing point.

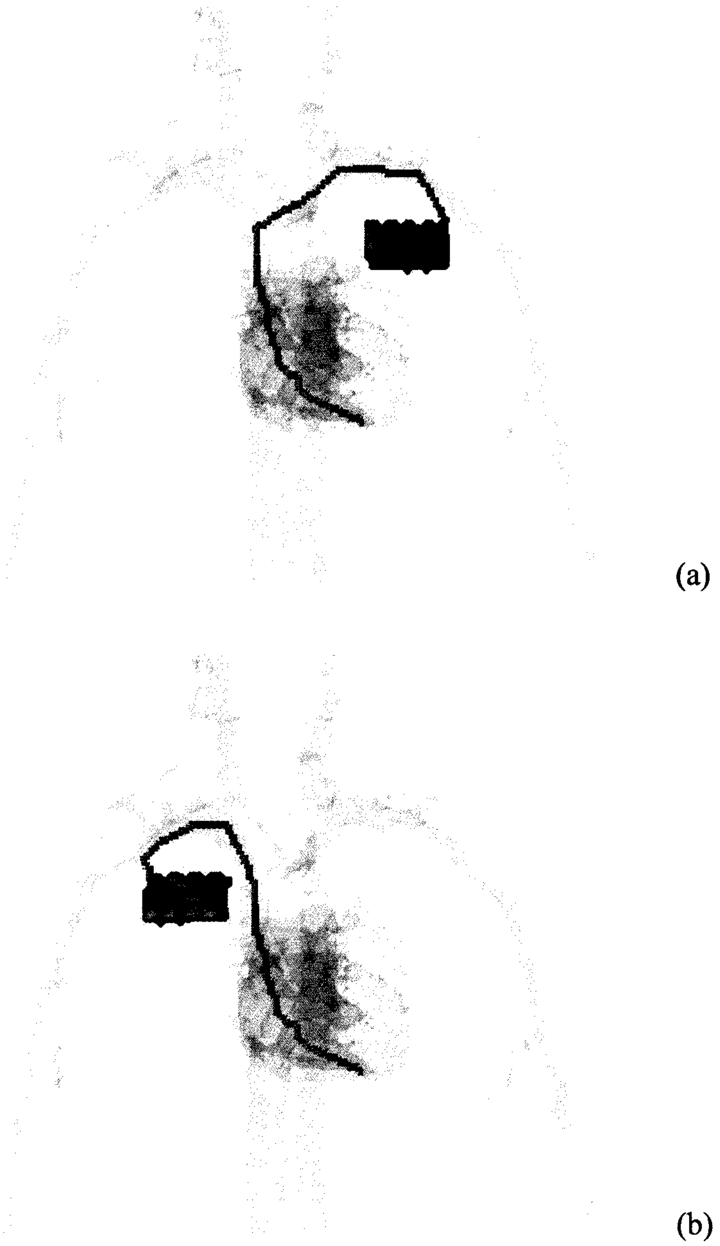

(a)

(b)

Figure 7-1 The heart pacer and the pacer wire: (a) left side location, (b) right side location

In order to obtain approximate values of the induced EMI potentials a method is applied similar to that used earlier [57]. The loops formed by the leads are projected onto the x-, y- and z-planes and are completed by straight line return paths. The resulting traces are shown in Figure 7-2. Areas enclosed by the traces are used to compute the EMF due to magnetic field directed along x–, y– and z–axix. Traces in parts (a) and (b) of Figure 7-2 are for the generator placed on the left and right sides of the torso, respectively.

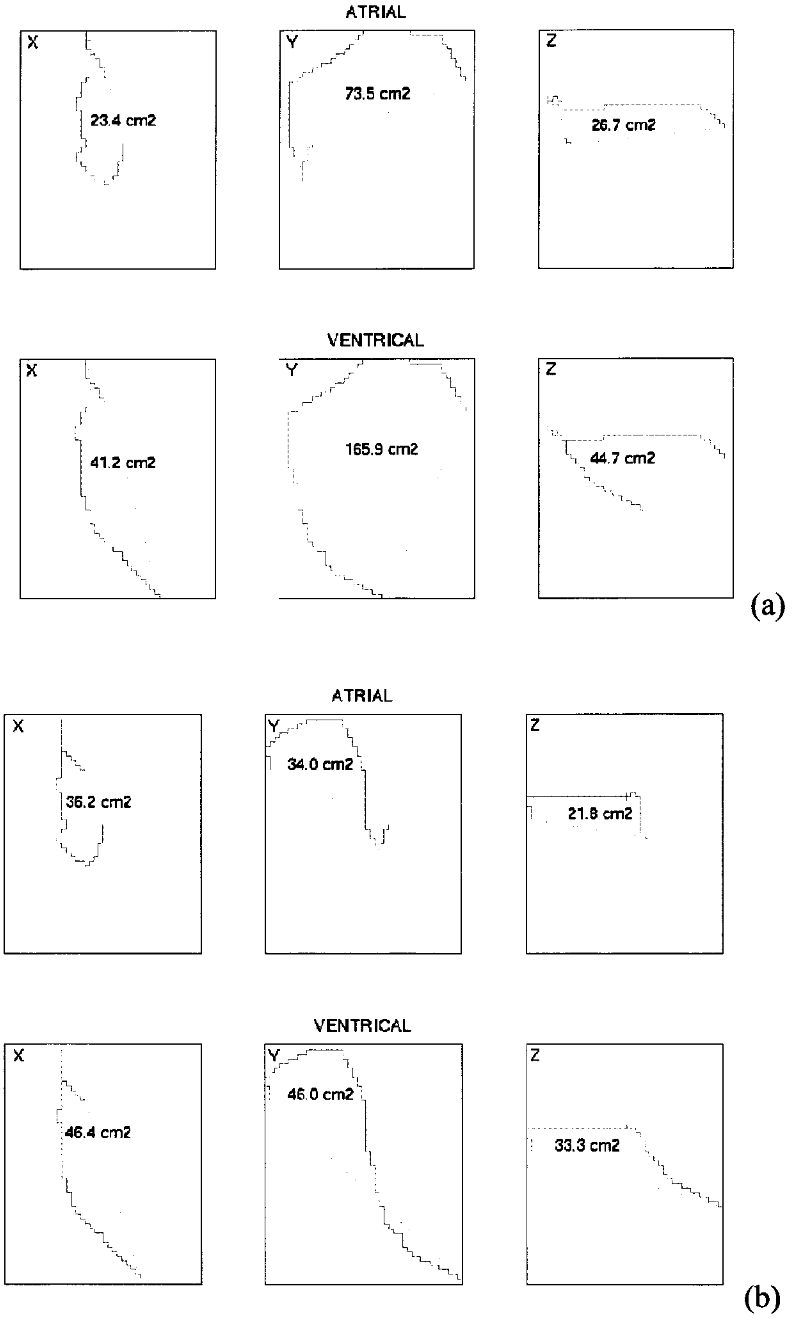

Figure 7-2 Pacer wire projections on principal planes x, y and z with dotted straight lines completing inductive loops. (a) left side pacer location, (b) right side pacer location

Estimated potentials between the pacer case and the contact point in the heart are given in Table 7-1. Three orientations of the magnetic flux density vector are considered, namely left-to-right (B_x), back-to-front (B_y) and head-to-foot (B_z). The potential is computed from the electromotive force (EMF) produced by the magnetic flux through the surface area projections indicated in Figure 7-2.

Table 7-1 Estimated potentials from Faraday's law, for 60 Hz, 0.1 mT source fields.

Pacer	Electrode	Lead length [cm]	EMI potential [mV]		
			Bx	By	Bz
Left	Atr	42.84	0.068	0.213	0.078
	Ven	53.28	0.119	0.478	0.129
Right	Atr	36.00	0.060	0.100	0.064
	Ven	46.44	0.093	0.118	0.086

Assuming the same effective resistivity for the leads and tissue between the electrodes the potential is computed from

$$V = emf\frac{L_w}{L_w + L_s} \tag{7.1}$$

where L_w and L_s are the lead and straight return path lengths respectively. If the return current paths through the body are modeled by an equivalent resistance R_s, Eq (5.1) can be replaced by the more accurate condition

$$V' = emf'\frac{R_w}{R_w + R_s} \tag{7.2}$$

Thus, computing the induced voltages accurately using the Faraday approximation requires knowledge of the equivalent body resistance and projected loop area.

7.1.3 Numerical computations

The 8 pacemaker and wire placements and 2 pacer input resistance values combine with the three magnetic field orientations to create 48 configurations, each requiring a separate execution of the SPFD program. All source levels are 0.1 mT at 60 Hz. Table 7-2 summarizes the induced EMI voltages as obtained from the 48 numerical modeling configurations. The indicated lead lengths L_w are in cm and the resistances R_w in kΩ.

Table 7-2 Induced voltages (mV) from the numerical modeling

R_w				B_x	B_y	B_z	L_w
Left	20	A	e.v.	0.076	0.554	0.163	35.64
			i.v.	0.019	0.554	0.062	42.84
		V	e.v.	0.326	0.528	0.056	48.6
			i.v.	0.214	0.528	0.042	54.36
	100	A	e.v.	0.078	0.569	0.168	35.64
			i.v.	0.019	0.569	0.064	42.84
		V	e.v.	0.335	0.542	0.057	48.6
			i.v.	0.22	0.542	0.043	54.36
Right	20	A	e.v.	0.058	0.28	0.111	30.24
			i.v.	0.014	0.28	0.029	36.0
		V	e.v.	0.308	0.32	0.233	43.2
			i.v.	0.225	0.32	0.15	47.52
	100	A	e.v.	0.059	0.287	0.114	30.24
			i.v.	0.014	0.287	0.03	36.0
		V	e.v.	0.316	0.329	0.239	43.2
			i.v.	0.231	0.329	0.154	47.52

The identical voltages for B_y excitation for the e.v. and i.v. lead reflect the fact that in the modeling a shift in the y-direction was used to place the lead outside the veins. Hence, two cases have identical loop area projections onto the y-plane. This translation also increases the projected area in the z-plane for the extravenous routing. This contributes to the variations between the e.v. and i.v. values in Table 7-2.

The results are compared in Table 7-3, which presents ratios of the induced voltages from the full numerical modeling (Table 7-2) to the simple estimates (Table 7-1), for the intravenous wire routing. The ratios range from 0.25 to 2.87.

Table 7-3 Ratios of the induced intravenous lead voltages from the full numerical modeling to the simple estimates

	R_w		B_x	B_y	B_z
Left	20	A	0.29	2.62	0.8
		V	1.79	1.12	0.33
	100	A	0.29	2.69	0.82
		V	1.84	1.15	0.33
Right	20	A	0.25	2.8	0.46
		V	2.4	2.69	1.74
	100	A	0.25	2.87	0.47
		V	2.46	2.76	1.79

7.1.4 Pacemaker Interference

Comparing simple assessments of the possibility for pacemaker EMI by 60 Hz magnetic fields with accurate computations, it can be seen that neglecting the complicated current path through body tissues leads to large errors in predicted EMI. Based on data in Table 7-2 and typical sensitivity settings of 0.25 – 1.6 mV for atrial pacemakers, and 0.75 – 4.0 mV for ventricular pacemakers [58], [61], the following levels of magnetic flux density may cause EMI. For the atrial electrode, the highest voltage is 0.569 mV at $B_y = 0.1$ mT. Thus, the limit of 0.25 mV is exceeded at 44 mT. For the ventricular electrode, the highest voltage is 0.542 mV. The limit of 0.75 mV is exceeded at 138 mT. On the other hand, based on the estimates from Figure 7-2 and Table 7-1, for the atrial electrode the threshold for EMI is 90 mT, and for the ventricular electrode the threshold is 120 mT.

7.2 Cellular Telephone Modeling

Among numerous problems related to interaction of wireless communication devices with the human body, EMI with the body attached or implanted devices is one of the most critical, apart from the determination of the SAR. In this chapter attention is directed towards the interference of a cellular telephone transmitter with a hearing aid device.

Cellular telephones such as the global system for mobile communication (GSM) and personal communication services (PCS) are well known to cause electromagnetic interference (EMI) with hearing aids. The main source of the EMI is the amplitude modulation in the acoustic range due to the time-division multiple access (TDMA) and to a lesser extent the code-division multiple access (CDMA). In the case of the TDMA, a frequency of 217 Hz and its harmonics are present in the European systems, and 50 Hz and its harmonics in the North American systems. For the CDMA transmitter at full output power there is no significant amplitude modulation, and at variable power rates the EMI spectrum resembles that of white noise [71]. The magnitude of the acoustic interference depends on several parameters of the telephone and the hearing aid [71], [74], [75]. For a given type of the telephone, the level of EMI induced sound pressure levels (SPL) vary by more than 40 dB depending on design of the hearing aid [71]. Similar levels of interference have been observed for hearing aids used in both microphone and telephone coil modes of operation. In the coil mode the hearing aid responds only to magnetic fields produced by the telephone [71]. More often, though, hearing aids are set to the microphone operation. Moreover, similar levels of interference in both modes of operation implicate either both electric and magnetic components of the telephone field or only the magnetic component. Thus, for a given hearing aid and telephone, the EMI depends on the fields in the location of the hearing aid.

Earlier numerical modeling has shown that the electromagnetic fields from a cellular telephone are very different in the ear canal compared to those in free space [76]. These early results refer to a generic telephone consisting of a monopole on a metallic box, and vertical placement of the handset next to the head. Both electric and magnetic fields vary much more rapidly with the distance inside the ear canal than in free space. Different spatial components of the fields are produced in and around the ear from those around the telephone in free space.

In reality, radiating systems of cellular telephones are more complex than a simple monopole on box which is directly reflected in the distribution of near fields around the antenna. The most common antenna system among commercial telephones consists of two coupled helices. A short, normal mode helical antenna is mounted in the corner of the telephone box, usually hidden inside the characteristic stubby plastic enclosure. This antenna is powered at its base by the RF amplifier. Second helix is embedded in the extendable plastic whip. There are two modes of operation of this antenna. When the whip is extended its helix is coupled with the field of the powered helix and it radiates and receives as a resonant half-wavelength dipole, thus enhancing the radiation performance of the short helix. With the whip retracted into the telephone, its metallic parts are shielded from the powered helix, which in this mode radiates and receives alone.

An example of a telephone utilizing the dual helical antenna is the Motorola TAC 7500 (Figure 7-3). This telephone has been the subject of the joined project of Motorola Laboratories, Florida, the US Food and Drug Administration Laboratories and University of Victoria. The aim of the project has been to evaluate EMI with a hearing aid device. Motorola labs performed a detailed mapping of the near fields of the telephone. Motorola also supplied information about the dimensions and the internal construction of the telephone device. Food and Drug Administration lab performed acoustic tests of the EMI of the telephone with a hearing aid device. Computer modeling of the fields and data analysis has been performed at the University of Victoria.

Performance evaluation of a complex antenna in its operating environment (two helices, handset and human tissue) can be done experimentally or numerically [62], [63], [64], [65], [66]. The numerical modeling approach or a combination of experiment and numerical modeling, offer many advantages compared with a purely experimental approach, which has been often used till now. However, modeling poses many challenges and, in order to be considered reliable, has to be verified.

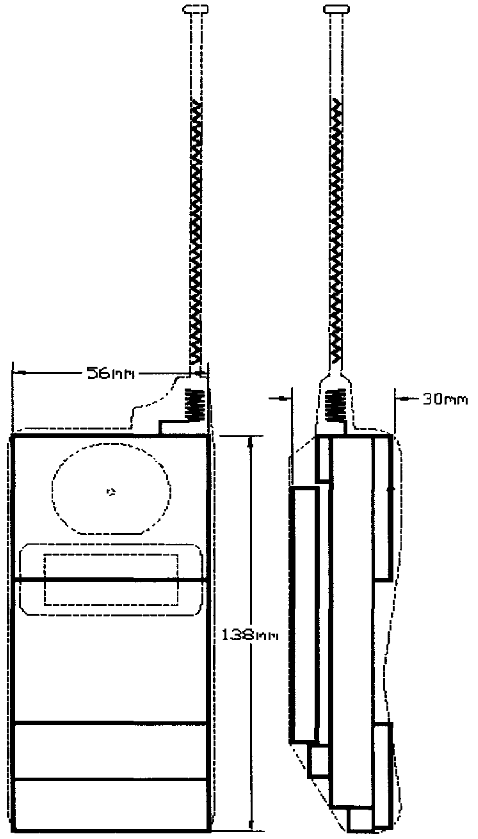

Figure 7-3 GSM telephone, model Motorola TAC 7200

In this work, the modeling of an antenna consisting of two helices is verified by comparison with measurements made in the manufacturer's (Motorola) laboratory, a limited measurement in our laboratory, and by use of two computer codes. This multifaceted verification provides confidence in the results of computations of data that cannot be obtained experimentally.

Thus, having verified our FDTD modeling of the helix antenna, this method has been used to evaluate performance of the handset in the vicinity of the user's head. Such an evaluation is not possible experimentally for realistic models, only for highly simplified models of the human head. Our investigations include the input impedance, the far-field radiation pattern, power deposited in the human tissue and detailed field mapping of both electric and magnetic components inside the ear canal where the hearing aid device is located. The influences of the ear shape and various positions of the handset with respect to the user's head have been evaluated.

7.3 FDTD modeling of a helical antenna on a handset

The FDTD method is used for the analysis because of its flexibility and efficiency in solving complex heterogeneous geometry problems. The Yee-cell, rectangular grid and the total-field formulation are used. Two different FDTD codes are used, our own code and the LC code provided by the SGI [67]. The reason for two codes is to ensure reliable modeling of the helical antenna and computational efficiency. Our own code has graded meshes, thus facilitating the reduction of computer resources for larger problems that include the human head in the FDTD space. Additionally, this code allows us to properly allocate the electrical properties of tissues in the head model.

The powered helix in Figure 7-3 consists of 7 turns having an external diameter of 5.35 mm and the axial length of 11 mm. An L-shaped feedline 12 mm long and 5 mm wide connects the helix to the coaxial output of the amplifier. The helix and its feedline are fabricated from a length of silver plated wire 0.5 mm in diameter.

This structure is modeled staircased along the edges of the Yee cells as shown in Figure 7-4. The actual helix with the inside diameter of 4.85 mm is approximated in a 1 mm FDTD mesh as a square helix measuring 4 grid cells per side and thus having comparable cross-section of turns. The discretization has been accomplished by choosing a continuous path of cell edges selected as the nearest neighbors along the length of the real helix. Thus, the discretized helix has the same number of turns, the same axial length and approximately the same cross-sectional area. This structure is further refined in the trial FDTD runs. By varying the cell size, the resonance of the helix has been tuned to 900 MHz to match the resonance of the real helix measured in the lab with the network analyzer. This condition has been obtained with the grid size 0.95 mm.

Similarly discretized is the passive helix in the retractable whip. The real helix consists of 28 turns of 0.3 mm wire for the axial length of the helix of 92 mm and has the resonance frequency of 980 MHz.

The discretized passive helix has 2 by 2 cell cross-section. In separate FDTD runs it has been determined that a resonance of the passive whip can be obtained at 980 MHz using 2 cell pitch and axial length of 94 cells. Thus, the modeled whip has a larger number of turns that the real helix but approximates well the physical size and resonance frequency. The discrepancy in the number of turns apparently accounts for the helix in the real whip being embedded in plastic with permittivity higher than that of free space. This leads to the lower resonance frequency than without the plastic coating.

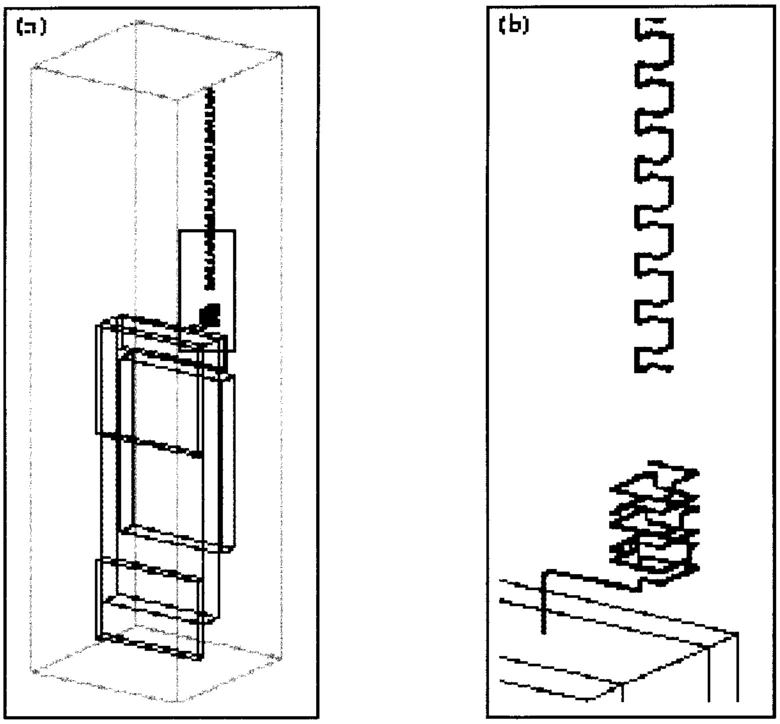

Figure 7-4 Major metallic parts of the handset as represented in FDTD domain (a), detailed view of staircase discretization of helices (b)

Such separately validated antenna parts are modeled on a handset, whose dimensions of metallic parts are based on the blueprints supplied by Motorola and are accurate. The handset box is covered with a dielectric material. Several test trials that have been performed, indicate that such features as curvature of plastic parts and small detail of the telephone do not change the electromagnetic fields around by more than 1 %. Thus the telephone model consists of metal parts, shown in Figure 7-4, covered with 1 mm dielectric of $\varepsilon'_r = 2.1$. A perfectly matched layer (PML) terminates the computational space, which, in addition to the telephone structures, encompasses free space in front of the handset to record the fields, electric and magnetic at distances 10 to 40 mm from the handset face (for comparison with measurement results). This set of computations, as shown in Section 7.4 fully validates modeling of this particular handset in FDTD.

A larger FDTD domain is used to include the head model as shown in Figure 7-5

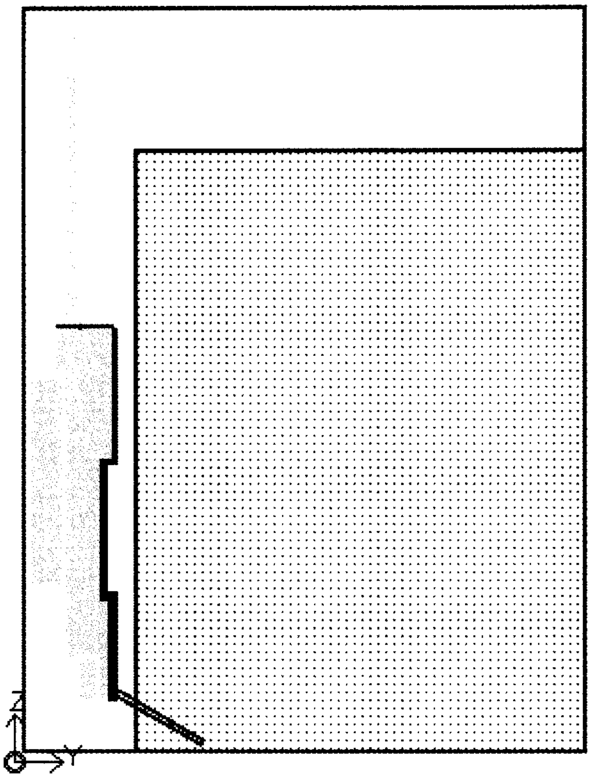

Figure 7-5 FDTD model combining handheld telephone and head model (gray shaded area).

The grid resolution varies from 0.95 mm to 4 mm. Graded meshes with 1:1.2 steps are utilized, where a fine grid is used to model the antenna, its vicinity, and the ear region of the head. A coarser resolution is used further away from the area of interest. A frequency shifted Gaussian pulse excites the antenna. The total output power from the antenna in free space is computed from the radiated power, and for the telephone next to the head as a sum of the total radiated and total absorbed power in the tissue [63].

In the FDTD modeling, the handset is aligned with the coordinate system as shown in

Figure 7-5, while the head model is rotated into various positions. Appropriate measures are taken to maintain the head anatomy after the rotation. Typical handset placement closely simulates that used in the acoustic measurements and is shown in Figure 7-6.

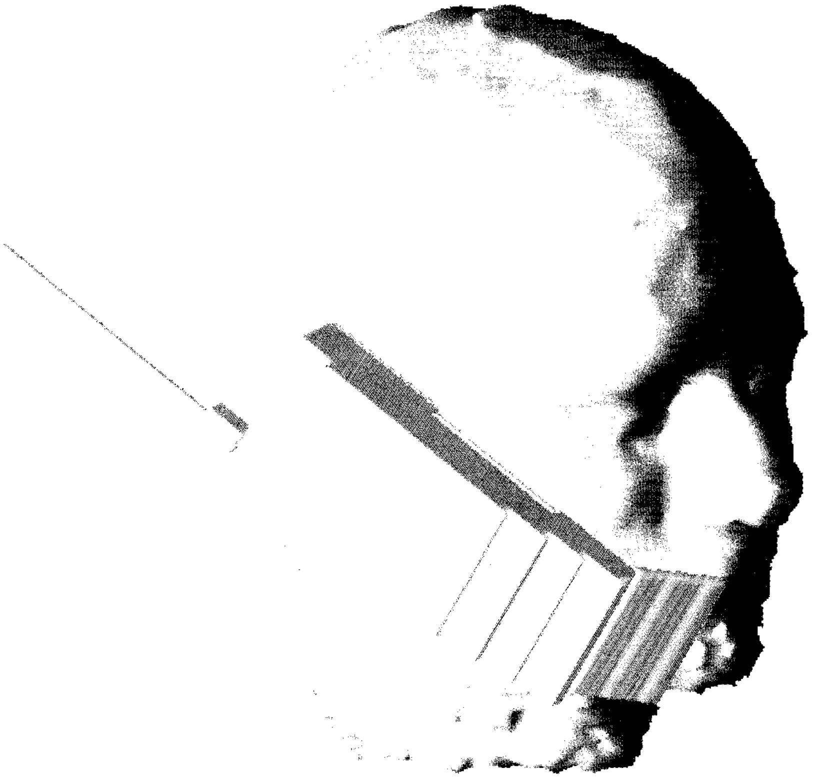

Figure 7-6 Telephone and head as modeled in FDTD. 3D rendering of metallic and plastic parts of the telephone and the head. Picture rotated to show the head upright.

Because of the differences in ear shapes and telephone placement, several variants of the placement are investigated. Also two shapes of external ear (pinna) are considered. A special FDTD algorithm is available in the UVic FDTD code to handle dielectric objects with shapes and/or voxels that do not coincide with the FDTD mesh. This algorithm has increased the accuracy of computations, particularly when the head model was not aligned with the coordinate system. In the cases where the metal surfaces did not coincide with the mesh, another algorithm was used that allows for accurate treatment of fields near these surfaces [68].

7.4 Comparison of measurements with computations

7.4.1 Measurement Method

Electric and magnetic fields have been measured at the telephone manufacture's laboratory using an automatic scanning system and miniature free-space E- and H-field probes. The probes consist of three small antennas and give a total magnitude of the field measured. External diameters are 6.9 mm and 5.9 mm for the electric and magnetic field probes, respectively. The scans are performed in four planes spaced 10 mm to 40 mm from the center of the telephone earphone. The frequency is 902.4 MHz (center of the transmit band) and the power output is set to the test mode. The manufacturer's specifications for the probes indicate ±12 % measurement uncertainty. However, it has been assessed that spurious reflections in the laboratory environment produced greater errors, estimated at 20 %.

7.4.2 Results – near-field comparison

Magnitudes of electric and magnetic fields are compared in free space near to the antenna, where the fields are spatially very non-uniform. With the measurements and computations performed in different laboratories, we thus presume that the computations are accurate within the limits of uncertainties associated with the methods used. Figure 7-7 and Figure 7-8 present detailed maps of the measured and computed fields in a plane parallel to the handset, 1 cm away from the earpiece, for the retracted, and extended antenna. The same output power of the telephone (test mode) is used in all measurements and computations. Good agreements are apparent for both the electric and magnetic fields. It should be noted that the measured fields have not been scanned in the areas on the upper-left side corner of the planes, and as a result, there is a blank rectangle in panels (a) and (c) of Figs 7-7 and 7-8. Note also that close spacing of contour lines around the blank rectangle is an artifact of field plotting and not a steep gradient of the measured fields.

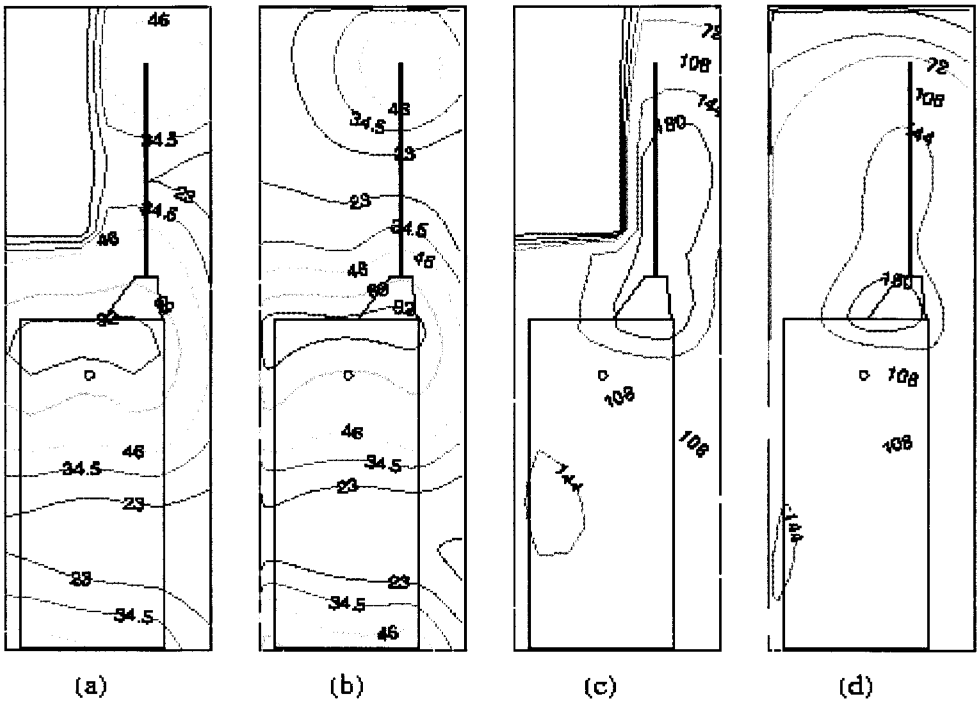

(a) (b) (c) (d)

Figure 7-7 Electric fields in V/m (a) measured, (b) computed, and magnetic fields in mA/m, (c) measured, and (d) computed. All values are in free space 1 cm from the telephone. Antenna extended.

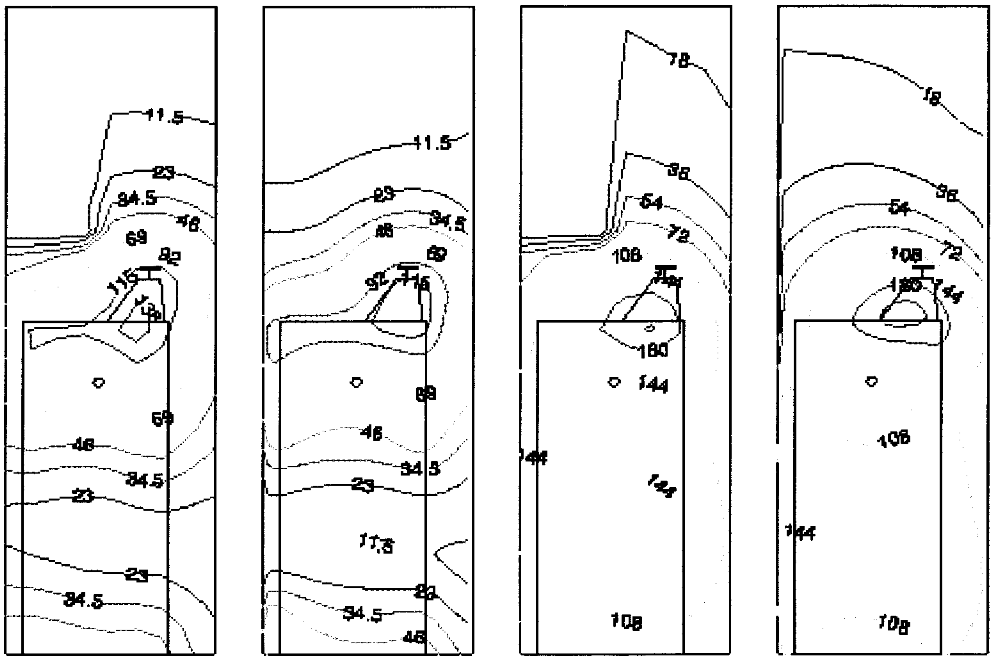

(a) (b) (c) (d)

Figure 7-8 Electric fields in V/m (a) measured, (b) computed and magnetic fields in mA/m, (c) measured, and (d) computed. All values are in free space 1 cm from the telephone. Antenna retracted.

Tables 7-4 and 7-5 give more quantitative global comparisons for four planes where measured data are available. These data refer to a test area of 9 by 16 cm, sampled in a grid of 10-mm (total of 170 points). The test area is rectangular and extends up to the region where the measurements are not taken (Figs. 7-7 and 7-8). Three measures of error are used. One of the measures is a relative difference (Δ_R) between mean measured and computed fields within the test area. The second measure is the mean value of absolute error (Δ_M) defined as:

$$\Delta_M = mean\left(\frac{2\left|F_{mi} - F_{ci}\right|}{\left|F_{mi} + F_{ci}\right|}\right) \tag{7.3}$$

where F_{mi} and F_{ci} are measured and computed fields, respectively in each point within the test area. The final measure is the standard deviation:

$$\Delta_{STD} = \left[mean \left(\frac{2\left| F_{mi}^2 - F_{ci}^2 \right|}{\left| F_{mi}^2 + F_{ci}^2 \right|} \right) \right]^{1/2} \tag{7.4}$$

Examination of data in Tables 1 and 2 indicates a reasonably close agreement between the computed and measured electric and magnetic fields. This agreement for 1-cm plane separation is within the surface area where the hearing aid is placed in the acoustic measurements. All the mean fields (Δ_R) are remarkably close to each other. Differences of up to 16 % are in mean values of relative absolute differences (Δ_M) in each point. Even larger Δ_{STD} can be noted, as this measure emphasizes differences in single points. The differences of the magnitude observed are entirely expected in view of the errors associated with measurements alone.

Uncertainties associated with computations are more difficult to estimate. With the size of the grid used and closeness of results obtained with two FDTD codes, the method is accurate at least within 2% (or better). However, there are errors associated with modeling details of the antenna and the handset. These errors are quite difficult to assess quantitatively. Nevertheless, the good agreement between the measurements attests to reasonable modeling of the device.

Our tests of telephone representation have indicated a lack of sensitivity to small details of the dielectric parts of the handset. A relative insensitivity to modeling of fine details of the handset has been also reported in [65] for power deposition in the head. On the other hand, it needs to be stressed that correct representation of the antenna is essential.

Data in Tables 7-4 and 7-5 also indicate that values of Δ_M are generally smaller in planes further removed from the telephone. With the dimensions of the measurement probes, particularly for the electric field, there is a possibility of coupling of the sensor antenna with the handset.

Table 7-4 Comparison of the measured and computed fields in free space close to the telephone; antenna extended. All differences listed are in percent.

Field	E			H		
Distance	Δ_R	Δ_M	Δ_{STD}	Δ_R	Δ_M	Δ_{STD}
1 cm	5.3	13.5	28	0.1	11.4	7.2
2 cm	1.7	8.6	15	0.3	9.2	23
3 cm	2.5	6.4	11	0.4	7.6	27
4 cm	2.1	6.8	13	0.3	6.9	27

Table 7-5 Comparison of the measured and computed fields in free space close to the telephone; antenna retracted. All differences listed are in percent.

Field	E			H		
Distance	Δ_R	Δ_M	Δ_{STD}	Δ_R	Δ_M	Δ_{STD}
1 cm	0.7	16	21	2.8	12	6.5
2 cm	1.9	11	24	0.8	9.7	21
3 cm	3.2	9.1	28	2.0	7.8	25
4 cm	3.7	10	33	2.5	7.8	26

7.5 Antenna characterization

7.5.1 Resonant Frequency and Input Impedance

Table 7-6 gives resonant frequency and input impedance obtained for an extended antenna in free space and in 3 and 4 positions close to two models of the ear. The resonant frequency and impedance in free space are in good agreement also with approximate measurements. Data in Table 7-6 are given only for the extended antenna, as this mode of operation is most often used in practice.

Table 7-6 Resonant frequency and impedance of the antenna on the handset in the vicinity of the user's head.

Test Conditions		Resonant Frequency [MHz]	Impedance
Free-Space		902	33 Ω
Normal Ear	*P1	890	40 Ω
	P2	891	38 Ω
	P3	898	35 Ω
Flat Ear	P1	892	37 Ω
	P2	897	38 Ω
	P3	900	38 Ω
	P4	900	39 Ω

* P – indicates various positions with respect to the ear.

Various placements of the telephone with respect to the user's head in a tilted position followed the configuration shown in Figure 7-3, but varied in the distance. It has been found that the resonant frequency of this antenna changes little in the presence of the human head. Furthermore, the impedance of the antenna in free space with the second helix retracted (33 Ω) is relatively close to the impedance with the extended helix (35 – 40 Ω) when the handset is placed next to the user's ear. The retracted antenna in free-space, and extended next to the head are typical use positions. This commercial antenna, while designed most likely experimentally (by "cut and try") actually performs rather well in terms of relatively small mismatch caused by the presence of the user's head.

7.5.2 Radiation Patterns

Antenna radiation patterns in free space and in the presence of human head are illustrated in Figure 7-9 and Figure 7-10, showing 3D plots of radiated power. The plots are normalized for maximum at 0 dB. In free-space, the pattern resembles that of a dipole with uneven arms. The second arm of the antenna is due to the current on the handset box and since the box is longer than the upper helix, the radiation pattern maximum is downward oriented. Similar behavior has been observed also for monopole antennas on handsets [63]. The proximity of a head (Figure 7-10) clearly affects the radiation pattern.

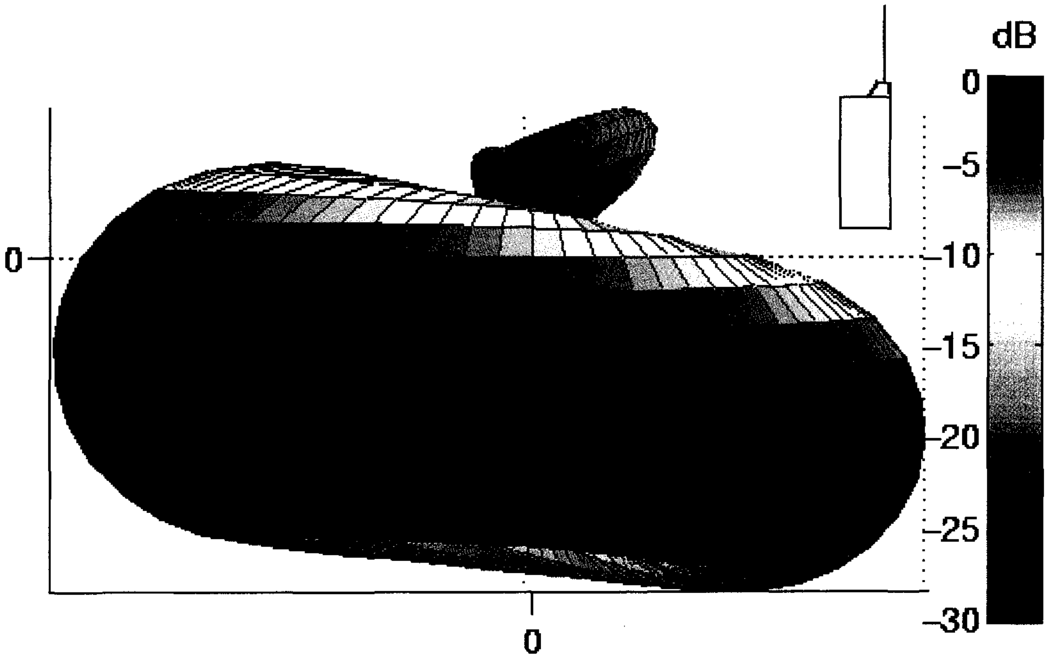

Figure 7-9 Stereoscopic radiation pattern in free-space.

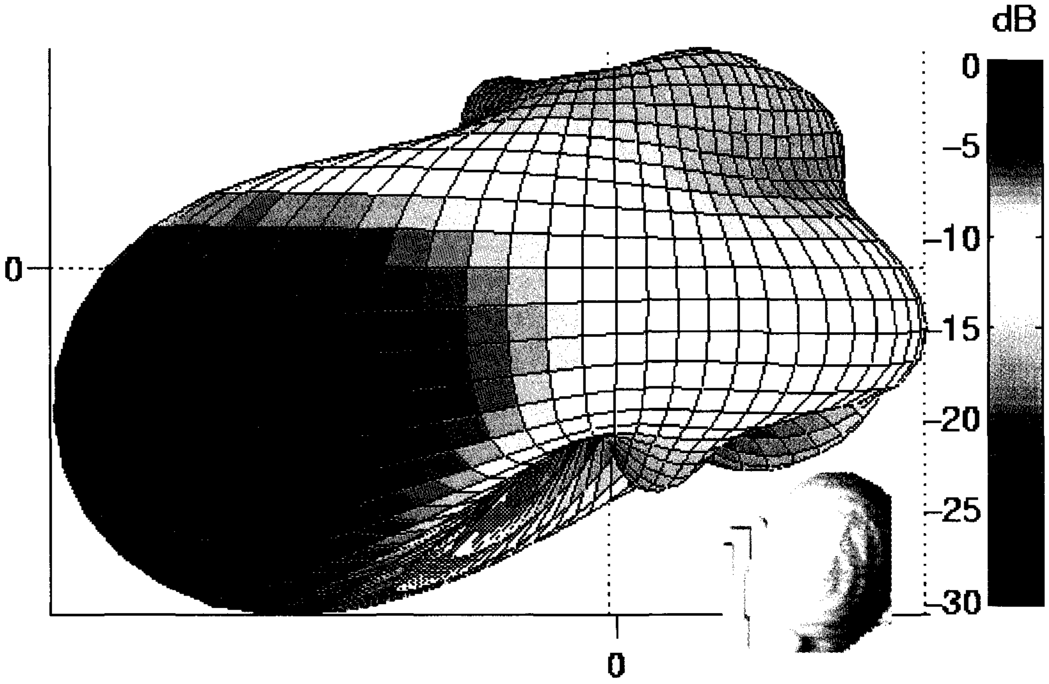

Figure 7-10 Radiated power for the handset antenna next to the user's head. Head and telephone orientation relative to pattern illustrated by inset.

7.6 SAR evaluation

The SAR values in 1 g or 10 g of tissue are required by regulations to be below 1.6 W/kg in North America [71], and 2 W/kg in Europe [72], respectively. Both standards prescribe only one position for testing. Using method described in Chapter 4, the 1g and 10 g average SARs have been computed for the entire head volume. A crossection through the head model showing the 1g average SAR is presented in Figure 7-11.

Figure 7-11 1g average SAR in the head crossection

Average SAR values for 1g and 10 g were obtained for the head volume by a search for the maxima. Table 7-7 gives relative values of SARs for the two models of the ear and for various distances between the handset and the head, normalized to the highest SAR obtained in all configurations. Separation 0 mm corresponds to the handset touching the head in a position specified in regulations. The 10-g SAR values are smaller than 1 g

SAR values, as expected. Also, SAR decreases with separation between the handset and the head. What is rather surprising, though, is a larger SAR for the "normal" ear than the flattened ear.

Table 7-7 Relative SAR values normalized to the highest.

		Relative SAR	
Ear Model	Separation	1 g	10 g
Normal	0 mm	1	0.35
	0 mm*	0.78	0.31
	8 mm	0.40	0.20
Flattened	0 mm	0.52	0.31
	4 mm	0.40	0.27
	6 mm	0.34	0.26
	8 mm	0.32	0.26

* P – different position

7.7 EMI of a GSM cellular phone with hearing aid device

7.7.1 Acoustic Measurements

Hearing aid EMI is evaluated by measurements of radio frequency (RF) induced sound pressure level (SPL). Tygon tubing is used to connect the hearing aid to the SPL meter without disturbing the RF field, as described in [71]. Measurements are performed for the hearing aid in free-space and in the ear canal. In both cases, the hearing aid is aligned with the center of the telephone earphone. The distance between the hearing aid and the phone is 10 mm for both test positions (free space and telephone placed against the ear).

Data has been obtained for three persons. Two separate measurement sets of 10 samples are taken for each person.

When exposed to pulse-modulated fields from the GSM phone, an audio tone is induced in the hearing aid acoustic output with a fundamental frequency of 217 Hz. The single frequency of 217 Hz in the SPL signal has been measured with a Bruel and Kjaer Type 2144 Frequency Analyzer to determine the sound pressure level (SPL) in dBA emitted by the hearing aid. The case of free space exposure of the hearing aid is used as a reference level.

To obtain insight into the relationship between the RF power exposure from a cellular phone and the resulting acoustic SPL produced by the hearing aid, an additional experiment has been performed. An RF signal generator with GSM modulation and output power adjustable between –40 dBm and –5 dBm feeds a half-wave dipole antenna through a coaxial cable. The hearing aid under test is placed at the center of the dipole (the region where the maximum magnetic field exists). RF power into the dipole has been adjusted to produce SPL levels that exist over the entire range of experimental values obtained with the GSM test telephone. These values included those of the hearing aid in the ear of 3 test subjects.

7.7.2 Fields in the ear canal

Figure 7-12 and Figure 7-13 show the magnitude of the electric and magnetic field for two models of the ear (pinna). These magnitudes are shown close to the center of the ear canal. It needs to be noted that the ear canal is not aligned with any axis of the coordinate system, and does not proceed along a straight line. The distance shown on the abscissa is measured from an entrance into the auditory canal. The center of the entrance in the auditory canal is at the reference point. The free space curves correspond to the magnitude of the fields without the head but with the cellular telephone in the same position. For each ear-model in addition to the standard placement of the telephone as in Figure 7-6 (and acoustic tests) results for two other placements are illustrated.

One general observation is that the magnitudes of the electric fields are attenuated in the ear canal, while the magnitudes of the magnetic fields are enhanced. The result for the magnetic field may be surprising, however, it is in agreement with the previously reported results for a monopole antenna on a handset modeled at UVic lab with the same code and head model [76]. This enhancement is a result of scattering of the near-field within the heterogeneous model of the head. As a result, components of the field appear that are not present in the free space.

Overall, each field component may vary quite rapidly inside the ear canal, as observed in [76], as well as in this work. The magnitude of the total field usually changes more smoothly. A few rapid changes of the electric field in Figs. 6-10 and 6-11 are most likely due either to the test point being close to the canal wall, or a rapid change in magnitude of one field component.

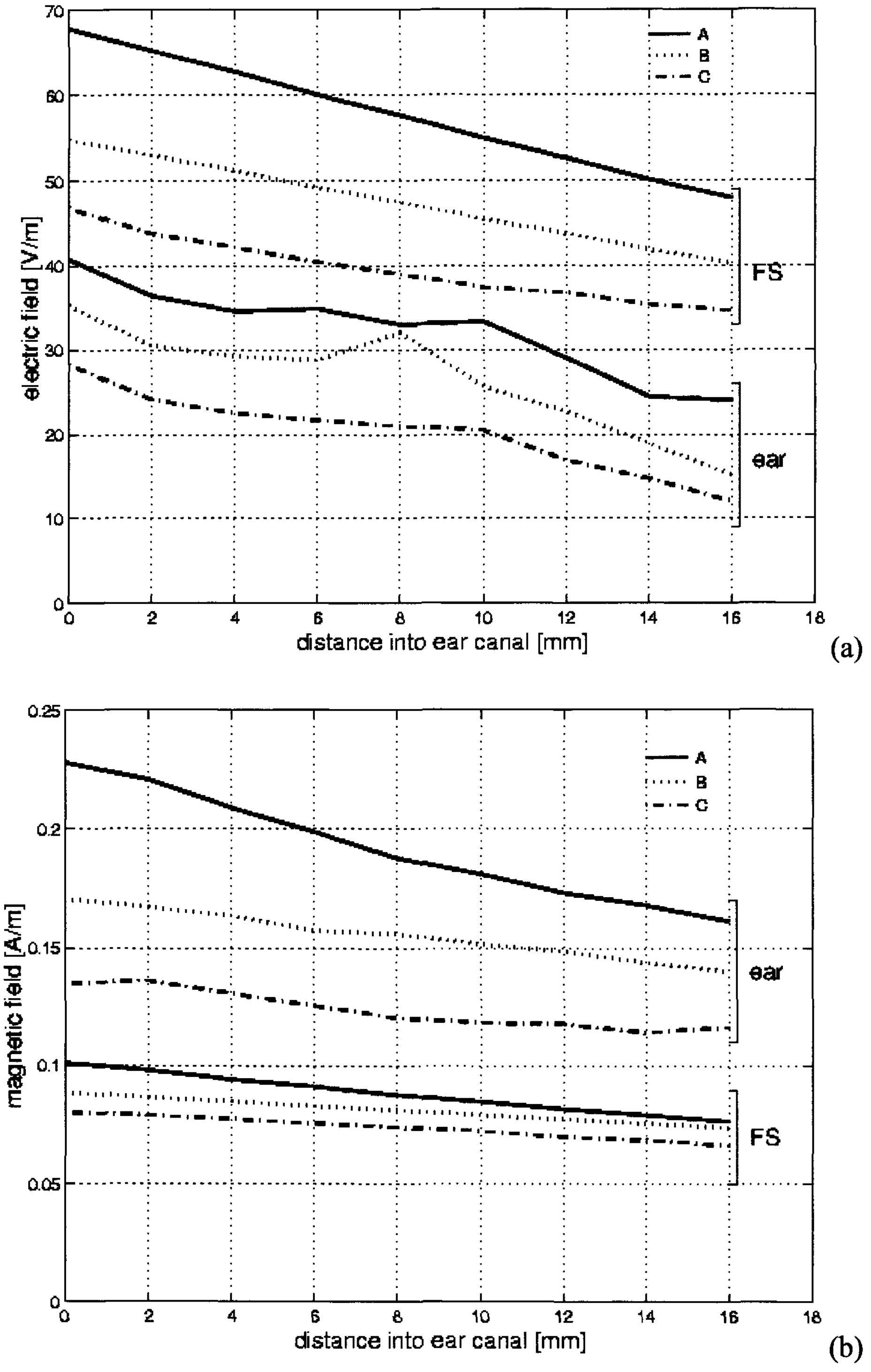

Figure 7-12 The electric field (a) and magnetic field (b) magnitude in free space (FS) and the ear canal (E) for the compressed ear-model and various positions of the telephone. Antenna extended. A- the center of earphone in the reference point (Fig. 6-1). B - the earphone 4 mm away from the ear canal, and aligned with the reference point. C - the earphone 12 mm away from the ear canal, and aligned with the reference point.

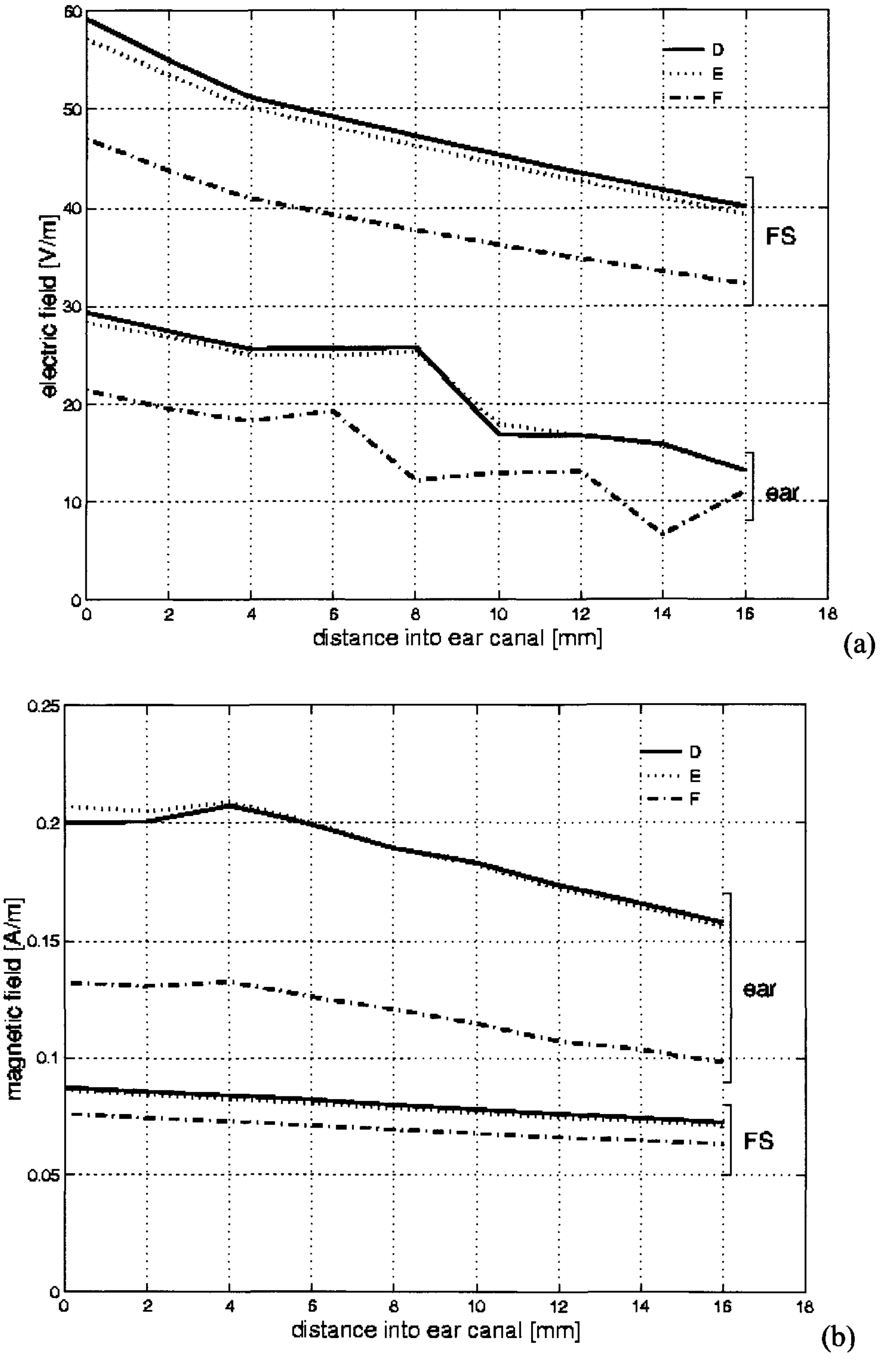

Figure 7-13 The electric field (a) and magnetic field (b) magnitude in free space (FS) and the ear canal (E) for the normal shape ear-model and various positions of the telephone. Antenna extended. D - telephone shifted 8 mm towards the mouth. E - the center of earphone in the reference point (Fig. 6-1). F – the earphone 8 mm away from the ear canal, and aligned with the reference point.

Certain self-consistent features of the field behavior in the ear canal can be observed. One of them is that for the electric fields the order of the curves for the field magnitude in the ear canal in general, corresponds to that of the field magnitude in free space. The relationship is not evident to the same extent for the magnetic fields but generally reasonable. The behavior of the magnetic fields is reasonable in view of the free space field distribution and previous reported results [76].

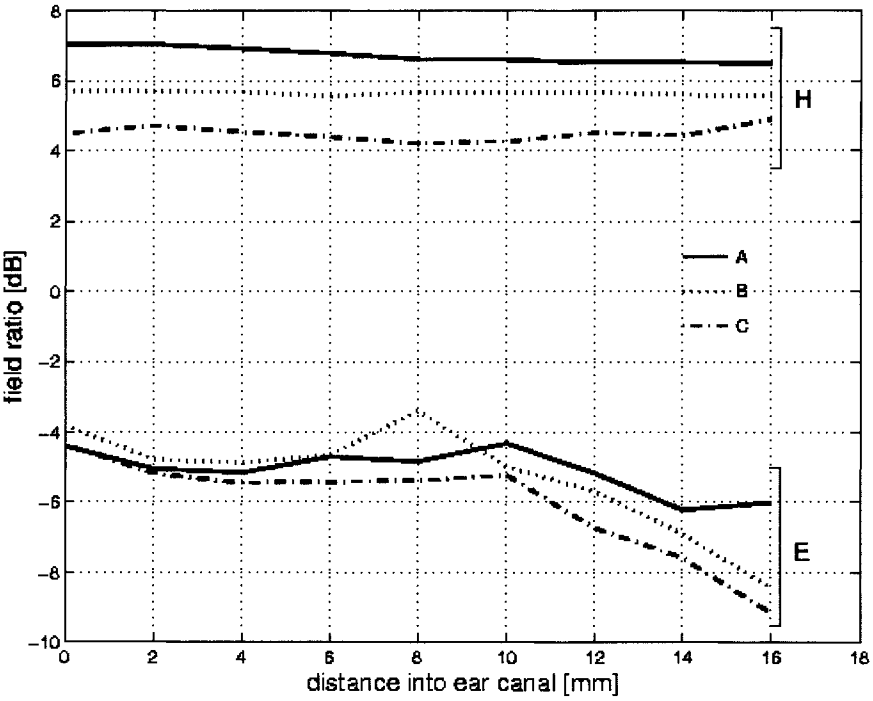

Figure 7-14 Ratio of the electric (E) fields and magnetic (H) field in the ear canal to those in free space for the flattened ear-model and various positions of the telephone. Antenna extended. A- the center of earphone in the reference point (Figure 6-1). B - the earphone 4 mm away from the ear canal, and aligned with the reference point. C - the earphone 12 mm away from the ear canal, and aligned with the reference point.

The ratios of the electromagnetic fields in the ear canal and free space are given in Figure 7-14 and 7-15 for the two models of the ear. For both ear models, the magnetic field ratios change little with distance into the ear.

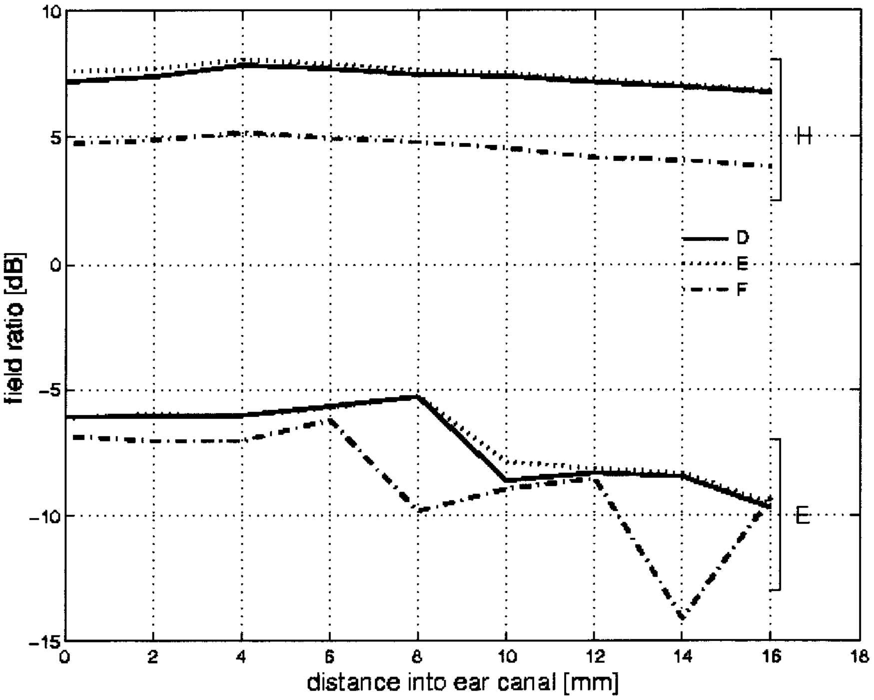

Figure 7-15 Ratio of the electric (E) fields and magnetic (H) field in the ear canal to those in free space for the normal shape ear-model and various positions of the telephone. Antenna extended. D - telephone shifted 8 mm towards the mouth. E - the center of earphone in the reference point (Figure 6-1). F – the earphone 8 mm away from the ear canal, and aligned with the reference point.

The variations are greater for the electric field ratios, which is consistent with data shown in Figure 7-12(a) and Figure 7-13(a). On the other hand, the electric field close to 10-12 mm into the ear (where the hearing aid is located) varies little. For the placements of the handset as in Figure 7-6 and as in the acoustic tests, the magnetic field ratios are 6.7 and 7.5 dB for the two ear models.

7.7.3 EMI evaluation

The acoustic measurements indicated that, when the hearing aid was placed in the ear of three subjects, the average SPL increased by 7.4 dBA, with a standard deviation of 0.77 dBA compared to the reference case. The fact that the SPL increases, relative to free space exposure, when the hearing aid is placed in the ear of a person is consistent with an increased magnetic field strength. The relationship between the output of the hearing aid, i.e., 217 Hz acoustic sound pressure level (SPL) and the RF power delivered to the dipole, is shown in Figure 7-16.

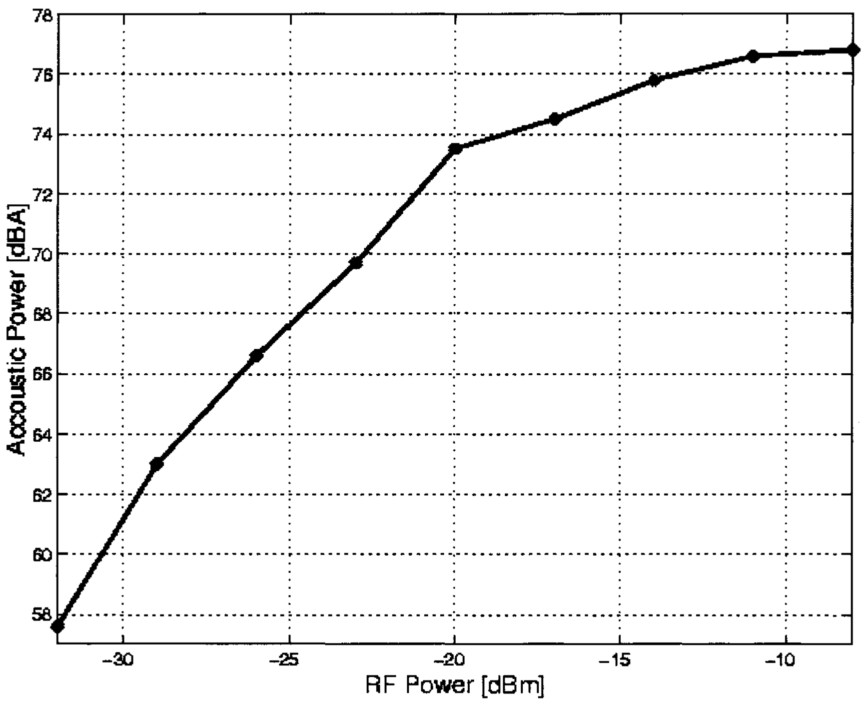

Figure 7-16 Acoustic power at 217 Hz as a function of the RF power, data used to normalize the hearing aid SPL measurements.

As can be seen, the relationship for lower values of power was approximately-linear. As RF power was increased in 3 dB increments, the hearing aid output SPL increased correspondingly, but at higher RF levels the hearing aid SPL appeared to saturate, and the increases in output SPL were lower for each subsequent 3-dB increase in RF power.

7.7.4 Interpretation of results

For the telephone and hearing aid investigated, the results of the acoustic tests correlate well with the ratio of the magnitudes of the magnetic fields in the auditory canal and free space. Even though this does not preclude the possibility for the E-field also causing the EMI, the coupling through the H-field appears to be the predominant one. There is a direct avenue for this coupling, as the hearing aid microphone contains a coil. On the other hand, a visual examination of the hearing aid, has also revealed other wires forming loops, which may take part in the coupling.

There is variability in both acoustic and electromagnetic data. The ratios of the magnitude of electromagnetic fields in the ear and free space vary depending on the ear shape and the placement of the handset. Directional field components vary even more. The ratios of the magnetic fields for the two ear shapes for telephone and hearing aid locations corresponding to those of the acoustic test are about 7 dB. This compares well with an average normalized SPL of 7.4 dB. Our data point out that it may be possible to predict hearing aid SPL based on magnetic field strength. However, other factors must be considered before any general conclusions can be drawn. These include the gain setting of the hearing aid, the absolute SPL produced by the hearing aid, and the absolute RF power level at a location of the hearing aid.

7.8 Summary

Selected examples described illustrate the application of the human body models and numerical codes to problems of practical importance. The facility to manipulate the human model described in Chapter 3 was used to obtain representative models for the situations evaluated. In all cases, use of supercomputer and parallel codes were essential.

The SPFD method and the body model have been applied to evaluate the EMI due to 60 Hz magnetic fields with implanted cardiac pacemakers. Approximations derived directly from Faraday's law have also been obtained for the same configurations of the electrode leads. The EMI potentials obtained in SPFD computations are significantly different from Faraday's law estimates. This is due to the complex three-dimensional paths in which the current flows between the pacemaker electrodes. Thus, the induced potential at pacemaker input depends not only on the length of the lead and its placement with respect to the direction of the magnetic field, but also on the conductive path in tissues which completes the inductive loop.

In the modeling of a handheld telephone interaction with the head, the accurate representation of the near fields of its dual helix antenna system was of particular importance. An FDTD model of the antenna system was created by discretizing both helices along the mesh edges. The discretized helix is square in cross-section and has a staircase rather than smooth spiral shape. This inherently inaccurate representation has been fine tuned by the adjustment of mesh step, to closely match the near fields of the real antenna that were experimentally determined in Motorola labs. Such validated FDTD model of the transmitter system has been used together with the high-resolution head model to determine antenna characteristics when operating in the proximity of the head. The RF power absorption field in the head has been post-processed to obtain the 1g and 10g SAR, for which the algorithm described in Chapter 5 was critical.

Furthermore, the validated model of the telephone has been applied to determine the influence that the proximity of the head has on the EMI that a GSM telephone has on a hearing aid device. It has been determined that inside the ear canal, there is a decrease of the electric field and increase of the magnetic field component in comparison with the same relative position to the transmitter operating in free space. In independent experiments performed in the FDA laboratory it has been found that the acoustic interference with the hearing aid increases when the device is worn in the ear of a human subject compared with the device in the same relative position to the transmitter but suspended in free space. This confirms that the coupling between the transmitter and the device is mostly through the magnetic component of the interfering field.

8 Conclusions and Future Work

8.1 Conclusions

The main objectives of this work were all related to determining the interactions between the external sources of electromagnetic fields and human body organs and tissues. Computer modeling is, at present, the only practical method of observing the physical effects of arbitrarily applied external electromagnetic fields in all body organs and tissues. Modeling has also been used to evaluate effects of body proximity on electronic devices. Due to interest of the research community, and the society at large, two frequency ranges have been the focus of the investigation: power line frequencies, which belong to the ELF band, and cellular telephone frequencies, which are a part of microwaves.

At ELF frequencies, the objective of modeling is to map the induced electric field and resultant current density in organs and tissues due to external fields: electric or magnetic. This serves the purpose of dosimetry, and provides means for biologists and physiologists studies. Modeling of induced fields in the body is also helpful in predicting the EMI problems with implanted electronic devices, such as heart pacers or defibrillators.

At RF frequencies, the physical effect of interest is the absorption of RF energy in body tissues. The parameter that describes and quantifies the interaction is the Specific Absorption Rate (SAR). The guidelines and regulations for public safety in RF exposure are expressed in terms of weight averaged SAR. The objective of modeling in this case is to map the weight averaged SAR in the body and to find its maximum value in the whole body or in a body part. Further, it is generally known that at RF frequencies the proximity of the body strongly affects the performance of transmitter systems, such as personal communication devices, and may trigger EMI with electronic devices implanted or worn in body cavities. These effects can also be modeled with appropriate body models and electromagnetic codes.

The original contributions described in this dissertation fall in three categories: development of body models, verification of computational methods to determine fields induced in body models, and application of modeling to selected problems of practical importance. The following summarizes these contributions.

- A whole body model of a male adult discretized on a 3.6 mm grid has been developed. A variety of tools and methods for model building and manipulating has been created in the process as described in Chapter 3 and Appendix B. Based on this model and using these tools a number of derived models has been created, as also described in Chapter 3.
- Existing electromagnetic codes SPFD and FDTD have been used to compute fields in body models as outlined in Chapter 4. Both codes have been extended to the supercomputer platform and validated for use with body models by comparison with other codes applied to the same problems as detailed in Chapter 6. The FDTD code has been augmented with a new post-processing algorithm to compute the weight averaged SAR. Development of this algorithm is the subject of Chapter 5.
- The use of a body model and the SPFD code to address the issue of strong magnetic fields affecting a heart pacer device has been described as an example of modeling the ELF fields in the body. The heart and major blood vessels in the model have been refined to assure electrical continuity. The metallic box of the pacer has been embedded in the body model in the position indicated by X-rays of cardiac patients and the pacer leads have been threaded along the major veins and into the heart to

reproduce the configuration from the X-rays. Modeling the induced eddy currents due to 50 Hz magnetic field allowed the evaluation of the EMI potentials acting on the heart pulse sensing circuit in the device.

- Modeling of a cellular phone transmitting in a realistic position relative to the human head has been presented as an example of using the FDTD code with body model at RF frequency range. Accurate representation of the near field of a helical antenna utilized in the investigated telephone has been validated. The validated model of the telephone has been applied to determine the influence of the head proximity on performance of the telephone antenna, to compute the SAR in the head, and to evaluate the EMI of the transmitter with the hearing aid device worn inside the ear canal of a human subject.

8.2 Future Work

Computer modeling will likely remain the only viable method to determine the electric fields inside body organs and tissues in many practical situations. The availability of more powerful computers and refinement of computer codes will allow the determination of the fields inside the human body in greater detail and allow for more realistic models of EM emitting devices to be incorporated. To accomplish this the existing models and codes will have to be further improved. New computer codes and algorithms will have to be developed, that are hybrid in nature, and combine the strengths of different techniques.

While the already developed models and tools for their modification can be used to solve many other problems, there are other models that need to be developed. So far only a male body model is available. However, there is considerable interest in modeling the induced fields in a fetus for power line exposures and for some RF exposures, such as those resulting from operating plastic sealer machines. Existing models are only compatible with computer codes that use Cartesian meshes. However, FEM offers many advantages in modeling interactions of electromagnetic fields with human body. A lack of compatible models is one of the factors why this method has not been used. Thus, further modification and extension of the existing tools for model modification to obtain surface representations of major organs is of importance for the future research.

Regarding modeling of wireless device - human body interactions, there are many devices other than handheld telephones that need to be evaluated. Furthermore, they can only be evaluated by modeling, as experimental evaluation of SAR is cumbersome for such devices. Examples of such devices are laptop computers with wireless modems, personal data assistants, indoor LANs etc. In those cases, often other parts of the body in addition to the head need to be taken into account. Modeling of these devices, where often the separation between the device and the human body is of the order of one to few wavelengths, is likely to call for use of hybrid methods. For instance, method of moments may be used to model the antenna and device and FEM or FDTD to model the human body.

Bibliography

1. J. D. Kraus, *Electromagnetics., (4^{th} ed.),* McGraw-Hill, 1992.

2. R. P. Feynman, *The Feynman Lectures On Physics, vol. 2,* Addison-Wesley, 1964.

3. "IEEE Standard for Safety Levels with Respect to Human Exposure to Radio Frequency Electromagnetic Fields, 3 kHz to 300 GHz", IEEE standards Coordinating Committee 28, Institute of Electrical and Electronics Engineers, Inc., New York, NY, 1991

4. E. Postow, M. L. Swicord, "Modulated Fields And Window Effects", *Handbook of Biological Effects of Electromagnetic Fields,* eds. C. Polk and E. Postw, CRC Press, Boca Raton, 1996, pp. 535-580

5. S. S. Stuchly, A. Kraszewski, M. A. Stuchly, G. W. Hartsgrove, and R. J. Spiegel, "RF energy deposition in a heterogeneous model of man: far-field exposures", *IEEE Trans. Biomed. Eng.,* 34, 1987a, pp. 944-950.

6. H. P. Schwan, and K. Li, "Hazzards due to total body irradiation by radar", *Proc. IRE,* 44, 1572, 1956.

7. C. C. Johnson, C. H. Durney, and H. Massaudi, "Long-wavelength electromagnetic power absorption in prolate spheroidal model of man and animals", *IEEE Trans. Microwave Theory Tech.*, 23, 739, 1975.

8. C. H. Durney, C. C. Johnson, and H Massaudi, "Long-wavelength analysis of plane wave irradiation of a prolate spheroidal model of man", *IEEE Trans. Microwave Theory Tech.*, 24, 41, 1977.

9. H. Massaudi, C. H. Durney, and C. C. Johnson, "Long-wavelength electromagnetic power absorption in ellipsoidal models of man and animals", *IEEE Trans. Microwave Theory Tech.*, 23, 739, 1975.

10. O. P. Gandhi, E. L. Hunt, and J. A. D'Andrea, "Deposition of EM energy in animals and in models of man with and without grounding and reflector effects", *Radio Sci.*, 12, 39S, 1977.

11. J. F. DeFort, O. P. Gandhi, and M. J. Hagmann, "Moment-Method solutions and SAR calculations for inhomogeneous models of man with large number of cells", *IEEE Trans. Microwave Theory Tech.*, 31, 848, 1983.

12. V., Spitzer, M. L., Ackerman, A. L. Scherzinger, D. Whitlock, "The visible human male: a technical report". *J. Am. Med. Inform. Assoc.*, 3(2), 118, 1996.

13. N. Kuster and Q. Balzano, "Energy absorption mechanism by biological bodies in the near field of dipole antennas above 300 MHz", *IEEE Trans. Vehicular Tech.,* 41, 1,

1992.

14. Q. Balzano, O. Garay, J. Manning, “Electromagnetic Energy Exposure of Simulated Users of Portable Cellular Telephones”, *IEEE Trans. Vehicular Tech.,* 44, 3, 1995.

15. K. S. Yee, “Numerical solution of initial boundary value problems involving Maxwell’s equations in isotropic media”, *IEEE Trans. Antennas and Propagation,* vol. 14, 1966.

16. A. C. Eycleshymer and A. C. Schoemaker, *A Cross-Section Anatomy*, Appleton-Century-Crofts, New York, 1970.

17. J. Y. Chen and O. P. Gandhi, “Curents induced in an anatomically based model of a human for exposure to vertically polarised electromagnetic pulses”, *IEEE Trans. Microwave Theory Techn.*, 39, 31, 1991.

18. W. Xi, M. A. Stuchly and O. P. Gandhi, “Induced currents in models of man and rodents from 60 Hz magnetic fields”, *IEEE Trans. Biomed. Eng.,* 41, 11, 1994.

19. I. G. Zubal, C. R. Harrell, E. O. Smith, Z. Rattner, G. Gindi and P. B. Hoffer, “Computerized three-dimensional segmented human anatomy”, *Med. Phys.*, 21, 2, 1994, pp. 299-302.

20. T. W. Dawson, J. De Moerloose, and M. A. Stuchly, ”Comparison of magnetically induced ELF fields in humans computed by FDTD and scalar potential FD codes”, *ACES J.*, 11, 1996, pp. 63-71.

21. T. W. Dawson, and M. A. Stuchly, “A comparison of analytical and numerical solutions for induction in a sphere with equatorially varying conductivity by low-frequency uniform magnetic fields of arbitrary orientation”, *Proc. ACES*, 1997, pp. 533-540.

22. M. N. Sadiku, *Numerical Techniques in Electromagnetics*, CRC Press, 1992.

23. A. Taflove, S. C. Hagness, *Computational Electrodynamics: The Finite-Difference Time-Domain Method,* Second Edition, Artech House, 2000.

24. K. P. Hwang, A. C. Cangellaris, “Effective permittivities for second-order accurate FDTD equations at dielectric interfaces”, *IEEE Microwave and Components Lett.*, vol. 11, 2001, pp. 158-160.

25. D. Popovic, M. Okoniewski, “Effective permittivity at the interface of dispersive dielectrics in FDTD”, *IEEE Microwave and Components Lett.*, vol. 12, 2002.

26. Electric Power Research Institute (EPRI), “Evaluation of occupational magnetic field exposure guidelines”, Palo Alto, CA, TR-111501, 1998.

27. K. R. Foster and H. P. Schwan, “Dielectric properties of tissues”, *Handbook of*

Biological Effects of Electromagnetic Fields, eds. C. Polk and E. Postow, CRC Press, Boca Raton, 1996, pp. 25-102.

28. S. Gabriel et al, “The dielectric properties of biological tissues: II. Measurements in the frequency range 10 Hz to 20 GHz”, *Phys. Med. Biol.,* vol. 41, 1996, pp. 2251-2269.

29. S. Gabriel et al, “The dielectric properties of biological tissues: III. Parametric models for dielectric spectra of tissues”, *Phys. Med. Biol.*, vol. 41, 1996, pp. 2271-2293.

30. M. A. Stuchly and T. W. Dawson, “Interaction of low-frequency electric and magnetic fields with the human body,” *Proc IEEE,* vol. 85, no. 5, 2000, pp. 643-664.

31. F. S. Barnes, “The effects of time varying magnetic fields on biological bodies”, *IEEE Transactions on Magnetics,* vol 26, no. 5, 1990.

32. T.S. England and N. A. Sharples, “Dielectric properties of the human body in the microwave region of the spectrum”, *Nature,* vol. 163, 1949, pp. 487-488.

33. T.S. England, “Dielectric properties of the human body for wave lengths in the 1-10 cm range”, *Nature*, vol. 166, 1950, pp. 480-481.

34. J.R. Mallard and D.G. Lawn, “Dielectric absorption of microwaves in human tissues,” *Nature,* vol. 213, 1967, pp. 28-30.

35. L. A. Geddes, and L. E. Baker, “The specific resistance of biological material – a compendium of data for the biomedical engineer and physiologist”, *Med. Biol. Eng.*, 5, 271, 1967.

36. M. A. Stuchly, and S. S. Stuchly, “Dielectric properties of biological substances – tabulated”, *J. Microwave Power,* 15, 19, 1980.

37. F. A. Duck, *Physical properties of tissue: A comprehensive reference book*, Academic Press, 1990.

38. D. E. Dudgeon, R. M. Mersereau, *Multidimensional Digital Signal Processing*, Prentice-Hall, 1984.

39. P.Z. Peebles, *Probability, random variables, and random signal principles*, McGraw-Hill, 1993.

40. *IBM Visualization Data Explorer, Programmer's Reference*, IBM corporation, 1995.

41. P. J. Dimbylow, “Induced current densities from low-frequency magnetic fields in a 2 mm resolution, anatomically realistic model of the body”, *Phys. Med. Biol.* 43, 1997, pp. 221-230.

42. P. J. Dimbylow "FDTD calculations of the whole-body averaged SAR in an anatomically realistic voxel model of the human body from 1 MHz to 1 GHz", *Phys. Med. Biol.* 42, 1997, pp. 479-490.

43. International Comission on Radiological Protection, *Report of the Task Group on Reference Man*, ICRP Report 23, 1975.

44. O. P. Gandhi and J. Y. Chen, "Numerical dosimetry at power line frequencies using anatomically based models", *Bioelectromagn. J. Supp.*, **1,** 1992, pp. 43-60.

45. R. F. Harrington, *Time-Harmonic Electromagnetic Fields*, McGrow-Hill, 1961.

46. D. M. Sullivan, D. T. Borup, and O. P. Gandhi, "Use of the Finite-Difference Time-Domain Method in Calculating EM Absorption in Human Tissues", *IEEE Transactions on Biomedical Engineering*, vol. 34, no. 2, 1987, pp. 148-157.

47. T. W. Dawson, and M. A. Stuchly, "High resolution organ dosimetry for human exposure to low frequency magnetic fields", *IEEE Trans. Magn.*, **34,** 1998, pp. 1-11.

48. B. Hutzler, P. Baraton, J. L. Vicente, J. C. Antoine, M. Roux, and J. P. Urbain "Exposure to 50 Hz magnetic fields during live work", *Proc. CIGRE,* 1994, pp. 1-9.

49. International Commission on Non-Ionizing Radiation Protection (ICNIRP), "Guidelines for limiting exposure to time-varying electric, magnetic and electromagnetic fields (up to 300 GHz)", *Health Physics,* **74,** 1998, pp. 494-522.

50. T. W. Dawson, K. Caputa and M. A. Stuchly, "Numerical evaluation of 60 Hz magnetic induction in the human body in complex occupational environments", *Physics in Medicine & Biology* **44**(4), 1999, pp. 1025-1040.

51. T. W. Dawson, M. Potter and M. A. Stuchly, "Accuracy evaluation of modeling of low frequency field interactions with the human body", *ACES J.*, **16**, 2, 2001, pp. 162-172.

52. T. W. Dawson, K. Caputa and M. A. Stuchly, "Influence of human model resolution on computed currents induced in organs by 60 Hz magnetic fields", *Bioelectromagnetics,* 18**,** 1997, pp. 478-490.

53. M. A. Stuchly and O. P. Gandhi, "Inter-laboratory comparison of numerical dosimetry for human exposure to 60 Hz electric and magnetic fields", *Bioelectromagnetics*, 21**,** 2000, pp. 167-174.

54. P. S. Astridge, G. C. Kay, S. Whitworth, P. Kelly, A. J. Camm, and E. J. Perrins, "The response of implanted dual chamber pacemakers to 50 Hz extraneous electrical interference", *P.A.C.E.,* vol. 16, 1993, pp. 1966-1974.

55. G. C. Kaye, G. S. Butrous, A. Allen, S. J., Meldrum, J. C. Male, and A. J. Camm, "The effect of 50 Hz external electrical interference on implanted cardiac

pacemakers", *P.A.C.E.,* vol. 11, 1988, pp. 999-1008.

56. T. W. Dawson, M. A. Stuchly, K. Caputa, A. Sastre, R. B. Shepard, and R. Kavet, "Pacemaker interference and low frequency electric induction in humans by external fields and electrodes," *IEEE Trans. Biomed. Eng.,* vol. 47, no. 9, 2000, pp. 1211-1218.

57. W. Irnich, "Interference in pacemakers", *P.A.C.E,* vol. 7, 1984, pp. 1021-1048.

58. A. Sastre, "Susceptibility of implanted pacemakers and defibrillators to interference by power-frequency electric and magnetic", Tech. Rep., EPRI Report, A.S. Consulting & Research, Inc., 1997.

59. T. W. Dawson, K. Caputa, and M. A. Stuchly, "Organ dosimetry for human exposure to non-uniform 60 Hz magnetic fields", *IEEE Trans. Power Delivery,* vol. 14, no. 4, 1999, pp. 1234-1239.

60. T. W. Dawson, K. Caputa, and M. A. Stuchly "Numerical evaluation of 60 Hz magnetic induction in the human body in complex occupational environments", *Phys. Med. Biol.,* vol. 44, no. 4, Apr 1999, pp. 1025-1040.

61. B. Nowak, T. Voiglander, E. Himmrich, et al., "Cardiac output in single lead VDD pacing versus rate-matched VVIR pacing", *Am. J. Cardiology*, vol. 75, 1995, pp. 904-907.

62. M. A. Jensen and Y. Rahmat-Samii, "EM interaction of handset antennas and a human in personal communications" *Proceedings of IEEE,* vol. 83, no. 1, 1995, pp. 7-17.

63. M. Okoniewski and M. A. Stuchly, "A study of the handset antenna and human body interaction", *IEEE Trans. Microwave Theory Techn.*, 44, 1996, pp. 1855-1864.

64. O. P. Gandhi, G. Lazzi and C. M. Furse, "Electromagnetic absorption in the human head and neck for mobile telephones at 835 and 1900 MHz", *IEEE Trans. Microwave Theory Techn.,* 44, 1996, pp. 1884-1897.

65. A. Tinnigswood, C. M. Furse and O. P. Gandhi, "Computations of SAR distribution for two anatomically based models of the human head using CAD files of commercial telephones and parallelized FDTD code", *IEEE Trans. Antennas Propagat.*, 46, 1998, pp. 829-833.

66. Q. Yu, O. P. Gandhi, M. Aronsson and D. Wu, "An automated SAR measurement system for compliance testing of personal wireless devices", *IEEE Trans. Electromag. Compat.,* 41, 1999, pp. 234-245.

67. K. Thomas, *LC User's Guide, version 2.7,* 10 Feb. 1999, (http:/ /lc.cray.com).

68. J. Anderson, M. Okoniewski and S. S. Stuchly, "Practical 3D contour/staircase

treatment of metals in FDTD", *IEEE Microwave and Guided Wave Letters,* 6, 1996, pp. 146-148.

69. G. Lazzi, Q.-S. Yu, and O. P. Gandhi, "Extension and Validation of Equivalent Source Helical Antenna Modeling with the FDTD Code", *IEEE Microwave and Optical Technology Letters,* vol. 23, no. 3, 1999, pp. 172-174.

70. IEEE Standard C95.1-1991, *IEEE standard for safety levels with respect to human exposure to radio frequency electromagnetic fields, 3 kHz to 300 GHz,* Institute of Electrical and Electronics Engineers, Inc., New York, 1992.

71. Federal Communications Commission, "Guidelines for Evaluating the Environmental Effects of Radiofrequency Radiation," ET Docket No. 93-62. Washington, 1996.

72. CENELEC, European Committee for Electrotechnical Standarization, "Considerations for Human Exposure to EMFs from Mobile Telecommunication Equipment (MTE) in the Frequency Range 30 MHz – 6 GHz", 1996.

73. M. Skopec, "Hearing aid electromagnetic interference from digital wireless telephones", *IEEE Trans. Rehabilitation Eng.*, vol. 6 (2) , 1998, pp. 235-239.

74. F. K. Kuk and K. H. Nielsen, "Factors affecting interference from digital cellular telephones", *The Hearing J.,* vol. 50, 1997, pp. 32-34.

75. T. A. Victorian, "An update on digital cellular telephone interference and hearing aid compatibility", *The Hearing J.*, vol. 41, 1998, pp. 53-60.

76. M. Okoniewski and M. A. Stuchly, "Modeling of interaction of electromagnetic fields from a cellular telephone with hearing aids", *IEEE Trans. Microwave Theory Tech.,* vol. 46 (11), November 1998, pp. 1686-1693.

77. J. Berenger, "A perfectly matched layer for the absorption of electromagnetic waves", *Journal of Computational Physics*, vol. 114, 1994, pp. 185-200.

78. S.L. Horowitz, T. Pavlidis, "Picture Segmentation by a tree traversal algorithm", *Journal of The Association for Computing Machinery*, vol. 23, no. 2, 1975, pp. 368-388.

79. T. S. Tenforde, W.T. Kaune, "Interaction of extremely low frequency electric and magnetic fields with humans", *Health Phys.* vol. 53, 1987, pp. 585-606.

80. A. K. Hirata, Caputa, T. W. Dawson and M. A. Stuchly, "Dosimetry in models of child and adult for low-frequency electric field", *IEEE Trans. Biomedical Engineering,* 48 (9), September 2001, pp. 1007-1012.

81. P.J. Dimbylow, "Fine resolution calculations of SAR in the human body for frequencies up to 3 GHz", *Phys. Med. Biol.* 47, 2002, pp. 2835-2846.

82. M. Rahman, M. A. Stuchly, “Transmission Line-Periodic Circuit Representation of Planar Microwave Photonic Bandgap Structures”, *Microwave and Optical Technology Letters*, vol. 30, no. 1, July, 2001, pp. 15-19.
83. E.C. Fear, S.C. Hagness, P. M. Meaney, M. Okoniewski, and M. A. Stuchly, “Enhancing Breast Tumor Detection with Near-Field Imaging”, *IEEE Microwave Magazine*, vol. 3, no. 1, March, 2002, pp. 48-56.
84. Dawson, T. W., K. Caputa, M. A. Stuchly and R. Kavet, “Electric fields in the human body resulting from 60-Hz contact currents”, *IEEE Trans. Biomedical Engineering,* 48 (9), pp. 1020-1026, September 2001.

Apendix A. Organs and tissues of UVic man

Table A-1 Tissues and organs of UVic man

Tissue	Voxel count	Volume [cc]	Tissue	Voxel count	Volume [cc]
air outside	4221902	196977.06	hard palate	655	30.56
skin	126590	5906.18	cerebellum	3289	153.45
csf	5018	234.12	tongue	1156	53.93
spinal cord	3752	175.05	horn of mand.	286	13.34
skull	10237	477.62	nasal septum	132	6.16
spine	17595	820.91	brain white	11342	529.17
rib cage	29700	1385.68	sup. sag. sinus	335	15.63
pelvis	14400	671.85	medulla oblon.	99	4.62
long bones	65235	3043.60	frontal lobes	2646	123.45
muscle	743065	34668.44	pons	486	22.67
lung	62364	2909.65	third ventricle	211	9.84
heart	9354	436.42	pineal body	2	0.09
liver	30192	1408.64	occipal lobes	1566	73.06
gall bladder	329	15.35	hippocampus	162	7.56
kidney	7618	355.43	pituitary gland	3	0.14
pharynx	332	15.49	fat - head	9949	464.18
esophagus	642	29.95	uncusi - bone	19	0.89
stomach	5133	239.49	rurbinates	123	5.74
small bowel	26447	1233.91	caudate nucl.	239	11.15
colon	18284	853.06	zygoma	182	8.49
pancreas	792	36.95	insula cortex	291	13.58
adrenals	62	2.89	sinuses/mouth	3755	175.19
fat	329602	15377.91	putamen	226	10.54
blood	21033	981.32	optic nerve	31	1.45
gas (bowel)	3167	147.76	internal caps.	213	9.94
fluid (bowel)	528	24.63	septum palluc	29	1.35
bone marrow	29908	1395.39	thalamus	249	11.62
thyroid	105	4.90	eye retina	178	8.30
trachea	1182	55.15	corpus collos.	291	13.58
cartilage	900	41.99	sp. fr. lobes	179	8.35
spleen	5568	259.78	cereb. falx	85	3.97
urine	6597	307.79	temp. lobes	5263	245.55
feces	1134	52.91	fourth ventr.	38	1.77
testes	1479	69.00	eye cornea	21	0.98
prostate	438	20.44	pariet. lobes	2657	123.96
rectum	1467	68.44	amygdala	91	4.25
diaphragm	4528	211.26	eye humor	332	15.49
bladder	3147	146.83	globus pallid.	86	4.01
dens of axis	57	2.66	eye lens	8	0.37
jaw bone	1635	76.28	cereb. aqued.	13	0.61
parotid gland	706	32.94	lat. ventric.	215	10.03
lacrimal gland	49	2.29	prefront lobes	1157	53.98
spinal canal	265	12.36	teeth	217	10.12

Apendix B. Image segmentation software

Software for medical image segmentation has been developed for the HP UNIX workstation specifically to convert scan images of the Visible Human into voxel layers of the UVic body model. A co-op student proficient in C and X11 graphics has done coding of the program. The program comprises 3 functional modules:

- Input-output module for reading three different formats of medical images used in VHP data ('raw' data format of color images, and manufacturer specific formats of the CT and MRI machines used by the VHP). Image information is extracted from a file, normalized and reduced in resolution to fit in an array of pixels of 256x256. After the processing, the resulting array of voxels of 256x256 is stored in a file.
- Image segmentation module that subdivides the image into a number of disjoint regions encompassing pixels of similar image density. An already written and debugged routine from a student project that implements an algorithm from a classic image segmentation paper [78] has been utilized for this function.
- Graphical user interface for labeling and manipulating segmented images. In addition to attaching tissue tags to segmented regions by pointing and clicking with a mouse the program also supports rudimentary image editing to correct the results of automatic segmentation (cleaving regions along a mouse drawn line)

The program is operated as follows. On a startup a blank canvas window appears with a pull down menu for selecting image files. Following the selection of a file a second window appears with the gray scale view of the image (Figure B-1a). Selecting the 'process' option from the pull-down menu starts the segmentation algorithm. Depending on the image complexity the processing may take from under a minute to several minutes. The end of processing is signaled with the appearance of uniform gray scale regions in place of the original image. These regions must be manually classified and labeled by the person operating the program. A region label, such as 'bone', 'liver' or 'blood' is selected from a pull down menu. A region clicked with a mouse becomes colored appropriately to the selected tissue type. This stage of the operation is shown in Figure B-1b. When the operator is satisfied with the labeled parts, clicking the right button of the mouse on a labeled region pastes that region in the canvas window. Figure B-1c shows segmented arms with clearly defined bone, muscle and fat tissues that have been pasted from the process window.

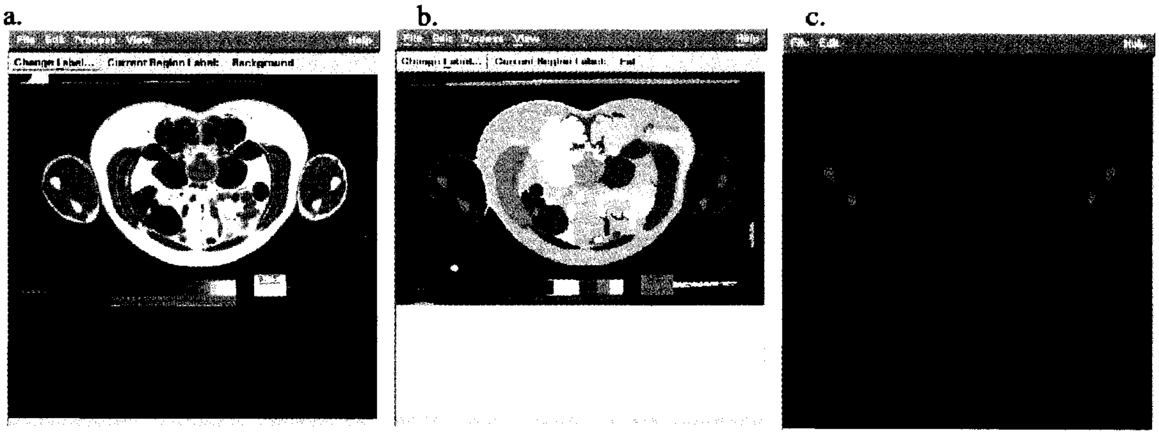

Figure B-1 Segmenting and labeling VHP image: a. gray scale body cross-section, b. image segmented (gray scale), labeled segments highlighted in color: 'bone' (green), 'fat' (blue-gray) and 'muscle' (purple) c. labeled segments assembled on canvas

More than one process windows can be open at the same time. The segmentation algorithm has several adjustable parameters which can be tuned to bring out details in the image. The regions obtained using different parameters can be selectively pasted on canvas from several process windows. A region pasted on top of a previously pasted region overrides the previous labeling. In practical use one process window is also open with the unprocessed image for visual reference.

Apendix C. Model viewing and editing software

Program for viewing and editing voxel layers of body models has been written to primarily view and inspect the results of model manipulations by dedicated programs without graphical capabilities, as described in Chapter 3 section 3.2. The layer viewer has been written in C using X11 graphical libraries of UNIX. In addition to displaying the cross-sections, program also performs searching the entire model for a selected tissue and has layer editing capabilities.

The main objective of creating a dedicated program for model viewing was to speed up the cycle of model modification and inspection. By using block data transfers from model file to memory and using byte arrays as an internal storage the loading of UVic model and displaying a selected cross-section takes about a second, whereas the same operation previously performed by a Matlab program took over a minute.

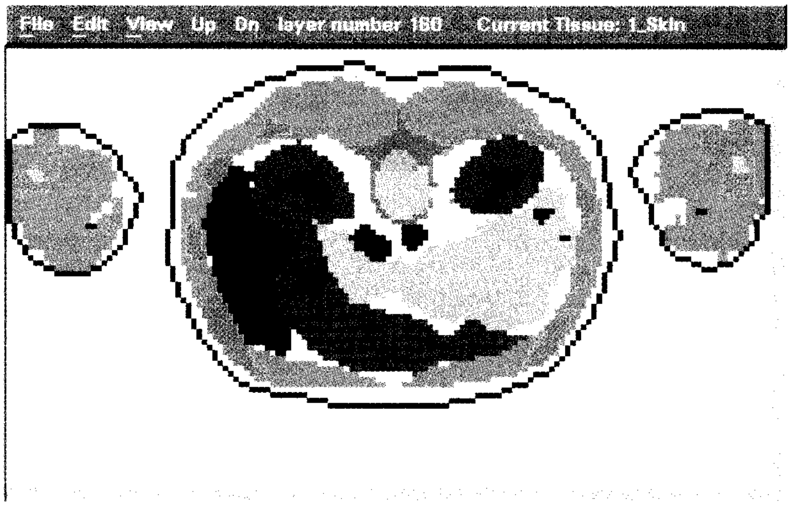

Figure C-1 Model viewer showing layer 160 of the UVic model.

The viewer is invoked by specifying on the command line the model file and the layer number for the initial display, e.g. layer 160 in Figure C-1. Scrolling through the layers is performed with the ‘up’ and ‘down’ buttons in the menu bar. An arbitrary number of the layer can also be entered after selecting ‘layer number’ from the menu. Clicking a voxel on the display changes the tissue displayed on the menu bar to that of the pointed voxel. This serves a dual purpose, one is to identify the voxel selected, second is to designate the tissue for the subsequent editing operations. Alternatively the tissue for subsequent operations can be selected with the pull-down menu.

Three modes of editing are available: single voxel, line of voxels, and filled rectangle. In the single voxel mode, the voxel clicked with the middle mouse button changes to the current tissue. In the line mode a continuous straight line of voxels of the current tissue is drawn between two points clicked with the middle button. In the rectangle mode the two points clicked with the middle button become opposite corners of a rectangle of the current tissue. A single level ‘undo’ operation is provided in the edit menu.

Although editing features of the program have been used to some extent to quickly correct small model errors (such as the presence of disconnected voxels) the primary function of the program is to find the coordinates of voxels pointed on the screen, that can later be used in refining the model. Each time the mouse button is clicked on a voxel the x,y,z indices of the voxel are printed in the standard output and also recorded in a log file for the session. An important feature for model inspection and refinement is the ‘find’ function of the edit menu. This function searches the model in a layer-by-layer fashion for an arbitrary tissue selected from the Current Tissue menu.

The model viewer and editor has been undergoing a continuous development. Current version of the program (Figure C-2) runs on a linux workstation and is based on QT graphical library which offers easy access to sophisticated widgets and display controls. The new program displays simultaneously three panels with the x-, y- and z- cross-sections of the model. Scrolling through layers is performed with the use of sliders. The location of cross-sections displayed in the other panels is shown as cross-hairs.

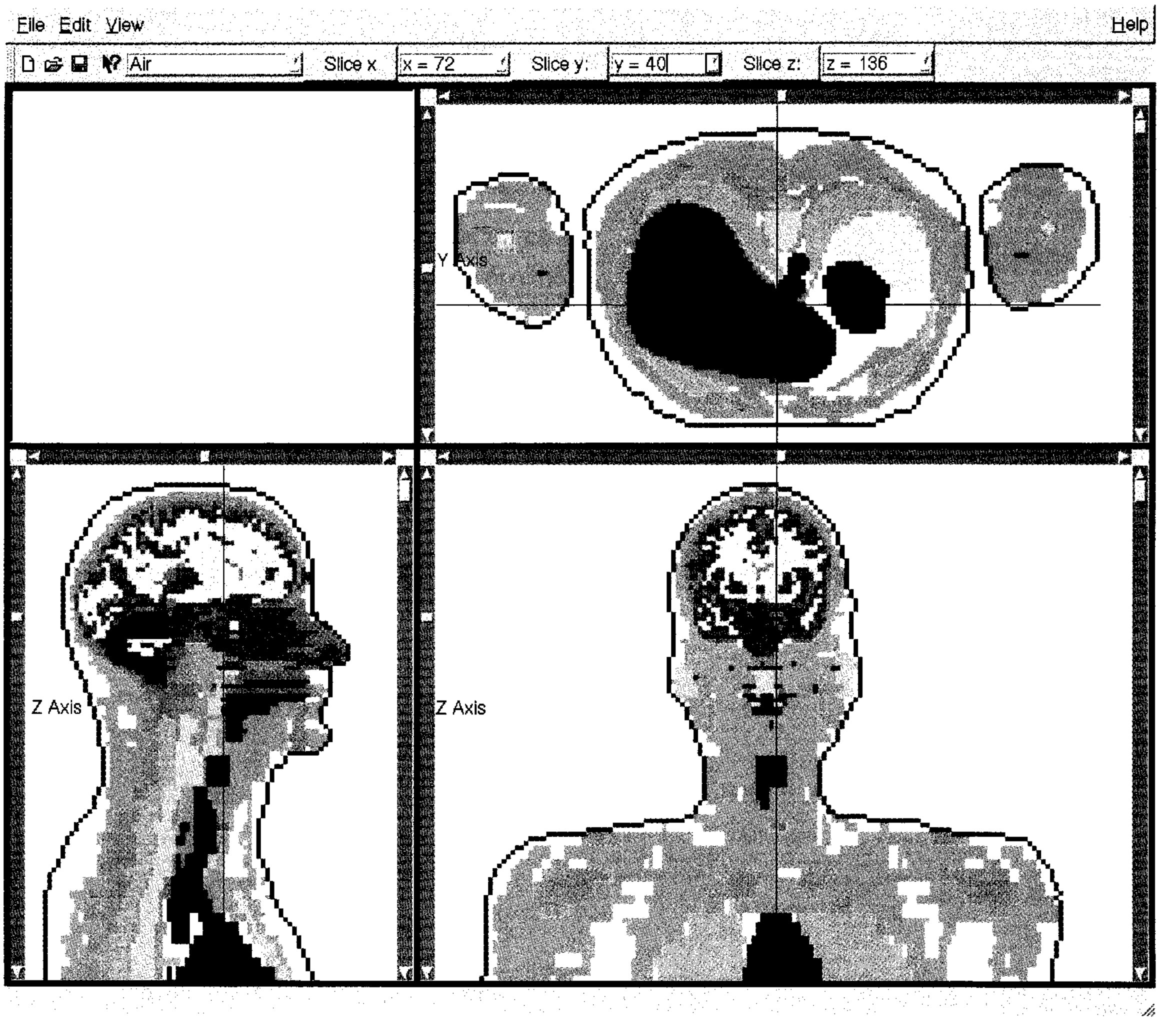

Air

Slice x: x = 72

Slice y: y = 40

Slice z: z = 136

Figure C-2 Model viewing and editing program currently under development.

The editing capabilities in this version of the program will be extended to 3-dimensions and will allow inserting arbitrarily placed boxes, cylinders, and spheres made of a selected tissue.

Apendix D. Comparison of SPFD data from two laboratories

Table D-1 and Table D-2 present comparisons between the data computed in two laboratories for NORMAN and UVic models, as described in Chapter 6. NORMAN has resolution of ~2 mm (see Table 6-1). The UVic model has a slightly different posture (the hands in front) and resolution of 3.6 mm. Considering data in Table D-1 and Table D-2, it can be noted, that for a great majority of tissues, the difference is 1% or less. Only in a few cases the difference reaches 2-3 %. Differences of the order of 1-2 % are typically expected on the basis of the accuracy analysis [51].

Effects of Model Size, Shape and Resolution

Data in Table D-3 illustrate the influence of the body model size, shape including anatomy and resolution on the average, voxel maximum and 99 percentile of the induced electric field. All data shown in Table D-3 have been obtained at the University of Victoria. The UVic model has the hands at the side. The effect of the size is the best illustrated by the AF model, and as expected, the whole body and most of the organ measures are larger than for the two other models, which are of similar height and weight. It is interesting to note, that the AF model mass is 37 % greater than that of the UVic model mass and 42% greater than NORMAN. Correspondingly, the whole-body-average electric fields are 41% and 44% greater, while 99 percentile electric fields are 41% and 34% greater, respectively. This is not unreasonable, since the difference in height of the models is small (0.2%), thus the increase in volume (mass) is mainly in the horizontal frontal dimensions of the torso, as also illustrated in Figure 6-1. Such simple mass-based scaling does not apply even approximately to specific organs and tissues. However, the highly developed muscle tissue in the AF model results in about 50% greater E_{avg} than in other models, but only about 20% greater E_{99}. For the two models of similar height and weight, the whole-body E_{avg} values vary by 3 and 4% for 2 and 4 mm resolution, respectively, and 6 and 1% for E_{99}.

The actual anatomy of persons represented by the models, as well as the accuracy of the models, both influence differences in the two dosimetric measures that are computed accurately, namely E_{avg} and E_{99} [51]. The two models of similar size have typically their average and 99 percentile different by about 10 % or less, e.g., E_{avg} in blood, brain, heart, kidney, muscle, and E_{99} blood, brain, muscle, for the same model resolution. A large difference in bone marrow is a direct result of tissue identification in the models. In this case, bone marrow is not included in the rib cage in NORMAN resulting in smaller values of the considered dosimetric measures. Relatively small organs, such as the testes, or thin organs, such as the spinal cord, also indicate larger differences in induced electric field strengths that can be directly ascribed to the differences in the shape and size of these organs in the models.

Regarding the model resolution, the differences (Table D-3) for E_{avg} and E_{99} are relatively small and consistent with those previously reported [52]. As reported previously, relatively smaller organs (testes in Table D-3) are not well represented by more coarse models. The most apparent and consistent factor is the influence of the model resolution on voxel maximum values. The large values of E_{max} for the high resolution models are inherent in their division into voxels, namely the large current density in the vicinity of the inner corner of a given organ/tissue boundary layer [52]. Furthermore, the reduction of E_{max} for a coarser resolution of a model depends on the adjacent tissues. This explains, for instance, the smaller reduction of brain E_{max} for the

UVic model (where special care has been taken to keep brain tissue surrounded by csf), than for NORMAN, whose original model has been re-sampled without any additional manual editing. As evaluated in [52], the increase in the voxel maximum is greater for a larger contrast in the conductivity of the neighbor tissues.

Very large differences exceeding 100 % can be noted for E_{max} in high-resolution models. The highest maximum value in any model for the whole body is typically associated with voxels of the skin NORMAN and UVic models have been extensively checked to ensure that all tissues, except eyes and air cavities, are covered with skin.

Table D-1 Comparison of the induced electric field (μV/m) in organs and tissues of NORMAN in a uniform magnetic field of 1 μT, 60 Hz, oriented from front-to-back. The model resolution is approximately 2 mm

	Number	Average			Maximum			99 Percentile		
Tissue	of voxels	NRPB	UVic	% diff.	NRPB	UVic	% diff.	NRPB	UVic	% diff.
Skin	525818	16.5	16.5	0	1090	1160	7	71.6	73.0	2
CSF	39444	3.53	3.55	0	35.0	34.2	2	11.9	11.9	0
Spinal cord	9449	7.16	7.26	1	74.2	72.5	2	29.9	29.2	2
Long bones	742714	18.0	17.5	3	265	266	0	113	111	1
Muscle	3363332	12.9	12.8	1	179	176	2	42.6	42.9	1
Lung	465638	22.8	22.8	0	140	140	0	58.8	59.2	1
Heart	40441	16.9	16.7	1	82.6	82.1	1	58.4	58.1	1
Liver	208228	29.2	29.4	1	108	109	1	57.3	57.4	0
Gall bladder	1243	11.7	11.8	1	29.5	29.7	1	25.1	25.3	1
Kidney	37191	20.2	20.3	0	79.0	79.5	1	42.5	42.7	1
Stomach	24752	13.1	13.1	0	92.3	92.0	0	53.2	53.0	0
Small bowel	115947	10.4	10.3	0	49.7	50.6	2	24.0	23.8	1
Pancreas	12147	9.11	9.13	0	33.3	33.2	0	21.8	21.8	0
Fat	1961432	20.5	20.4	0	454	478	5	96.1	97.9	2
Blood	109406	7.09	7.04	1	47.8	46.7	2	23.5	23.1	2
Thyroid	2334	11.2	11.0	1	17.8	17.8	0	16.3	16.3	0
Spleen	19622	33.2	33.2	0	89.1	89.4	0	58.7	58.7	0
Bladder	5849	11.4	11.7	2	92.7	94.1	2	52.8	53.2	1
Breast	3103	13.6	13.7	1	27.0	27.5	2	24.4	24.8	2
Duodenum	11434	8.67	8.73	1	31.9	32.2	1	22.7	22.9	1
Brain	165443	10.0	10.0	0	84.8	84.8	0	30.7	30.7	0
Lower large intest	34694	9.86	9.84	0	54.6	54.1	1	26.6	26.3	1
Upper large intest	51666	13.1	13.1	0	56.6	56.4	0	29.1	29.2	0
adrenals	1786	15.4	15.4	0	26.5	26.8	1	24.1	24.5	1
Eye sclera	767	2.86	2.86	0	8.61	8.63	0	6.71	6.72	0
Eye humor	1377	1.78	1.78	0	4.02	4.03	0	3.46	3.45	0
Eye lens	41	1.53	1.54	0	2.51	2.51	0	2.51	2.51	0

Table D-2 Comparison of the induced electric field (μV/m) in organs and tissues of the UVic model with hands in front The magnetic field is 1 μT, 60 Hz, oriented from front-to-back. The model resolution is 3.6 mm.

Tissue	Number of voxels	Average			Maximum			99 Percentile		
		NRPB	UVic	% diff.	NRPB	UVic	% diff.	NRPB	UVic	% diff.
Skin	126253	17.5	17.5	0	305	304	0	70.4	70.5	0
CSF	6545	4.34	4.33	0	18.6	18.7	0	13.2	13.2	0
Spinal cord	3752	6.46	6.42	1	41.3	41.1	0	28.2	28.0	1
Bone	139668	17.3	17.3	0	118	117	0	63.1	63.1	0
Muscle	743114	12.5	12.5	0	123	122	1	42.5	42.6	0
Lung	62364	17.4	17	0	71.8	71.4	1	41.0	41.0	0
Heart	9354	11.7	11.5	2	41.1	41.0	1	32.2	31.7	1
Liver	29277	27.6	27.9	1	99.9	101	1	60.8	61.3	1
Gall bladder	329	4.45	4.52	2	15.2	15.4	1	10.1	10.2	1
Kidney	7618	20.9	20.9	0	58.0	58.8	2	44.8	44.7	0
Stomach	5133	8.97	8.83	2	32.4	32.1	1	24.8	24.6	1
Small bowel	26447	11.8	11.7	1	44.3	44.0	1	26.8	26.6	1
Colon	18284	19.1	19.1	0	66.6	66.2	1	44.4	44.4	0
Pancreas	792	6.94	6.80	2	24.6	24.2	2	22.1	21.7	2
Fat	330022	23.1	23.2	0	259	259	0	87.5	87.8	0
Blood	21000	5.72	5.73	0	69.4	69.0	1	19.6	19.6	0
Bone marrow	29941	13.6	13.5	0	129	128	1	77.6	77.4	0
Spleen	5568	34.8	34.6	1	76.8	76.3	1	59.9	59.4	1
Testes	1479	12.1	12.1	0	60.4	60.4	0	33.8	33.8	0
Prostate	438	13.8	13.9	0	43.2	43.6	1	30.1	30.2	0
Bladder	3147	7.78	7.79	0	33.0	33.0	0	24.4	24.5	1
Cartilage	900	9.76	9.73	0	31.8	31.6	1	29.1	29.0	1
Diaphragm	4528	11.6	11.6	0	57.1	56.7	1	34.5	34.3	1
Brain	30714	8.85	8.84	0	45.6	45.5	0	23.2	23.2	0
Tongue	1156	2.24	2.24	0	7.87	7.78	1	6.14	6.14	0
Eye retina	224	4.03	4.03	0	15.7	15.6	0	12.7	12.7	0
Eye cornea	100	3.07	3.07	0	5.44	5.44	0	5.44	5.44	0
Eye humor	315	2.09	2.09	0	4.93	4.92	0	4.67	4.66	0
Eye lens	8	2.21	2.22	0	3.10	3.10	0	3.09	3.10	0

Table D-3 Comparison of the induced electric field (μV/m) in a few organs and tissues for various models and their resolution The magnetic field is 1 μT, at 60 Hz, directed from front-to-back.

Tissue	E_{avg}					E_{max}					E_{99}				
	NRPB ~2 mm	NRPB 4 mm	UVic 1.8 mm	UVic 3.6 mm	AF 2 mm	NRPB ~2 mm	NRPB 4 mm	UVic 1.8 mm	UVic 3.6 mm	AF 2 mm	NRPB ~2 mm	NRPB 4 mm	UVic 1.8 mm	UVic 3.6 mm	AF 2 mm
Blood	7.04	6.75	6.15	6.31	8.85	46.7	32.8	87.1	78.2	90.0	23.1	22.2	20.5	20.8	35.6
Bone marrow	9.39	8.95	12.9	13.3	16.1	126	98.3	168	132	292	50.7	46.8	78.0	77.4	65.8
Brain	10.0	9.49	9.07	8.82	10.3	84.8	51.4	65.5	64.7	93.0	30.7	28.0	26.5	25.6	21.4
CSF	3.55	3.71	4.01	4.28	9.15	34.2	19.5	26.5	20.8	44.9	11.9	12.4	13.9	12.2	11.9
Heart	16.7	13.7	14.5	14.4	16.7	82.1	59.0	56.4	50.3	123	58.1	45.8	41.1	41.2	34.3
Kidneys	20.3	19.3	20.7	20.6	20.4	79.5	61.0	92.5	69.5	55.3	42.7	37.7	50.2	49.0	31.7
Lungs	22.8	21.3	18.9	18.9	20.7	140	76.8	102	85.5	80.3	59.2	54.5	46.4	46.2	35.8
Muscle	12.8	12.8	12.4	12.6	18.7	176	104	135	124	300	42.9	42.1	42.5	42.9	49.5
Spinal cord	7.26	6.71	9.54	9.72		72.5	58.1	69.6	60.6		29.2	24.8	37.3	41.0	
Testes	9.88	11.1	12.4	13.0	14.2	49.1	38.6	80.5	69.4	32.6	26.2	28.3	32.9	32.9	32.6
Whole body	15.8	15.5	16.2	16.1	22.8	1160	586	348	297	1350	75.6	67.4	71.4	66.8	101

Apendix E. RF exposure safety standards

Tables E-1-6 summarize the RF exposure limits from FCC regulations in the US [71], and CENELEC guidelines in Europe [72].

Table E-1FCC Limits for Maximum Permissible Exposure (MPE) for Occupational/Controlled Exposure.

Frequency Range (MHz)	Electric Field Strength (V/m)	Magnetic Field Strength (A/m)	Power Density (mW/cm^2)	Averaging Time (minutes)
0.3 – 3.0	614	1.63	(100)*	6
3.0 – 30	1842/f	4.80/f	(900/f^2)*	6
30 - 300	61.4	0.163	1.0	6
300 – 1500	--	--	f/300	6
1500 – 100,000	--	--	5	6

f = frequency in MHz *Plane-wave equivalent power density

Table E-2 FCC Limits for Maximum Permissible Exposure (MPE) for General Population/Uncontrolled Exposure.

Frequency Range (MHz)	Electric Field Strength (V/m)	Magnetic Field Strength (A/m)	Power Density (mW/cm^2)	Averaging Time (minutes)
0.3 – 1.34	614	1.63	(100)*	30
1.34 – 30	824/f	2.19/f	(180/f^2)*	30
30 – 300	27.5	0.073	0.2	30
300 – 1500	--	--	f/1500	30
1500 – 100,000	--	--	1.0	30

f = frequency in MHz *Plane-wave equivalent power density

Table E-3 FCC Limits for Specific Absorption Role (SAR).

Population	Whole-Body	Partial-Body	Hands, Wrists, Feet and Ankles
General	0.08 W/kg	1.6 W/kg	4.0 W/kg
Workers	0.4 W/kg	8.0 W/kg	20.0 W/kg

NOTE 1: *Whole-Body SAR* is averaged over the entire body, *Partial-Body SAR* is averaged over any 1g of tissue defined as a tissue volume in the shape of a cube. *SAR for Hands, Wrists, Feet and Ankles* is averaged over any 10g of tissue defined as a tissue volume in the shape of a cube.

NOTE 2: At frequencies above 6 GHz, *SAR* limits are not applicable and MPE limits for field strength and power density should be applied.

Table E-4 CENELEC Limits of specific absorption rate (continuous exposure) and specific absorption.

Population	SAR averaged over any 6-min. time interval and over the whole body	SAR averaged over any 6-min. time interval and any 10g a) of tissue other than hands, wrists, feet, ankles	SAR averaged over any 6-min. time interval and any 10g a) of tissue in the hands, wrists, feet, ankles
General	0.16 W/kg	2 W/kg	4 W/kg
Workers	0.4 W/kg	10 W/kg	20 W/kg

a). The 10-g mass should be chosen as a cube, not as a flat sheet at the surface.

Table E-5 CENELEC reference levels for field-strength and power density, continuous exposure for workers.

Frequency (MHz)	RMS – value of electric field-strength (V/m)	RMS – value of mag- netic field-strength (A/m)	Mean power density (W/m^2)
0.01 – 0.038	1000(a)	42(a)	
0.038 – 0.61	1000(a)	1.6/f (a)	
0.61 – 10	614/f	1.6/f	
10 – 400	61.4	0.16	10
400 – 2000	$3.07 \cdot f^{1/2}$	$8.14 \cdot 10^{-3} \cdot f^{1/2}$	f/40
2000 – 150,000	137	0.364	50
150,000 – 300,000	$0.354 \cdot f^{1/2}$	$9.4 \cdot 10^{-4} \cdot f^{1/2}$	$3.334 \cdot 10^{-4} \cdot f$

f = frequency in MHz

Table E-6 CENELEC reference levels for field-strength and power density, continuous exposure for general population.

Frequency (MHz)	RMS – value of electric field-strength (V/m)	RMS – value of mag- netic field-strength (A/m)	Mean power density (W/m^2)
0.01 – 0.042	400(a)	16.8(a)	
0.042 – 0.68	400(a)	0.7/f (a)	
0.68 – 10	275/f	0.7/f	
10 – 400	27.5	0.07	2
400 – 2000	$1.37 \cdot f^{1/2}$	$3.64 \cdot 10^{-3} \cdot f^{1/2}$	f/200
2000 – 150,000	61.4	0.163	10
150,000 – 300,000	$0.158 \cdot f^{1/2}$	$4.21 \cdot 10^{-4} \cdot f^{1/2}$	$6.67 \cdot 10^{-5} \cdot f$

f = frequency in MHz